Università degli studi di Pisa
Facoltà di Scienze Matematiche, Fisiche e Naturali
Scuola di Dottorato 'G.Galilei'

Dottorato di Ricerca in Fisica Applicata
Ciclo XX

Tesi di Dottorato
PhD Thesis

Modeling and Simulation of Seismic Attenuation Systems for Gravitational Wave Interferometers

Dr. Valerio Boschi

Internal supervisor: Prof. Diego Passuello
External supervisor: Prof. Virginio Sannibale

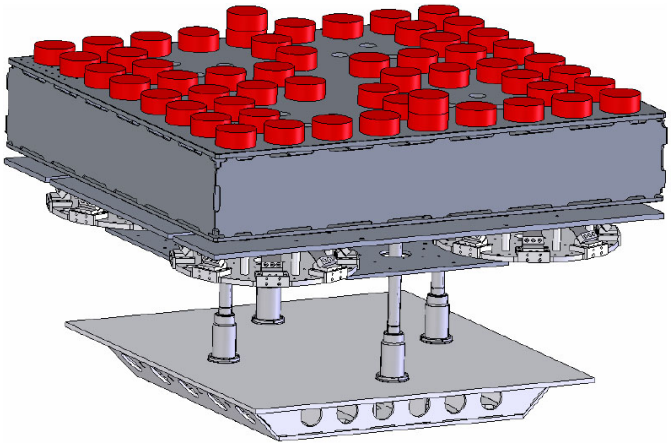

SSD FIS/01

Contents

Abstract

In order to detect gravitational waves (GW), the displacement of the test masses has to be reduced to the challenging level of 10^{-18} m/$\sqrt{\text{Hz}}$. For second generation detectors like Advanced LIGO the requirements are even more compelling. Since the seismic noise is the dominant low frequency noise source for terrestrial GW detectors, the performance and reliability of seismic attenuation systems play a critical role.

This thesis analyzes the mechanical modeling and simulation of seismic attenuators for GW interferometers. The first part of our study concentrated on HAM-SAS, a single-stage passive mechanical isolator, proposed by the California Institute of Technology SAS group, that is designed to support the Advanced LIGO HAM vacuum chambers. Several analytical and numerical simulation techniques have been used in order to determine the performance, reliability and controllability of the system and to obtain a set of linear models that can be used for the active control of the attenuator. The second part of this work is dedicated to the pre-isolator stage of Virgo suspensions. We obtained a set of state-space representations of Virgo inverted pendulum using system identification techniques and we developed a Kalman filter, based on the linear models, that is able to estimate independently every resonance mode of the pre-isolator from open loop data.

Here we summarize the contents of each chapter. In chapter 1 we give an overview of gravitational wave sources. In chapter 2 we discuss the noise sources affecting GW interferometers. Chapter 3 describes LIGO and Virgo detectors, giving special attentions to the different strategies used for seismic attenuation. In chapter 4 we provide a description of HAM-SAS and we discuss the test and measurements results of its prototype. In chapter 5 we developed a series of analytical models in order to evaluate HAM-SAS performance and compare it to the AdLIGO seismic noise requirements. In chapter 6 we study a set of non-linear numerical models of HAM-SAS developed with MBDyn simulation software. In chapter 7 we apply a recently developed linearization technique in order to extract state-space representations from the numerical models. Finally in chapter 8 we describe the linear models and the Kalman filter developed for Virgo inverted pendulum.

Part I

Introduction

Chapter 1

Gravitational Waves

1.1 Gravitational Waves

1.1.1 Theoretical origin

In special relativity, the space-time interval between two events [1] is:

$$ds^2 = c^2dt^2 - dx^2 - dy^2 - dz^2 \tag{1.1}$$

This expression can also be written using tensorial notation as

$$ds^2 = \eta_{\mu\nu}dx^\mu dx^\nu \tag{1.2}$$

where $\eta_{\mu\nu} = \begin{pmatrix} 1 & 0 & 0 & 0 \\ 0 & -1 & 0 & 0 \\ 0 & 0 & -1 & 0 \\ 0 & 0 & 0 & -1 \end{pmatrix}$ is the Minkowski metric. In general relativity space is not necessarily flat, so the definition of interval becomes:

$$ds^2 = g_{\mu\nu}dx^\mu dx^\nu \tag{1.3}$$

where $g_{\mu\nu}$ is no longer a constant tensor. If the curvature is small, we can write a linear approximation of the metric as:

$$g_{\mu\nu} = \eta_{\mu\nu} + h_{\mu\nu} \tag{1.4}$$

where all $h_{\mu\nu}$ tensor elements are much smaller than 1.

The quantity that describes the space-time curvature in every reference frame is a 4^{th} order tensor, called Riemann tensor, given by

$$R^\mu_{\nu\rho\sigma} = \partial_\rho\Gamma^\mu_{\nu\sigma} - \partial_\sigma\Gamma^\mu_{\nu\rho} + \Gamma^\mu_{\alpha\rho}\Gamma^\alpha_{\nu\sigma} - \Gamma^\mu_{\alpha\sigma}\Gamma^\alpha_{\nu\rho} \tag{1.5}$$

where $\Gamma^\mu_{\nu\rho}$ are the Christoffel symbols, functions of the metric tensor:

$$\Gamma^\mu_{\nu\rho} = \frac{1}{2}g^{\mu\sigma}(\partial_\rho g_{\sigma\nu} + \partial_\nu g_{\sigma\rho} - \partial_\sigma g_{\nu\rho}) \tag{1.6}$$

The Riemann tensor contraction is a 2^{nd} order tensor, called Ricci tensor, given by

$$R_{\mu\nu} = g^{\rho\sigma}R_{\rho\mu\sigma\nu} = \partial_\rho\Gamma^\rho_{\mu\nu} - \partial_\nu\Gamma^\rho_{\mu\rho} + \Gamma^\rho_{\mu\nu}\Gamma^\sigma_{\rho\sigma} - \Gamma^\sigma_{\mu\rho}\Gamma^\rho_{\nu\sigma} \tag{1.7}$$

The equation that describes the gravitational field in general relativity, called Einstein field equation, is

$$R_{\mu\nu} = \frac{8\pi G}{c^4}(T_{\mu\nu} - \frac{1}{2}g_{\mu\nu}T^{\lambda}_{\lambda}) \tag{1.8}$$

where $T_{\mu\nu}$ is the stress-energy tensor, the quantity that describes the density and flux of energy and momentum in spacetime. Using (1.4), we can expand at first order both the Ricci tensor and the Christoffel symbols obtaining

$$R_{\mu\nu} \simeq \partial_\nu \Gamma^{\lambda}_{\lambda\mu} - \partial_\lambda \Gamma^{\lambda}_{\mu\nu} + o(h^2) \tag{1.9}$$

and

$$\Gamma^{\lambda}_{\mu\nu} \simeq \frac{1}{2}\eta^{\lambda\rho}(\partial_\mu h_{\rho\nu} + \partial_\nu h_{\rho\mu} - \partial_\rho h_{\mu\nu}) + o(h^2) \tag{1.10}$$

In order to simplify the calculations even further, we have to introduce a particular condition on the coordinate system, called harmonic gauge, given by

$$g^{\mu\nu}\Gamma^{\lambda}_{\mu\nu} = 0 \tag{1.11}$$

Using (1.10), this expression can be approximated at the first order as

$$\partial_\mu h^{\mu}_{\nu} = \frac{1}{2}\partial_\nu h^{\mu}_{\mu} \tag{1.12}$$

Therefore, using (1.9) and (1.12), the Einstein equation, linearized in h, becomes:

$$\Box h = \frac{16\pi G}{c^4}(T_{\mu\nu} - \frac{1}{2}g_{\mu\nu}T^{\lambda}_{\lambda}) \tag{1.13}$$

where we have introduced the $\Box = \frac{1}{c^2}\frac{\partial^2}{\partial t^2} - \nabla^2$ operator. The solution set is given by the sum of a particular solution of (1.13) and the solutions of the associated homogeneous equation. These last solutions are just a superposition of plane waves propagating with speed c, given by

$$h_{\mu\nu}(x) = e_{\mu\nu}\exp(ik_\lambda x^\lambda) + e^*_{\mu\nu}\exp(-ik_\lambda x^\lambda) \tag{1.14}$$

where k_λ is the 4-wave vector and $e_{\mu\nu}$ is a symmetric matrix, called polarization tensor. Using (1.12) condition, it's possible to eliminate 4 of 10 independent components of $e_{\mu\nu}$. Introducing another condition on the coordinate system, called transverse-traceless gauge (TT-gauge), the polarization tensor becomes

$$e_{\mu\nu} = \begin{pmatrix} 0 & 0 & 0 & 0 \\ 0 & a & b & 0 \\ 0 & b & -a & 0 \\ 0 & 0 & 0 & 0 \end{pmatrix} \tag{1.15}$$

Therefore $e_{\mu\nu}$ can be written as a sum of two tensors

$$e_{\mu\nu} = a(e_+)_{\mu\nu} + b(e_\times)_{\mu\nu} \tag{1.16}$$

where $(e_+)_{\mu\nu} = \begin{pmatrix} 0 & 0 & 0 & 0 \\ 0 & 1 & 0 & 0 \\ 0 & 0 & -1 & 0 \\ 0 & 0 & 0 & 0 \end{pmatrix}$ and $(e_\times)_{\mu\nu} = \begin{pmatrix} 0 & 0 & 0 & 0 \\ 0 & 0 & 1 & 0 \\ 0 & 1 & 0 & 0 \\ 0 & 0 & 0 & 0 \end{pmatrix}$.

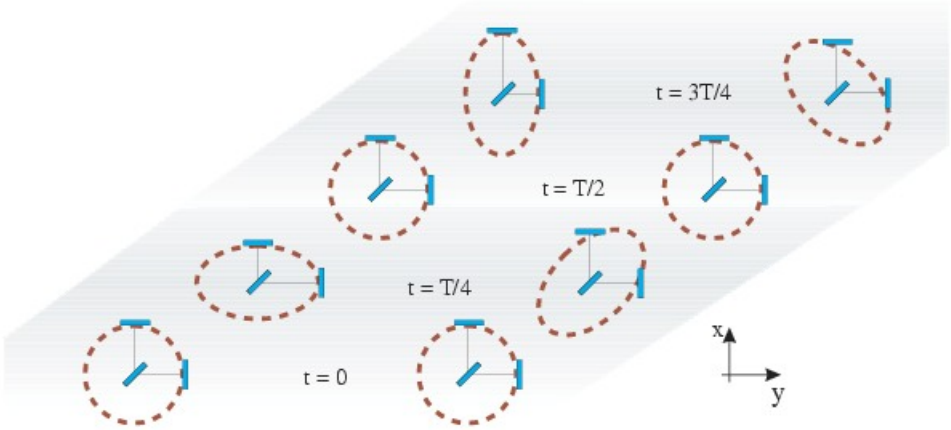

Figure 1.1: Effects of the two different polarization directions of a gravitational wave on a set of freely falling masses arranged on a circumference.

The matrices $(e_+)_{\mu\nu}$ and $(e_\times)_{\mu\nu}$ are the only physical degrees of freedom of gravitational waves and represents the two orthogonal polarization directions of a gravitational wave propagating along the $\hat{z}$ axis. In fig. 1.1 is shown the interaction of the components with a set of freely falling masses arranged on a circumference. The $(e_+)_{\mu\nu}$ component lengthens the distances along $\hat{x}$ and simultaneously shrinks them along $\hat{y}$. The effect of $(e_\times)_{\mu\nu}$ is the same but the principal axes are rotated by 45 degrees.

1.1.2 Quadrupole radiation

The formal analogy between Newton's law of gravitation and Coulomb's law suggests the possibility to expand gravitational radiation, as we do in electrodynamics, using multipole moments. We can, for example, define a gravitational dipole moment as [2]:

$$d_g = \int dV \rho\left(r\right) r \tag{1.17}$$

where $\rho\left(r\right)$ is the mass density of the source and r is the distance from the origin. However the equivalence between inertial mass and gravitational mass requires the respect of classical mechanics conservation laws. Since $\dot{d}_g$ represents the momentum, quantity that remains constant in a isolated system, no radiation can be associated to this distribution moment.

The first term able to generate gravitational waves is the quadrupole moment. In the typical case, where motions within the source can be considered slow compared with the speed of light, it can be written as:

$$I_{\mu\nu} \equiv \int dV \left(x_\mu x_\nu - \frac{1}{3}\delta_{\mu\nu} r^2\right) \rho\left(r\right) \tag{1.18}$$

The field associated to this component results

$$h_{\mu\nu} = \frac{2G}{Rc^4} \ddot{I}_{\mu\nu} \tag{1.19}$$

In order to have a preliminary estimate of h, we are going to use these relations in the case of a binary star, one of the most common gravitational wave sources. We consider the motion circular with radius r_0 and frequency f_{orb}. We also assume the same mass M for both objects. Applying (1.18) e (1.19) we get

$$h_{xx} = -h_{yy} = \frac{32\pi^2 G}{Rc^4} M r_0^2 f_{orb}^2 \cos\left[2\left(2\pi f_{orb}\right) t\right] \tag{1.20}$$

$$h_{xy} = h_{yx} = \frac{-32\pi^2 G}{Rc^4} M r_0^2 f_{orb}^2 \sin\left[2\left(2\pi f_{orb}\right) t\right] \tag{1.21}$$

Since the amplitude of a gravitational wave is an adimensional quantity and $f_{orb}^2 = \dfrac{GM}{16\pi^2 r_0^3}$, it's possible to reorder (1.20) and (1.21), obtaining an approximate expression:

$$|h| \sim \frac{r_{s_1} r_{s_2}}{r_0 R} \tag{1.22}$$

where $r_{s_1} = r_{s_2} = \dfrac{2GM}{c^2}$ are the Schwarzschild radii of the two stars. Using typical experimental values for a binary system constituted by neutron stars ($M \sim 1.4 M_\odot$, $f_{orb} \sim 400$ Hz, r_0=20 Km), located in the galaxy cluster closest to the Earth (Virgo, $R \sim 15$ Mpc), we obtain

$$|h| \sim 1 \cdot 10^{-21} \tag{1.23}$$

The lost energy due to gravitational wave emission has been measured for the first time in the case of the binary pulsar PSR1913+16. The orbital period of this system (fig. 1.2), discovered in 1974 by R.Hulse and J.Taylor [3], have been constantly decreasing over the years, falling by almost 40 seconds between 1974 and 2003. This effect, measured also in other systems [4, 5], can be explained only with gravitational radiation emission and represents the only indirect evidence of its existence. The general relativity predictions of the orbital decay are very accurate and have been recently estimated to be consistent at $(0.13 \pm 0.21)\%$ level [6].

1.2 Astrophysical Sources

Depending on their emitted wave forms, the sources of gravitational waves can be classified in three categories:

- Periodic sources: coalescing binaries, spinning neutron stars (pulsars)
- Impulsive sources: supernovae, gamma ray bursts
- Stochastic sources: cosmological background, white dwarf binaries

1.2.1 Coalescing binaries

Coalescing binaries are binary systems constituted by very compact objects, as neutron stars or black holes, that lose energy emitting gravitational radiation. Their orbital period constantly decreases and, after a time τ_c, called coalescing

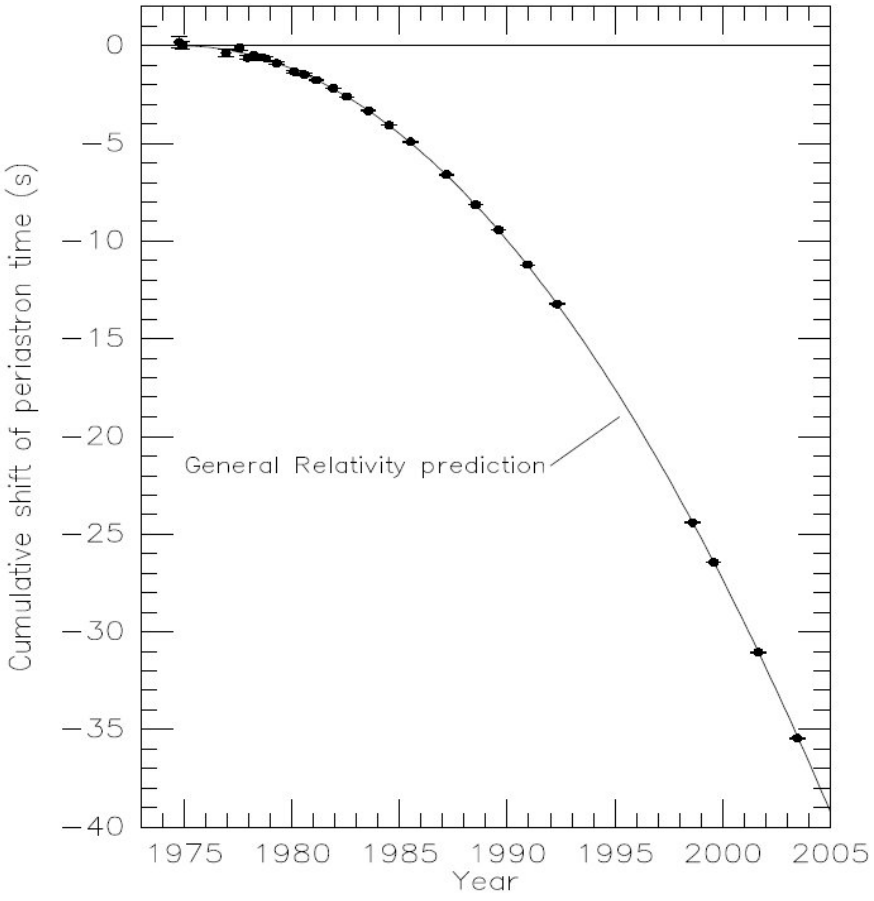

Figure 1.2: Orbital decay of PSR B1913+16 [6]. The data points indicate the observed change in the epoch of periastron with date while the curve shows the theoretically expected change in epoch for a system emitting gravitational radiation, according to general relativity.

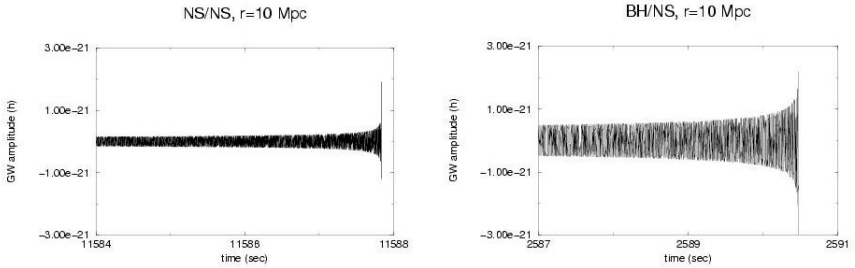

Figure 1.3: Theoretical waveforms of h_+gravitational radiation component emitted by the two main types of coalescing binaries (NS/NS and BH/NS), located at $r = 10$ Mpc distance, in the final phase of their evolution.

time, they eventually merge. Among all gravitational wave sources, the coalescing binaries are the ones the scientific community looks at with more confidence. The known systems of this type, like the above mentioned PSR1913+16 or the PSR1534+12 [4], seem to confirm theoretical predictions very well, and the intensity of their gravitational radiation is expected to be within the sensitivity of terrestrial interferometers.

A first order calculation of the characteristic parameters of these systems can be done using the *newtonian/quadrupolar* approximation. In this regime, the stars are considered as pointlike masses, the tidal deformations are neglected, and the gravitational radiation is generated only by the quadrupole moment. In this way, we can write the law that describes the variations of the orbital frequency f_{orb} with time:

$$f_{orb} = \left(f(0)^{-8/3} - \pi^{8/3} \frac{256}{5} \frac{G^{5/3}}{c^5} M^{5/3} t \right)^{-3/8} \tag{1.24}$$

where $M = \dfrac{(m_1 m_2)^{3/5}}{(m_1 + m_2)^{1/5}}$ with m_1 and m_2 are the star masses. It's possible to write the coalescing time τ_c as

$$\tau_c = 3.0 \, \frac{f_{orb}(0)}{100\text{Hz}} \left(\frac{M}{M_\odot} \right)^{-5/3} \tag{1.25}$$

where $M_\odot$ is the mass of the Sun. We eventually obtain the amplitude of the two polarization components of h:

$$h_+(r,\theta,t) = 6.0{\cdot}10^{-21}(1{+}\cos^2\theta) \left(\frac{M}{M_\odot} \right)^{5/3} \left(\frac{f_{orb}(t)}{1\text{kHz}} \right)^{2/3} \left(\frac{1\text{Mpc}}{R} \right) \cos(2\pi f_{orb} t)$$

$$h_\times(r,\theta,t) = \pm 1.2 \cdot 10^{-20} \cos\theta \left(\frac{M}{M_\odot} \right)^{5/3} \left(\frac{f_{orb}(t)}{1\text{kHz}} \right)^{2/3} \left(\frac{1\text{Mpc}}{R} \right) \sin(2\pi f_{orb} t)$$

where R is the distance of the system. Figure 1.3 shows the theoretical waveforms of the h_+component for coalescing binaries, constituted by two neutron stars (NS/NS) with $m_1 = m_2 = 1.4\ M_\odot$, and by a black hole and a neutron star (BH/NS) with $m_1 = 1.4\ M_\odot$ and $m_2 = 10\ M_\odot$, in the final phase of their

evolution. As shown in the two plots, during the merging, the last phase of the coalescence, the wave has a typical form, called *chirp*, characterized by an oscillation of increasing amplitude and frequency.

Even though the physics of coalescing binaries is well understood, there are many uncertainties on the rate of observable events. The estimates are in a range between $1/10^5$ and $1/10^6$ years for every galaxy. In order to obtain a rate of a few events per year, we have to monitor a distance of about 400 Mpc.

1.2.2 Spinning neutron stars

Spinning neutron stars, or pulsars, are expected to be the main sources of continuous gravitational radiation, which are long-lasting, quasi-monochromatic GWs with slowly varying frequency. Although current models of stellar evolution predict the presence of approximately 10^9 neutron stars in our galaxy, of which 10^5 are expected to be spinning and actively emitting radiation, only about 1700 pulsars have been observed so far. This is due to the high variability in the intensity of the generated radiation. An upper limit of the amplitude of the emitted GWs can be given using statistical arguments [7]. If we assume that the neutron stars are uniformly distributed in the galaxy and have a constant birthrate, the strongest signals will have an amplitude $h \sim 4 \cdot 10^{-24}$.

There are three types of mechanisms usually considered for the emission of continuous GWs from pulsars in the frequency band of current ground-based detectors (20 Hz−2 kHz) [8]:

- Non-axisymmetric distortions of the neutron star: magnetic fields or elastic tension of the pulsar's crust can generate deformations on its surface, called mountains, that are asymmetric respect to the rotation axis. Considering a star with inertia tensor I_{ij}, spinning at frequency ν, the pulsar will generate monochromatic GWs with frequency 2ν and amplitude

$$h = \frac{16\pi^2 G}{c^4} \frac{I_{zz}\nu^2}{d} \epsilon \tag{1.26}$$

  where d is the distance and $\epsilon = \frac{I_{xx} - I_{yy}}{I_{zz}}$ is a parameter, called equatorial ellipticity, that express the star deformation. The range of possible values of ϵ is highly uncertain. Only an upper limit has been estimated: $\epsilon \lesssim 5 \cdot 10^{-5}\sigma$ where σ is the breaking strain of the crust.

- Unstable oscillation modes in the fluid part of the star: spinning neutron stars can be subject to non-axisymmetric instabilities, during their birth and accretion phase, a period in which the star is growing gravitationally attracting matter from an other body. These instabilities can be divided in two broad categories depending on their timescales: dynamic and secular. In the first case the unstable modes grows in a time comparable with the oscillation period, while in the second the growth is much longer. A typical example of a dynamic instability is the so called bar-mode (see fig. 1.4), a process that is expected to affect highly rotating newborn neutron stars. If the ratio between the rotational kinetic energy T and the gravitational binding energy W exceeds a critical value ($T/|W| \gtrsim 0.24$), the star becomes unstable and its geometry is deformed in a bar shape, emitting a burst of GWs. Secular modes are instead thought to be caused

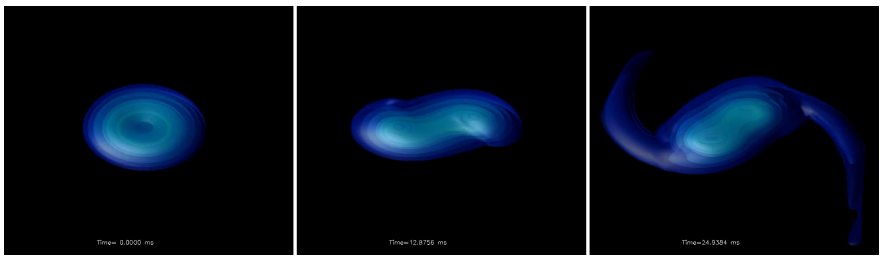

Figure 1.4: Simulation of the bar-mode instability of a spinning neutron star [9]. The three snapshots are taken - from left to right - before the onset of the instability ($t = 0$), during the bar-mode emission ($t \simeq$13 ms), after the formation of spiral arms ($t \simeq$25 ms). The colors give an indication of the star relative local density.

by the Chandrasekhar-Friedman-Schutz instability [10]. In this process, the unstable mode counter-rotate respect to the pulsar in the star frame but co-rotate in an inertial frame. An estimate of the emitted gravitational radiation for a generic unstable neutron star is given by

$$h \simeq 5 \cdot 10^{-22} \left(\frac{E}{10^{-3} M_{\odot} c^2} \right)^{1/2} \left(\frac{f}{1\,\mathrm{kHz}} \right)^{-1/2} \left(\frac{15\,\mathrm{pc}}{d} \right) \tag{1.27}$$

where the two parameters, E, the radiated energy and f, the frequency of the emitted GW, depends on the process that causes the instability.

- Free precession: in this case the neutron star rotation axis is misaligned respect to its symmetry axis forming an angle θ_w. For a star at a distance d and rotating at frequency ν we can write

$$h = 10^{-27} \left(\frac{\theta_w}{0.1\,\mathrm{rad}} \right) \left(\frac{1\,\mathrm{kpc}}{d} \right) \left(\frac{\nu}{500\ \mathrm{Hz}} \right) \tag{1.28}$$

The gravitational radiation is emitted at the three frequencies $f_1 = \nu + \nu_{prec}$, $f_2 = 2\nu$, $f_3 = 2\nu + 2\nu_{prec}$, where ν_{prec} is the precession rate, with decreasing amplitude. While the first and third frequencies emissions are caused by the precession, the second oscillation is caused by the star deviation from axisymmetry in an analogous way as we have seen before.

1.2.3 Supernovae

The explosion of a supernova happens when a massive star, used all their nuclear fuel, cannot sustain its own gravity. Consequently the star central core begin to collapse generating an enormous shockwave that causes the expulsion of the supernova most external layer. While the origin of the electromagnetic emission, generated in these events, is the external shell expulsion, the gravitational radiation is emitted due to the core collapse.

Even though, several years ago, the supernovae were considered as the most easily detectable gravitational wave sources, today we know that the intensity of the radiation emitted during the core collapse could vary considerably depending on the stellar mass percentage that is converted in radiation and by the type

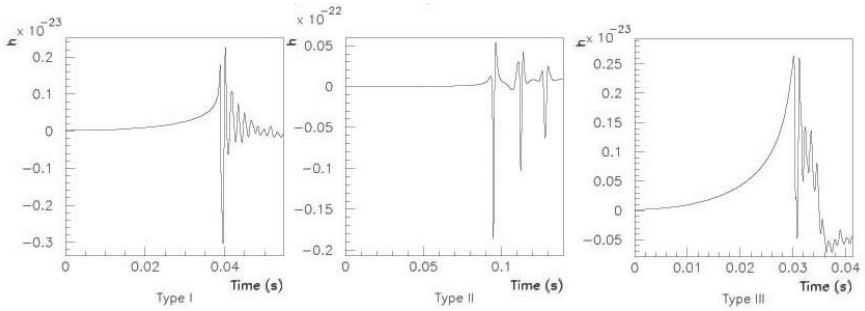

Figure 1.5: Examples of theoretical waveforms emitted by the three main types of supernovae, located at 10 Mpc distance, during their core collapse.

of symmetry of the collapse itself. For example, in case of a perfect spherical collapse, no gravitational radiation is emitted. An estimate of h amplitude is given by the expression:

$$h_+ \sim h_\times \sim C \, \frac{10\text{Mpc}}{R} \tag{1.29}$$

where C is a constant with a value between 10^{-21} and 10^{-24} depending on the physical processes involved in the gravitational wave emission during the collapse. The expected frequency is about some kHz.

The fig. 1.5 shows some theoretical waveforms extracted by a catalog, obtained with a numerical simulation performed in 1997 by T. Zwerger and E. Muller [11], constituted by 78 signals, corresponding to different initial values of the rotation and of the angular moment distribution of the star.

The expected rate for these events is between 1/30 years and 1/40 years per galaxy. The Virgo cluster, that is 20 Mpc distant and constituted by about 2500 galaxies, could therefore generate a rate of several events per year.

1.2.4 Gamma Ray Burst

Gamma-ray bursts (GRBs) are intense flashes of γ-rays which occur approximately once per day and are isotropically distributed over the sky. The variability of the bursts time scales, from a millisecond to several seconds, indicates that the sources are very compact and their measured red shifts have shown that they are generated outside our galaxy. GRBs can be divided in two broad classes depending on their duration: short burst ($\lesssim$ 2 s), that are thought to be caused by mergers of NS/NS or BH/NS binaries, and long events ($\gtrsim$ 2 s), probably associated with the core collapse of supernovae. As we have seen, the emission of gravitational radiation is expected in both scenarios. Although, no experimental evidence of gravitational wave emission associated with GRBs has been found yet, upper limits have been recently given for several events [12].

1.2.5 Stochastic background

A stochastic signal is characterized by a continuous spectrum and an approximately constant amplitude. A possible origin of a gravitational stochastic background is the superposition, in the time or frequency domain, of signals coming

from many sources. We expect for example that the collapse of vast population of black holes could generate, depending on their mass distribution and formation time, signals with intensity and frequency that can be detected by the present experiments.

A particularly interesting stochastic source is constituted by the gravitational equivalent of the well known 3 K cosmic background radiation. It has been hypothesized that some fluctuations of the graviton field - the field associated to the particle that mediates the gravitational interaction in many quantum field theories - present in the primordial universe, have been amplified during the *inflation*, a phase of very rapid expansion of the universe, included in many cosmological models. Depending on the parameters that characterize the inflation process, the intensity of gravitational background radiation could reach detectable levels [13].

Chapter 2

Interferometric GW detection

As R. Dicke wrote in one of the first work on experimental relativity [14]: " In other fields of physics the experimentalist is faced with the problem of choosing the most important out of a large number of possible experiments. With gravitation the problem is different. There are so few possible experiments, and their importance is such, that any and all significant experiments should be performed ".

Historically the first experiments for gravitational wave detection are those performed in the 1960's by J.Weber using two resonant bars [15]. Even though Weber's claims of detection have never been confirmed, various international efforts have contributed over the years to improve the sensitivity of these detectors. In today's resonant bars (the Italian experiments AURIGA, NAUTILUS, EXPLORER, ALTAIR, the experiments ALLEGRO and Niobe in Louisiana, USA and Australia respectively), we measure the normal modes of oscillation of a cylindrical metal mass, cooled at cryogenic temperatures, using extremely sensitive magnetic sensors, called Superconducting Quantum Interference Devices (SQUIDs).

Today, however, the highest expectations of the scientific community are for another kind of instrument: the Michelson interferometer, the same device that has proved the absence of ether, one of the fundamental principles of special relativity.

2.1 Michelson Interferometer

The Michelson interferometer is the core of every GW interferometer. Its optical configuration is shown in fig. 2.1. It consists of a light source e.g. a laser illuminating a 50/50 beam splitter (BS) mirror. Half of the light is transmitted along the laser propagation direction, the other half is reflected into the perpendicular axis. Both beams are reflected by the two mirrors with reflectivities r_1, $r_2 \sim 1$ and then recombined at the beamsplitter.

Let's now consider the effects of a gravitational wave on a Michelson interferometer with its arms aligned along $\hat{x}$ and $\hat{y}$ axes. Let's examine the $\hat{x}$ axis. We know that light connects only events in the space-time that are separated

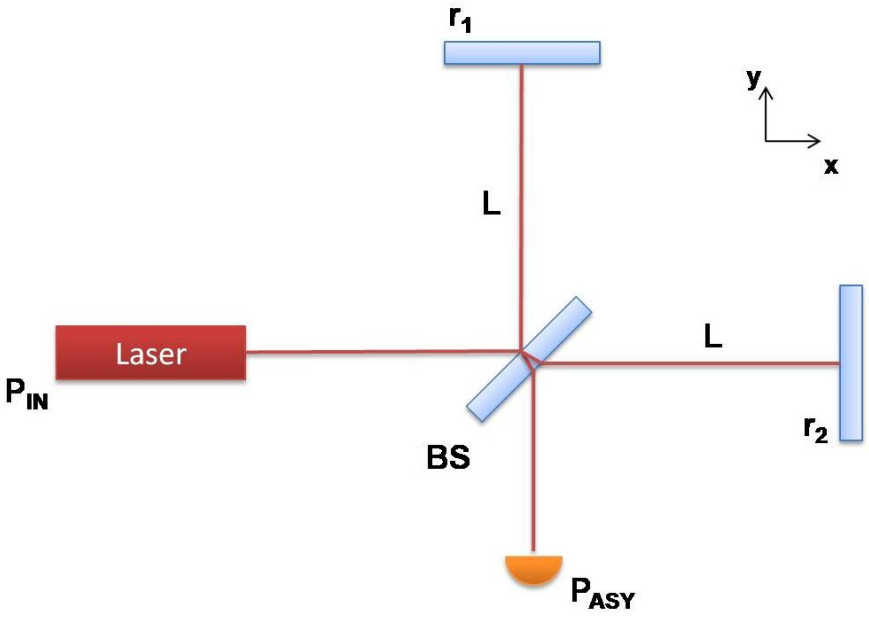

Figure 2.1: Sketch of a Michelson interferometer. The gold semicircle represents the output photodiode.

by a null interval. This means $ds^2 = 0$. Setting (1.2) equal to zero, we obtain

$$ds^2 = -c^2dt^2 + \left(1 + h_{11}\left(2\pi ft - \vec{k}\cdot\vec{x}\right)\right)dx^2 = 0 \tag{2.1}$$

We can evaluate the time the light takes to travel from the beam splitter to the end of the $\hat{x}$ arm, integrating the square root of the previous expression:

$$\tau_x^{(1)} = \frac{1}{c}\int_0^L \sqrt{1+h_{11}}dx \approx \frac{1}{c}\int_0^L \left(1 + \frac{h_{11}}{2}\left(2\pi ft - \vec{k}\cdot\vec{x}\right)\right)dx \tag{2.2}$$

where we expanded the square root at first order, since $h \ll 1$. In the same way, we can write the time needed for the return trip:

$$\tau_x^{(2)} = -\frac{1}{c}\int_L^0 \left(1 + \frac{h_{11}}{2}\left(2\pi ft - \vec{k}\cdot\vec{x}\right)\right)dx \tag{2.3}$$

The total time $\tau_x = \tau_x^{(1)} + \tau_x^{(2)}$ is therefore

$$\tau = \frac{2L}{c} + \frac{1}{2c}\int_0^L h_{11}\left(2\pi ft - \vec{k}\cdot\vec{x}\right)dx - \frac{1}{2c}\int_L^0 h_{11}\left(2\pi ft - \vec{k}\cdot\vec{x}\right)dx \tag{2.4}$$

Let's consider the simplest case of a sinusoidal wave propagating along the $\hat{z}$ axis, with frequency f_{gw}, polarization + and amplitude $h_{11} = -h_{22} = h_0$. The two integrals of (2.4) can be easily calculated, posing $h(t) = h_0 \exp(i2\pi f_{gw}t)$. The total time will be

$$\tau_x = \tau_0 + \frac{h_0}{4\pi f_{gw}} Re[e^{i2\pi f_{gw}\tau_0} - 1] \tag{2.5}$$

where $\tau_0 = \frac{2L}{c}$ is the classic time. For a photon that travels along the $\hat{y}$ arm, the expressions are the same but they depend on h_{22} instead of h_{11}. Therefore

$$\tau_y = \tau_0 - \frac{h_0}{4\pi f_{gw}} Re[e^{i2\pi f_{gw}\tau_0} - 1] \tag{2.6}$$

In the laboratory reference frame this difference in the travel time respect to the classical case can be interpreted as a variation of the interferometer arm lengths, L_x and L_y:

$$L_x = \frac{1}{2}c\tau_x = L\left(1 + \frac{h(t)}{2}\right) \tag{2.7}$$

$$L_y = \frac{1}{2}c\tau_y = L\left(1 - \frac{h(t)}{2}\right) \tag{2.8}$$

For an interferometer 1 Km long, assuming $h \sim 10^{-21}$, this variation is $L_x - L \sim 10^{-18}$ m. The two photons arrive at the output of the interferometer with a phase difference equal to

$$\frac{\delta\phi_{gw}(t)}{h(t)} = \frac{4\pi L}{\lambda} sinc\,(\pi f_{gw}\tau_0) \tag{2.9}$$

where $sinc(x) = \dfrac{\sin x}{x}$. In fig. 2.2 we can see the plots of $\left|\dfrac{\delta\phi_{gw}(t)}{h(t)}\right|$ as a function of the frequency, for different kinds and lengths of interferometers. In the low frequency flat region, where $f_{gw}\tau_0 < 1$, (2.9) can be approximated as

$$\frac{\delta\phi_{gw}(t)}{h(t)} = \frac{4\pi L}{\lambda} \tag{2.10}$$

expression that clearly shows the importance of arm length for increasing the sensitivity of an interferometer.

The power induced by the the passage of gravitational wave on the resulting interference fringe, measured at the antisymmetric port (ASY) by a photodetector, can be written as

$$P_{ASY} = \frac{P_{IN}}{2}(1 + C\cos(\Phi + \delta\phi_{gw})) \tag{2.11}$$

where P_{IN} is the beam power impinging on the beam splitter, Φ is phase difference between the two arms, $C = \frac{2r_1r_2}{r_1^2+r_2^2}$ is the contrast. Since $\delta\phi_{gw}$ can be considered very small, we can rewrite 2.11, keeping only the first order terms, as

$$P_{ASY} = \frac{P_{IN}}{2} C\,[\cos\Phi - \sin(\Phi)\delta\phi_{gw}] \tag{2.12}$$

Thus the power variation δP_{ASY} induced by a gravitational wave is

$$\delta P_{ASY} = \frac{P_{IN}}{2} C\sin(\Phi)\delta\phi_{gw} \tag{2.13}$$

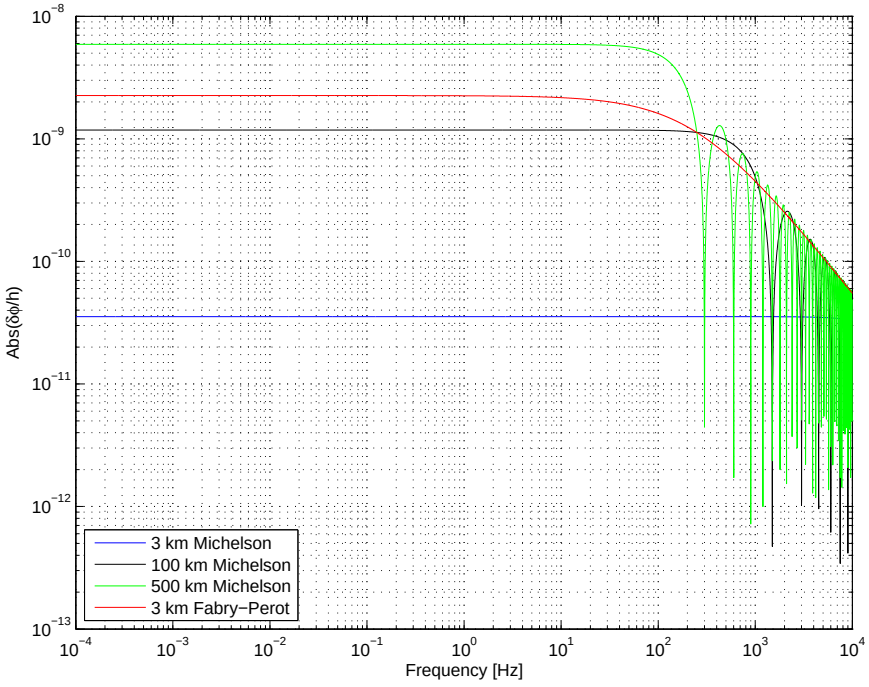

Figure 2.2: Plots of the phase difference $\left|\frac{\delta\phi_{gw}(t)}{h(t)}\right|$ as a function of the gravitational waves frequency f_{gw}, for different arm lengths and types of interferometers. We considered $h(t) \simeq 10^{-21}$. As we can see, the performance of a Fabry-Perot interferometer is roughly equivalent to that of a 100 km Michelson.

2.2 Fabry-Perot Cavities

As we can see from fig. 2.2, without the use of Fabry-Perot cavities no gravitational wave interferometer would be practically feasible. Constituted by two plane mirrors, called the input and end mirrors, separated by a distance L, Fabry-Perot cavities are essentially displacement to phase transducers: the light entering the cavity is reflected with a phase shift that depends by the cavity length. The mirror reflectivities $r_1$and r_2 are chosen to have $1/(1-r_1r_2) \gg 1$. The resonance condition which maximizes the stored energy is $2kL = 2n\pi$ where n is an integer and k is the wavenumber. If the length changes by an amount δL, the phase shift can be written as

$$\delta\phi = \frac{4\mathfrak{F}}{\pi}(2\pi\frac{\delta L}{\lambda}) \tag{2.14}$$

The finesse $\mathfrak{F}$ is defined as the ratio between two consecutive resonances of the cavity and the full width at half maximum of a resonance (FWHM) and is given by

$$\mathfrak{F} = \frac{\pi\sqrt{r_1r_2}}{1-r_1r_2} \tag{2.15}$$

At the resonance, the light is kept inside the cavity for a time τ_s, called storage time, defined as

$$\tau_s = \frac{2L}{c}\frac{\mathfrak{F}}{\pi} \tag{2.16}$$

. Under the assumption of very high reflectivities and very low loss of the mirrors, in the condition $f_{gw}2L/c \ll 1$, the response of a Fabry-Perot interferometer to gravitational waves can be written, in the frequency domain, as

$$\frac{\delta\phi}{h} \sim \tau_s\frac{8\pi c}{\lambda}\sqrt{\frac{1}{(1+4\pi f_{gw}\tau_s)^2}} \tag{2.17}$$

So it behaves essentially as a low-pass filter with cutoff frequency $1/4\pi\tau_s$.

2.3 Noise Sources

Fig. 2.3 gives a detailed overview of the noise sources affecting a GW interferometer. The noises can be essentially divided in two categories

- Displacement noises: the processes that directly move the suspended mirrors. This class of noise sources plays a very important role in interferometer design, since it limits how much we can fold the optical path in order to make the instrument compact. Seismic noise, thermal noise, radiation pressure noise are included in this category.
- Sensing noises: the disturbances that appear in the photodetector signal but they are not caused by a gravitational wave. Examples are the shot noise, the laser instabilities, the readout electronics noise.

Due to the contribution of all noise sources, the output photodiode will measure a phase shift indistinguishable from that generated by an equivalent GW signal

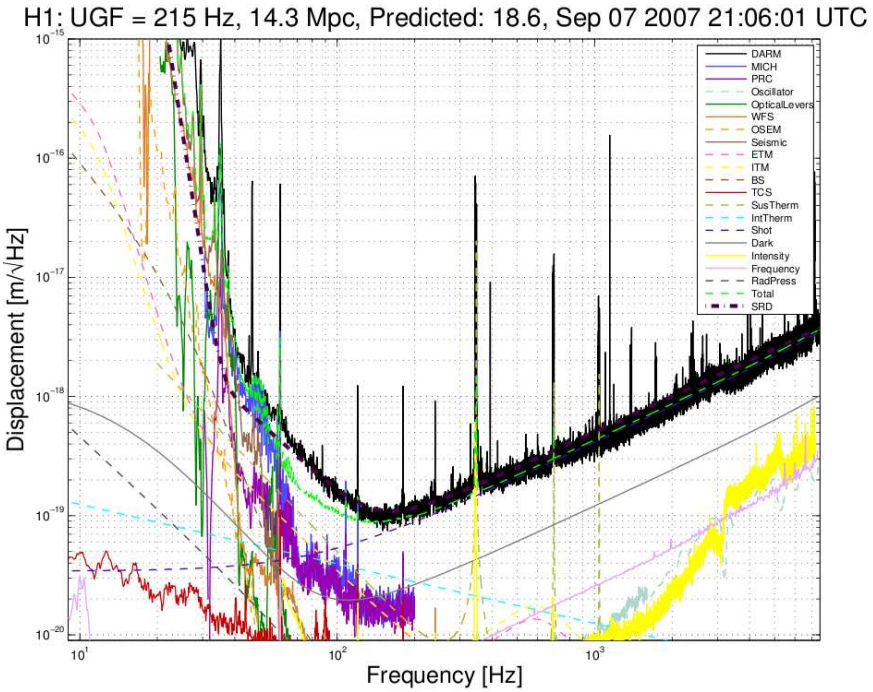

Figure 2.3: LIGO noise budget during one of the last days of S5 science run. Some curves are directly measured (for example the Seismic noise), others are entirely based on the theoretical models (for example the thermal noises SusTherm, IntTherm). The bold dashed purple curve (SRD) represents the required sensitivity.

$h_n(t)$. The two-sided power spectral density S_n is defined as

$$S_n(f) = \lim_{T\to\infty} \frac{1}{T} \left| \int_{-T/2}^{T/2} h_n(t) e^{i2\pi f t} dt \right|^2 \tag{2.18}$$

Since it's easier to think in terms of positive frequencies, in the gravitational wave community it is customary to define the amplitude linear spectral density as

$$\widetilde{h}_n(f) = \sqrt{2 S_n(f)} \tag{2.19}$$

that is expressed in units of $[h_n(t)]/\sqrt{\text{Hz}}$.

2.3.1 Seismic Noise

Seismic noise is the main limitation to the low frequency sensitivity of ground based interferometers. It propagates to the test masses through the suspension system causing perturbations in mirror displacement. The minimum coupling between the horizontal and vertical directions is due to the Earth curvature. As we can see in fig. 2.4, the input and output mirrors of the Fabry-Perot cavities form an angle $\alpha_{grav} = L/r_\oplus \sim 6 \cdot 10^{-4}$ rad (where $L = 4$ km is the cavity length and $r_\oplus$ is the Earth radius) with the global vertical direction. Therefore

a vertical displacement δz has effect along the beam direction, producing a variation $\alpha_{grav}\delta z$ of the optical path. The suspension system causes even larger mechanical couplings (1%), due to structural reasons.

Seismic noise has both natural and human origins and can vary by few orders of magnitude from site to site. However all ground motion displacement spectra observed worldwide share some common characteristics: they have essentially the same amplitude in all three orthogonal space directions and they exhibit a low pass behavior that follows the empirical law [2]

$$\widetilde{x}_{seism}(f) = A\,(1\text{ Hz}/f)^2 \quad \text{m}/\sqrt{\text{Hz}}, \quad \text{if } f > 0.1\text{ Hz} \tag{2.20}$$

with 10^{-9} m/$\sqrt{\text{Hz}} \leq A \leq 10^{-7}$ m/$\sqrt{\text{Hz}}$. If we compare $\widetilde{x}_{seism}(f)$ with the 10^{-18} m/$\sqrt{\text{Hz}}$ displacement induced by a GW on a 1 km Michelson interferometer, we see that we need an isolation system capable to attenuate the seismic noise by 11 orders of magnitude at 1 Hz.

In 1993 J. Peterson [16] collected and analyzed the data from 75 seismic stations around the world and developed two seismic noise models, the New Low Noise Model (NLNM) and the New High Noise Model (NHNM) that are now commonly used as a reference. The models are hypothetical background spectra obtained from a composite of the lowest spectra (NLNM) and from the average of the noisiest sites (NHNM) in the seismometer network. Fig. 2.5 shows a comparison between two polynomial fits of LIGO sites seismic noise spectra (see subsection 5.4) and Peterson's models. There are two main peaks present in Peterson's NLNM and NHNM models. The broad resonance in the 0.1-0.5 Hz range, called microseismic peak, is generated by the interactions of ocean waves at sea and is prominent in all seismic noise spectra measured all over the world. The peak is caused by a non linear process [17] through which ocean waves couple energy into elastic waves, called microseisms. The interaction of water waves with similar frequencies but opposing directions generates a second-order pressure wave with half the period and an amplitude proportional to the product of the wave heights. Unlike the pressure field generated by traveling waves, this pressure wave does not wane with depth and efficiently couples with the Earth's crust to generate seismic surface oscillations that propagates primarily as Rayleigh waves. The resonance between 0.05 Hz and 0.1 Hz is called single-frequency microseismic peak because it's generated by the same process but it doesn't show the frequency doubling of the microseismic peak.

2.3.2 Gravity Gradient Noise

The gravity gradient noise, sometimes called Newtonian noise, poses a fundamental limitation to all seismic attenuation systems. This disturbance is caused by the unavoidable coupling between the test masses and the gravitational field around them. There are two sources of local gravitational fluctuations: the motion of macroscopic objects around the test masses and the seismic motion of ground. While the first cause can be eliminated with careful instrument design, the second is impossible to suppress. Consequently, even using a seismic attenuator with an infinite number of stages, a fraction of the seismic noise will always be transmitted to the mirrors.

An estimate of the transfer function between the gravity gradient noise and the seismic noise power spectra has been obtained by P. Saulson in [18] and can

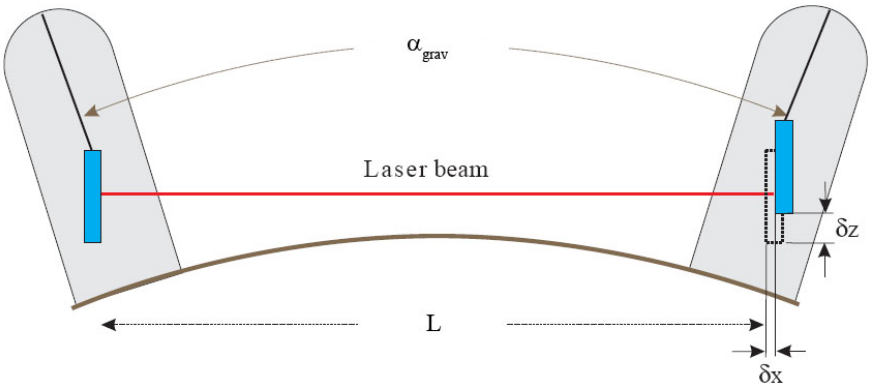

Figure 2.4: Effect of the Earth curvature on mirrors of an interferometer.

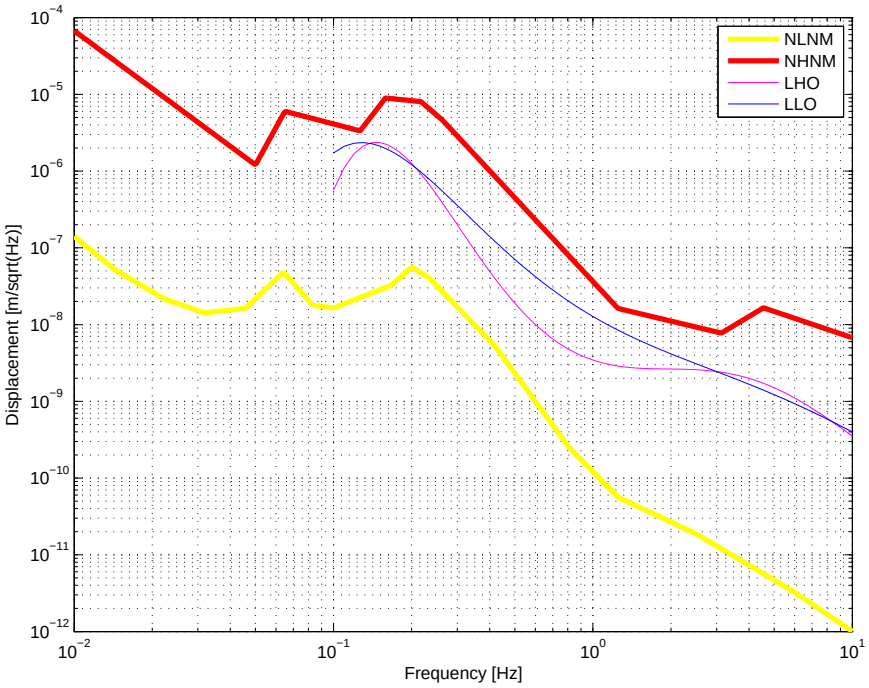

Figure 2.5: Peterson's new low noise (bold yellow) and high noise models (bold red). The spectra are compared with two polynomial fits of the displacement spectral densities of LIGO sites seismic noise. Magenta and blue curves are the noise spectra of Hanford, WA (LHO) and Livingston, LA (LLO) respectively.

be written as

$$\frac{\tilde{h}_{gg}^2}{\tilde{x}_{seism}^2} = \frac{16\pi^3}{3}\frac{G\rho^2}{L^2\omega^4} \tag{2.21}$$

where G is the gravitational constant, L is the interferometer arm length and ρ is the average soil density. Substituting the appropriate values for LIGO and Virgo interferometers we obtain

$$\tilde{h}_{gg} \simeq \frac{1\cdot 10^{-11}}{f^2}\tilde{x}_{seism} \tag{2.22}$$

Using the rough seismic noise estimate 2.20, we obtain $\tilde{h}_{gg} \sim 1{\cdot}10^{-11}A/f^4$ if $f >$ 0.1 Hz . The Saulson's model assumes that the density mass fluctuations of the ground are completely coherent over a characteristic scale $\lambda/2$, and completely uncorrelated for larger separations. Later more refined estimates [19] of the transfer function give results that agree with the order of magnitude of 2.22 but correct its behavior at low frequencies:

$$\tilde{h}_{gg} \simeq \begin{cases} \frac{\beta}{0.6}\frac{6\cdot 10^{-23}}{\sqrt{\text{Hz}}}\left(\frac{10}{f}\right)^2 & if\ 3\text{ Hz} < f < 10\text{ Hz} \\ \frac{\beta}{0.6}\frac{6\cdot 10^{-23}}{\sqrt{\text{Hz}}}\left(\frac{10}{f}\right)^4 & if\ 10\text{ Hz} < f < 30\text{ Hz} \end{cases} \tag{2.23}$$

with $0.15 < \beta < 1.4$ depending on the site seismic activity.

As we will see in the next chapter, the values of $\tilde{h}_{gg}$ are lower than the sensitivity of present interferometers and their upgraded versions. However future GW detectors, the so-called 3rd generation interferometers, are expected to extend their detection band to lower frequencies ($f < 10$ Hz). Since this range is dominated by seismic motion, the gravity gradient noise will represent one of their main limitations. For this reason several solutions to reduce the newtonian noise, like the possibility to build future interferometers in deep underground sites [20] and the development of active noise subtraction techniques [21], are being studied.

2.3.3 Thermal Noise

Thermal noise is another disturbance particularly important for interferometric GW detection in the low frequency range. Unlike seismic noise that could be theoretically completely eliminated, thermal noise can only be reduced, since it has a fundamental nature. The interferometer mirrors are in radiative thermal equilibrium with the vacuum chambers that are at room temperature. The energy exchange generates the Brownian motion of the particles of mirror glass, coating and suspension system and consequently induces a fluctuation in the measured cavity length.

Thanks to the fluctuation-dissipation theorem [22], we don't need to develop a detailed microscopic model of the dissipation phenomena. If a mechanical system can be considered linear and in thermal equilibrium, we can write the power spectrum of the fluctuating force F_{therm} induced by the dissipation simply as

$$\tilde{F}_{therm}^2 = 4k_BT\Re\left(Z(f)\right) \tag{2.24}$$

where k_B is the Boltzmann's constant, T is the temperature and $\Re(Z(f))$ is the real part of the mechanical impedance $Z(f)$ defined as the ratio

$$Z(f) = \frac{\tilde{F}_{ext}(f)}{\tilde{v}(f)} \tag{2.25}$$

between the Fourier transforms of the amplitude of an external force $F_{ext}(t)$ and the velocity $v(t)$ induced on the system. Relation 2.24 can also be written in the equivalent form

$$\widetilde{x}^2_{therm} = \frac{k_B T}{\pi^2 f^2} \Re(Y(f)) \tag{2.26}$$

where $\widetilde{x}_{therm}$ is the power spectrum of the system fluctuating displacement and $Y(f) = 1/Z(f)$ is the mechanical admittance.

Thermal noise affecting GW interferometers can be divided into three main contributions: suspension pendulum mode, suspension violin mode and test mass modes.

2.3.3.1 Suspension pendulum mode

As we will see in section 3.3.1, harmonic oscillators are widely used for seismic attenuation thanks to their frequency domain properties. Using relation 2.26 for a low loss oscillator with resonance frequency ω_0, elastic constant k and mass m, we obtain

$$\widetilde{x}^2_{SPM} = \frac{4 k_B T \omega_0^2 Q}{m\omega \left[Q^2 \left(\omega_0^2 - \omega^2\right)^2 + \omega_0^4 \right]} \tag{2.27}$$

The parameter Q is the quality factor of the oscillator defined as the ratio $Q \equiv \omega_0/\Delta\omega$ between the resonance frequency and the full width at half maximum. Since, in the low and high frequency ranges ($\omega \ll \omega_0$, $\omega \gg \omega_0$), $\widetilde{x}^2_{therm}$ is inversely proportional to the quality factor, the use of high Q suspensions reduces thermal noise.

We can now understand why a pendulum is a better choice for a suspension than an helicoidal spring. In facts there are two forms of dissipation in a pendulum, one due to viscous friction with gas, the other caused by the elasticity of the wire. While the first contribution can be eliminated using vacuum, the second can only be reduced and depends by the geometry and the material of the wire. The dilution factor, given by the ratio between the pendulum effective spring constant mg/l due to gravity and the elastic constant of the wire, is a relative measure of the elastic contribution to the energy dissipation. For a metallic wire, $Q \simeq 10^6$ and dilution factors of 10^2 are typical. This means that the quality factor of a metallic pendulum is 100 times higher than an helicoidal spring made of the same metal. Using fused silica, the same materials in which the interferometer mirrors are made, $Q \simeq 10^7$ and dilution factors of 10^3 have been reported [23].

2.3.3.2 Suspension violin modes

In a real suspension the resonances of the wire itself, called violin modes, appear in the system frequency response. The k-th harmonic of these modes resonance

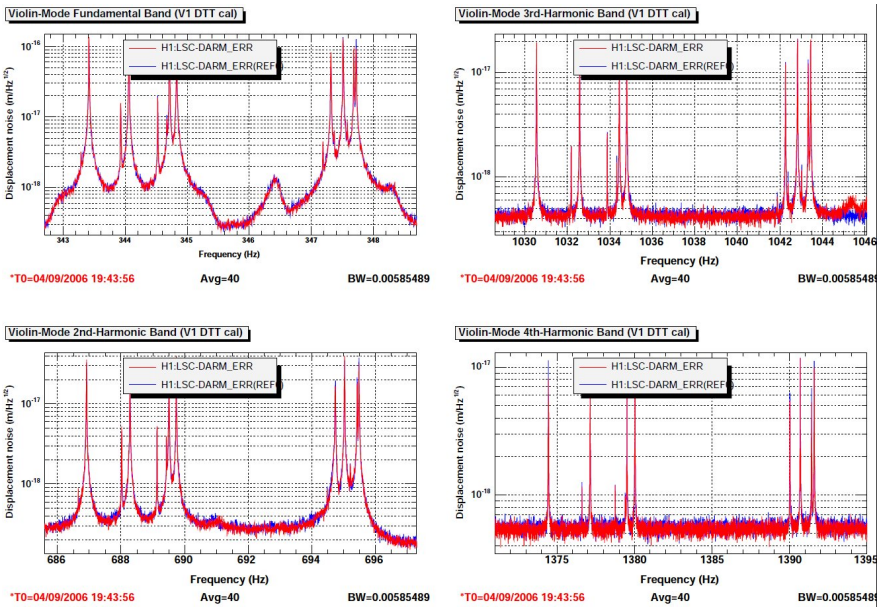

Figure 2.6: Violin modes of LIGO Hanford 4 km interferometer triple pendulum suspensions. In the plots are shown the first four harmonics measured during S5 run (red spectra) and compared with the reference (blue spectra).

frequency can be written as

$$\omega_k = \pi k \sqrt{\frac{mg}{nm_w l}} \tag{2.28}$$

where m is the mass of the mirror, n is the number of wires connecting the mirror to the suspension point, m_w is the mass of wire and l is the pendulum length. Since the Q of the violin modes are approximately equal to the pendulum mode quality factor, the thermal noise can be obtained simply substituting ω_0 with ω_k in 2.27 and summing over the harmonics

$$\tilde{x}^2_{SVM} = \frac{4k_B T}{m\omega} \sum_k \frac{\omega_k^2 Q}{\left[Q^2\left(\omega_k^2 - \omega^2\right)^2 + \omega_k^4\right]} \tag{2.29}$$

Fig. 2.6 shows the first 4 harmonics of triple pendulum suspension (see 3.3.1.2) violin modes measured during S5 LIGO science run.

2.3.3.3 Test mass modes

There are three different dissipation processes involved in the thermal noise of GW interferometer test masses: the bulk Brownian noise, the thermoelastic noise and the mirror coating noise. The first contribution is caused by bistable states distributed homogeneously in the substrate that convert the oscillating energy of the beam into heat, perturbing the mirror's surface position. The thermoelastic noise is produced instead by the oscillating temperature distribution generated by the squeeze and stretch of the mirror substrate. Finally the last

dissipation process is caused by imperfections in the mirror coating material. In facts, in order to reach the high reflectivity required for GW interferometer mirrors, several layers of dielectric materials are deposited on the substrate. Although the amount of material used for coating is small compared to the total mass of the mirror, its mechanical losses can constitute a large contribution to the thermal noise.

Calculating directly the admittance $Y(f)$ to determine the test masses thermal noise would require the highly complex task of measuring the resonance frequency ω_{int} and relative Q_{int} of each internal mode of the optics up to 100 kHz. Thanks to the approach described in [24], the noise spectrum can instead be calculated in terms of the time-averaged dissipated energy W_{diss} when an oscillating force with amplitude F_0 is applied to the mirror surface:

$$\tilde{x}^2_{therm} = \frac{8k_BT}{\omega^2}\frac{W_{diss}}{F_0^2} \tag{2.30}$$

2.3.4 Shot Noise

The shot noise is a fundamental disturbance associated to the quantum nature of light that poses a limitation on power measurements. This process is caused by the Poissonian distributed counting of the photons hitting the interferometer photodetector. The average number of photons N of frequency ν, impinging on a photodiode of quantum efficiency η, in a time interval Δt can be written as

$$N = \frac{\eta P_{ASY}\Delta t}{\hbar 2\pi\nu} \tag{2.31}$$

Since for a Poisson distribution the standard deviation $\sigma = \sqrt{N}$, the corresponding variation in power is

$$\delta P_{shot} = \sqrt{\frac{P_{ASY}\hbar 2\pi\nu}{\eta\Delta t}} \tag{2.32}$$

Therefore the signal to noise ratio can be written as

$$SNR = \frac{|\delta P_{gw}|}{\delta P_{shot}} \tag{2.33}$$

Going back back to 2.13, in the naive assumption of absence of any noise sources, the best choice for the static phase would be $P_{ASY} = \frac{P_{IN}}{2}$, since it's the one that maximize the sensitivity $\frac{\delta P_{ASY}}{\delta\phi}$. This is called the gray fringe condition while the tunings that gives maximum and minimum output power are respectively called bright and dark conditions. In reality, in order to find the best operating point, we have to maximize expression 2.33 respect to the static phase Φ. If we consider the contrast $C \simeq 1$, we get

$$\Phi_{OP} = \pm k\pi \tag{2.34}$$

This is the dark fringe condition and it corresponds to $P_{ASY} = 0$. All modern GW interferometers operate in this condition.

The minimum detectable signal expressed in terms of GW amplitude linear spectral density is found imposing $SNR = 1$

$$\tilde{h}_{shot} = \frac{1}{L}\sqrt{\frac{\hbar c\lambda}{2\pi\eta P_{IN}}}$$

If we consider an interferometer with its arms constituted by two Fabry-Perot cavities, using the same assumptions and conditions of 2.17, we can write

$$\tilde{h}^{FP}_{shot}(f) \simeq \frac{1}{8\mathfrak{F}L}\sqrt{\frac{\pi\hbar c^2}{\nu P_{IN}}}\sqrt{1+(4\pi f_{gw}\tau_s)^2} \tag{2.35}$$

This means that the interferometer sensitivity is now frequency dependent and $\tilde{h}^{FP}_{shot}(f) \propto f$ for $f > 1/4\pi\tau_s$.

2.3.5 Radiation Pressure

The photons of the beam impinging on the interferometer mirrors transfer twice their momentum. Since, as we have seen, the photons are Poissonian distributed, we expect a displacement fluctuation of the mirrors $\tilde{h}_{rp} \propto \sqrt{P_{IN}}$. The radiation pressure noise spectrum is indeed

$$\tilde{h}_{rp}(f) = \frac{1}{mLf^2}\sqrt{\frac{\hbar P_{IN}}{2\pi^3 c\lambda}} \tag{2.36}$$

2.3.6 Optical Readout Noise

The radiation pressure and the shot noises can be considered as two aspects of a single disturbance called optical readout noise

$$\tilde{h}_{ro} = \sqrt{\tilde{h}^2_{shot} + \tilde{h}^2_{rp}} \tag{2.37}$$

While the shot noise is white, the radiation pressure dominates at low frequencies since in this range we have $\tilde{h}_{rp} \propto 1/f^2$. This is related to the quantum nature of the phase measurement process. Even though an interferometer is clearly a macroscopic system, the measurement precision required to detect gravitational waves is so high that it can be considered as an Heisenberg microscope. The shot noise and the radiation pressure are conjugate phenomena: if we increase the laser power in order to lower the shot noise, we increase also the low frequency radiation pressure noise. However for any given frequency f_0 there is an optimal power value P_{opt} that minimize the readout noise spectral density $\tilde{h}_{ro}$

$$P_{opt} = \pi c\lambda m f_0^2 \tag{2.38}$$

Substituting P_{opt} in 2.37, we get the quantum limitation to any interferometer sensitivity:

$$h_{QL} = \frac{1}{\pi f L}\sqrt{\frac{\hbar}{m}} \tag{2.39}$$

For a Fabry-Perot interferometer, the equations 2.37 and 2.38 depends by the finesse $\mathfrak{F}$, since the folding decrease the phase noises but increases displacement

fluctuations:

$$\tilde{h}_{ro}^{FP} = \sqrt{\left(\frac{\pi}{2\mathfrak{F}}\right)^2 \tilde{h}_{shot}^2 + \left(\frac{2\mathfrak{F}}{\pi}\right)^2 \tilde{h}_{rp}^2} \tag{2.40}$$

$$P_{opt}^{FP} = \left(\frac{\pi}{2\mathfrak{F}}\right)^2 P_{opt} \tag{2.41}$$

As expected, the quantum limit 2.39 is instead independent by the interferometer configuration.

2.3.7 Laser Instabilities

Frequency and amplitude instabilities of the laser can couple in many ways with the interferometer differential arm signal. The amplitude fluctuation frequency components, corresponding to the interferometer detection band, can propagate to the antisymmetric port causing a strain noise

$$\tilde{h}_{afn} = \frac{\Delta L_{rms}}{L}\frac{\Delta P}{P_{avg}} \tag{2.42}$$

where ΔL_{rms} is the root mean squared of the arm length difference respect to the dark fringe condition and P_{avg} is the average power. Since $\Delta L_{rms} \simeq 10^{-12}$ m, the requirement is $\Delta P/P < 4 \cdot 10^{-6}$. As we will see in the next chapter, power fluctuations are stabilized with a feedback loop in both LIGO and Virgo.

The frequency noise is transmitted to the antisymmetric port due to unavoidable asymmetries between the arm lengths ΔL, the cavity finesses $\Delta\mathfrak{F}$ and the cavity losses ΔP_{losses}. The induced strain spectral noise can be written as

$$\tilde{h}_{lfn} = \frac{\Delta\nu}{\nu}\left(\frac{\Delta L}{L} + \frac{\Delta\mathfrak{F}}{\mathfrak{F}} + \frac{\Delta P_{losses}}{P_{losses}}\right) \tag{2.43}$$

Assuming a global asymmetry of a few percent, in order to reach the sensitivity goal of modern interferometers (see next chapter), we need to have $\Delta\nu < 1 \cdot 10^{-6}$ Hz/$\sqrt{\text{Hz}}$ at 100 Hz. Since the typical frequency noise of a laser is about 8 orders of magnitude greater than this value, multiple stages of active stabilization are required.

2.4 Power and Signal recycling

The next generation of detectors, like Advanced LIGO (AdLIGO) and Advanced Virgo, will use both signal and recycling cavities. Looking back at the equation 2.11, we note that, operating in dark fringe condition and in case of perfect contrast, $C = 1$, all the beam power is reflected towards the laser. The idea behind power recycling is to put a mirror between the light source and the beam splitter (see both LIGO and AdLIGO optical schemes of fig. 3.1 and fig. 3.2). This is equivalent to consider the rest of the interferometer as a single mirror coupled with the recycling mirror in order to create a single Fabry-Perot cavity with variable finesse. In this way we increase the field stored in the interferometer. The maximum recycling gain G_{rec} is defined as the inverse of how much light is lost per cycle in the interferometer. In present detectors

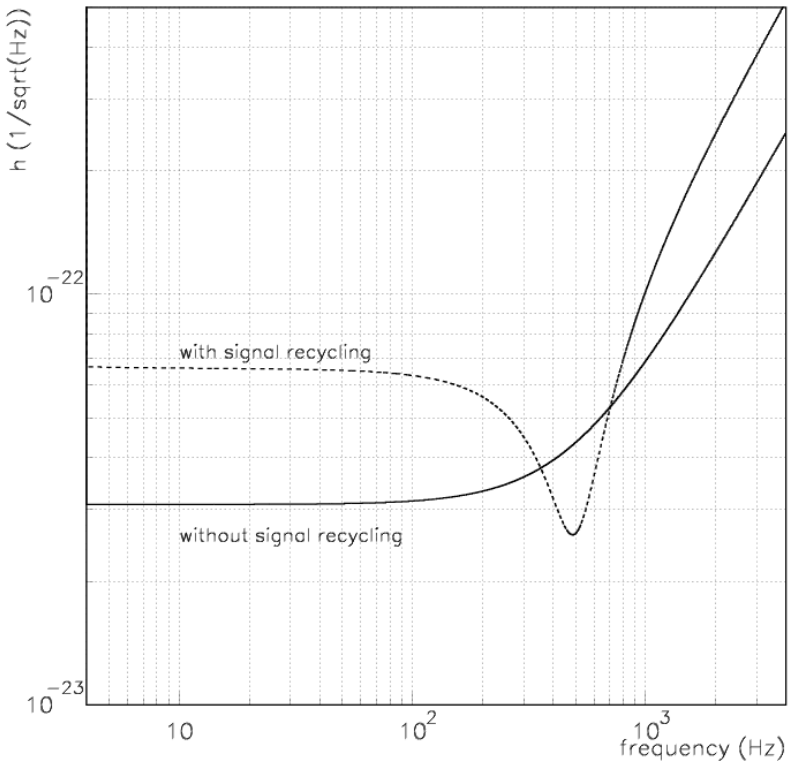

Figure 2.7: Effects of signal recycling on the sensitivity curve of a recycled Fabry-Perot Michelson interferometer [25].

G_{rec} ~60 (see table 3.1 in the next chapter). This ultimately reduces the shot noise by a factor $\sqrt{G_{rec}}$.

The signal recycling scheme uses a party reflecting mirror at the antisymmetric port (fig. 3.2). This allows to tune the sensitivity of the interferometer in a specific gravitational wave bandwidth. As in the case of the power recycling scheme, the signal recycling mirror and the rest of the interferometer constitute a single Fabry-Perot cavity. But the cavity, instead of being resonant at the laser frequency f_l, it resonates at $f_l \pm f_{GW}$. So the sensitivity in this interval is increased by the resonance quality factor. The price to pay is a degraded sensitivity outside this range, which can be tuned by changing the signal recycling mirror reflectivity. An example of such effects on the sensitivity curve of a recycled Fabry-Perot Michelson interferometer is shown in fig. 2.7.

Chapter 3

LIGO and Virgo Interferometers

The Laser Interferometer Gravitational-Wave Observatory (LIGO) is an experiment, coordinated by the California Institute of Technology (Caltech) and the Massachusetts Institute of Technology (MIT), dedicated to the detection and study of gravitational waves. The experiment consists of three in-vacuum Michelson interferometers with 4 km Fabry-Perot resonant optical cavities. Two interferometers, one with 4 km and one with 2 km arm length (called H1 and H2), share the same vacuum envelope in Hanford, Washington. The third one, with 4 km arms, is located in Livingston, Louisiana (labeled L1). Technical and scientific research in LIGO is organized through the LIGO Scientific Collaboration (LSC), constituted by 55 (as 2008) international colleges, universities and research institutions.

Virgo, located in Cascina, Pisa, Italy, is a Michelson gravitational wave interferometer with 3 km Fabry-Perot cavities. The experiment has been developed and built by a French-Italian collaboration (VSC) founded in 1989. Currently the VSC counts about 250 members from several French, Italian, Dutch, Polish and Hungarian institutions.

3.1 Optical Schemes

3.1.1 LIGO Optical Design

3.1.1.1 Initial LIGO

The initial LIGO detectors [26] have been designed to be sensitive to GWs with strain amplitude as small as 10^{-21} and frequency in the band 40-7000 Hz . The three interferometers (H1, H2, L1) adopt the power-recycled Michelson optical scheme with Fabry-Perot arm cavities (fig. 3.1).

The test masses are 11 kg cylinders of 25 cm diameter and 10 cm depth made with fused silica substrates. The mirror surface consists of multilayer dielectric coatings manufactured to have an absorption loss of a few parts-per-million (ppm) and scattering loss of 60-70 ppm.

The light source is a 10 W Nd:YAG laser, operating at 1064 nm, that is both

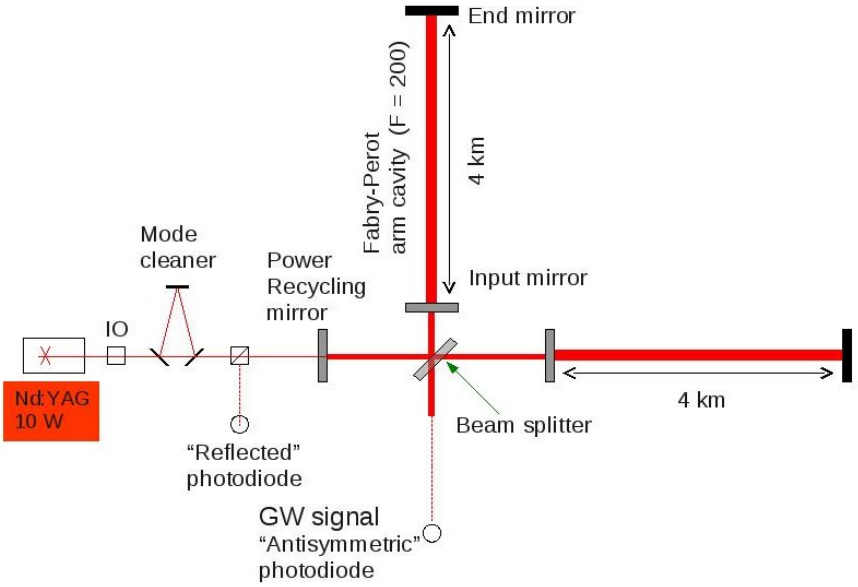

Figure 3.1: Initial LIGO optical scheme. The Input Optics (IO) block contains the laser stabilization and the phase modulators.

intensity and frequency stabilized. The power stabilization is implemented by directing a sample of the beam to a photodetector, filtering its signal and feeding it back to the power amplifier. Using this servo the laser power fluctuations are reduced to $\sim 10^{-7}/\sqrt{\text{Hz}}$ at 100 Hz. In order to keep the frequency noise below to $\sim 10^{-2}$ Hz$/\sqrt{\text{Hz}}$, a two-stage high bandwidth (500 kHz) feedback loop is adopted. After the stabilization the laser beam is phase-modulated with two RF sine waves producing two pairs of sidebands at 24.48 MHz and 61.2 MHz called resonant and non-resonant sidebands. The beam then reaches the mode-cleaner, a 12 m cavity transmissive triangular cavity that is designed to transmit the carrier and both the sidebands and additionally filters the laser noise above 1 MHz. After the mode-cleaner, the beam hits the power recycling mirror that reflects the non-resonant sidebands and increases the carrier and sideband powers by a factor 50 and 26.5 respectively. Finally the beam reaches the 50/50 beamsplitter and then the two input mirrors. Inside the Fabry-Perot cavities of finesse $\mathfrak{F} = 220$, the circulating power of the carrier, the only mode resonant, is about 15 kW.

3.1.1.2 Advanced LIGO

Advanced LIGO is the first major upgrade to the LIGO gravitational wave interferometers [27]. The sensitivity goals of the detectors are chosen to enable the advance from plausible gravitational wave detection to likely detection and rich observational studies of sources. Advanced LIGO promises an improvement over initial LIGO in the limiting sensitivity by more than a factor of 10 over the entire initial LIGO frequency band. It also increases the bandwidth of the instrument to lower frequencies (from 40 Hz down to 10 Hz) in order to allow the detection of black holes inspirals and unmodeled transient sources. Table 3.1

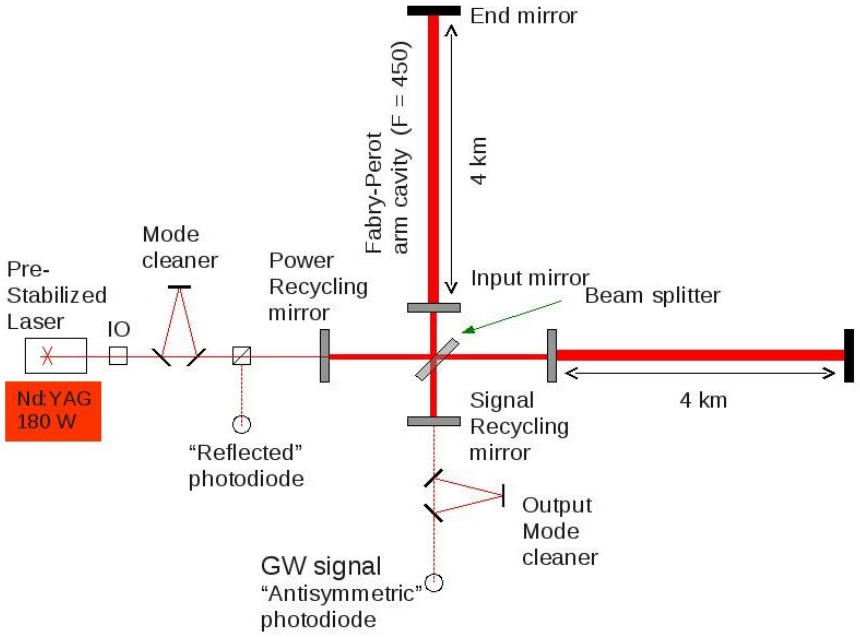

Figure 3.2: AdLIGO optical scheme

summarizes the differences between initial LIGO implementation and AdLIGO reference design parameters.

The AdLIGO optical configuration is a Fabry-Perot Michelson interferometer with dual recycling. The optical components that are introduced in AdLIGO, as shown in fig. 3.2, are the signal recycling mirror, the output mode cleaner cavity. The output mode cleaner is a triangular cavity used to filter out non-TEM_{00} mode carrier power. This greatly decrease the power that reached the antisymmetric photodiode, lowering the shot noise with only a small reduction in signal.

The finesse of the Fabry-Perot cavities is increased to 450. The laser is prestabilized and its power is increased to 180 W with more than 90% of the beam at the fundamental mode TEM_{00}. The resulting circulating power in the arms is roughly 800 kW. The Nd:YAG pre-stabilized laser design resembles that of initial LIGO, but with the addition of a more powerful output stage.

Respect to initial LIGO, the fused-silica mirrors for Advanced LIGO are larger in diameter (~32 cm) to reduce thermal noise contributions and more massive (~40 kg) to keep the radiation pressure noise to a level comparable to the suspension thermal noise. The test masses are suspended by fused silica tapered fibers, in contrast to the steel wire suspensions used in initial LIGO. Fused silica has much lower mechanical loss (higher Q) than steel, and the fiber geometry allows more of the energy of the pendulum to be stored in the earth's gravitational field while maintaining the required strength, thereby reducing suspension thermal noise.

Parameters	Initial LIGO implementation	AdLIGO reference design
Observatory arm lengths (H1, H2, L1)	4 km, 2 km, 4 km	4 km, 4 km, 4 km
Minimum strain noise (rms on 100 Hz band)	4×10^{-22}	$< 4 \times 10^{-23}$
Displacement sensitivity at 150 Hz	$\simeq 1 \times 10^{-19}$ m/$\sqrt{\text{Hz}}$	$\simeq 1 \times 10^{-20}$ m/$\sqrt{\text{Hz}}$
Laser wavelength	1064 nm	1064 nm
Arm cavity finesse	220	450
Storage time	0.84 ms	1.7 ms
Optical power at laser output	10 W	180 W
Optical power on test masses	15 kW	800 kW
Power recycling gain (G_{rec})	60	45
Input mirror transmissivity	3%	1.4%
Test masses	Fused silica, 11 kg	Fused silica, 40 kg
Mirror diameter	25 cm	34 cm
Suspension configuration (BSC chambers)	4 passive stages (Stacks)	4 passive stages (QUAD) + 3 active stages (HEPI + BSC-ISI)
Suspension wire fibers	Steel wires	Fused silica

Table 3.1: Comparison between initial LIGO implementation and AdLIGO reference design parameters

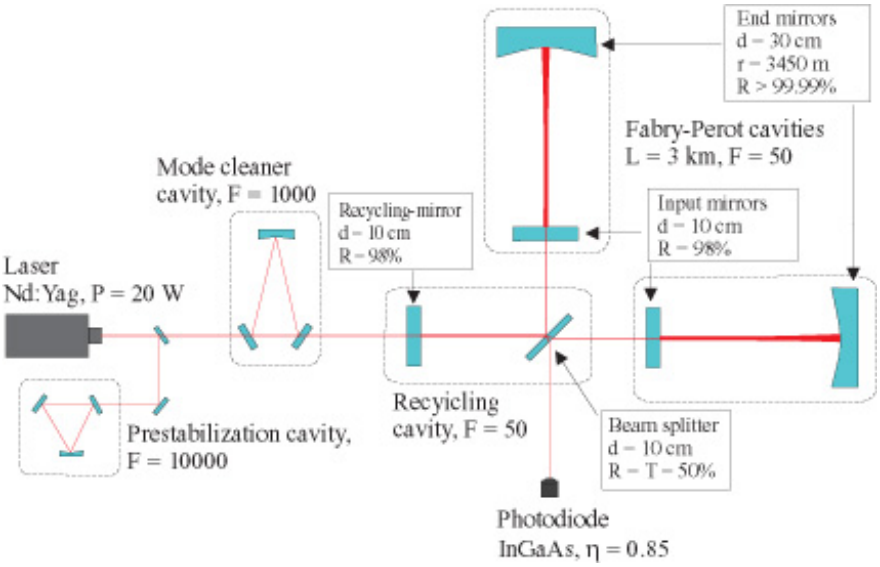

Figure 3.3: Virgo Optical Design.

3.1.2 Virgo Optical Design

Virgo optical scheme is shown in fig. 3.3. The principal components are

- The laser: it's a Nd:Yag with λ =1064 nm.
- The injection bench: it's constituted by the prestabilization cavity, used to stabilize the laser frequency, by the mode cleaner input and output mirrors and by the optics needed for alignment.
- The Fabry-Perot cavities: they are 3 Km long with a finesse $\mathfrak{F} = 50$.
- The mode cleaner: it's a triangular cavity about 150 m long with $\mathfrak{F} = 1000$. Two mirrors (the input and output mirrors) are mounted on the injection bench, the third one is separated and connected to the injection through a dedicated tube.
- The power recycling cavity: it's constituted by the recycling mirror and by the interferometer itself. It's able to amplify the laser power by a factor 50 (1000 W at the *beam splitter*).
- The detection bench: it supports the output mode cleaner (a small triangular cavity designed to increase the contrast) and the optics needed to collimate the beam on the photodiodes. Outside there is an optical bench where are located the photodiodes (InGaAs with quantum efficiency $\eta = 0.85$) used for the locking and the signal detection.

3.2 Vacuum systems

In order to isolate the test masses from acoustic noise and reduce the phase noise, all the main VIRGO and LIGO optical components and beam paths are

Figure 3.4: Vacuum system of the Hanford interferometer.

enclosed in ultrahigh vacuum systems.

3.2.1 LIGO Vacuum system

The LIGO vacuum system (fig. 3.4) was designed and constructed to ensure that phase noise associated with scatter from residual gas species would allow strain sensitivities of order 10^{-25} $1/\sqrt{Hz}$. To achieve this level of vacuum quality (10^{-7}-10^{-8} mbar), great care in the control of air leaks and residual hydrocarbon contamination was required.

Two kinds of vacuum chambers are used in LIGO: Beam Splitter Chambers (BSC) and Horizontal Access Module chambers (HAM). BSCs are approximately 5.5 m high and hold the beam splitter and the main interferometer mirrors. Each of the two interferometers at Hanford uses five BSC chambers for a total of ten chambers. HAMs are smaller chambers used for the Mode Cleaner and the Recycling cavity mirrors. The 4 km beam tubes have been built with stainless steel processed to remove hydrogen and all their welded parts have been baked out for many days. In this way it's possible to reach the required level of vacuum only pumping from the ends of the tubes.

3.2.2 Virgo Vacuum system

Virgo vacuum system can guarantee a partial pressure of 10^{-9} mbar for hydrogen. An even stronger limit, 10^{-14} mbar, is reached for gaseous hydrocarbons, since these compounds can stick on the mirrors surface, degrading their reflectivity. Even though the towers containing the superattenuators (see next section) are under vacuum, the presence of cables and electronics components of the control system does not allow to reach the ultra-high vacuum levels of the

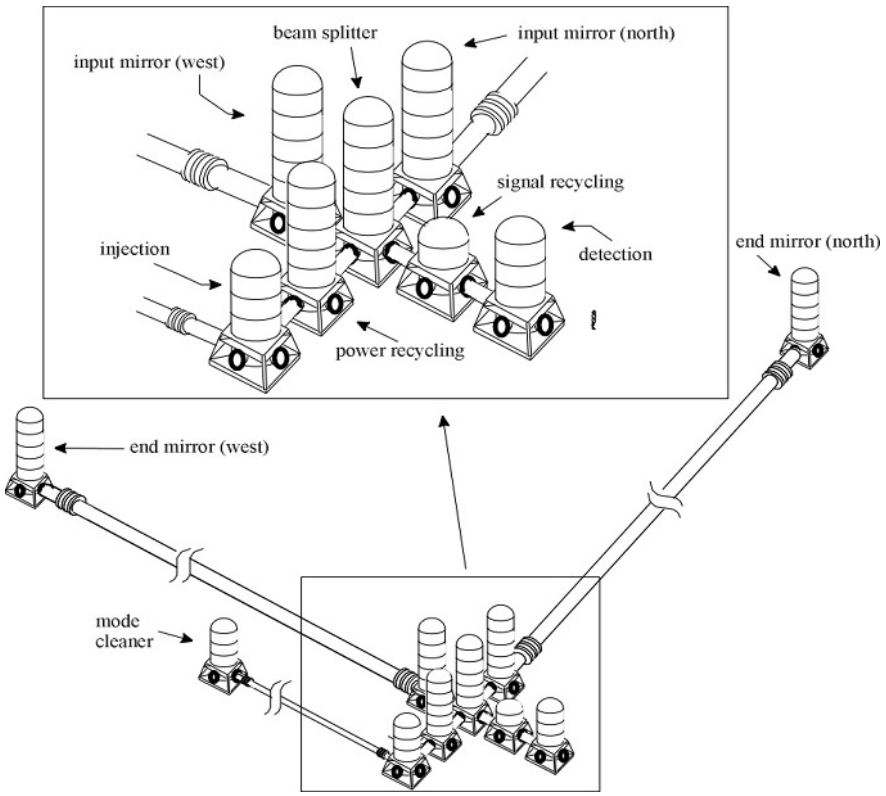

Figure 3.5: Virgo vacuum system

tubes. To solve this problem, every tower is divided in two sections that communicates only through a narrow conductance hole necessary for the passage of the metallic wire that sustains the last stage of the superattenuator. The electronics is located in the upper section and is maintained at 10^{-6} mbar of pressure. Fig. 3.5 shows the complete system: the tubes have a diameter of 1.2 m and are divided in 15 m sections. The overall volume, about 7000 m^3, makes Virgo the greatest vacuum system in Europe.

3.3 Seismic attenuation

As we have previously mentioned, the ground motion is the main low frequency noise source for all terrestrial gravitation wave detectors.

Even though theoretically only the seismic noise components directed along the beam should effect a GW interferometer, the earth curvature and the mechanics of the suspensions introduce unavoidable couplings between all the degrees of freedom. Since the seismic noise have to be reduced by over 11 orders of magnitude, a seismic attenuation system must therefore be able to attenuate along all the 6 degrees of freedom.

Two approaches are possible in the design of seismic attenuation systems:

- passive seismic attenuation

- active seismic attenuation

3.3.1 Passive seismic attenuation

The idea behind passive attenuation is to use the fundamental property that the response of a harmonic oscillator to seismic excitation is equivalent to a second-order low pass filter. The main advantage of this approach is that, since the use of controls is kept to a minimum, the attenuation performance depends only by the mechanical parts and is not limited by the actuators and sensors. This makes the system extremely reliable over time. LIGO seismic isolation stacks, LIGO/GEO600 triple and quadruple pendulums, Virgo superattenuator, HAM-SAS, that will be described in the next subsections and in the next chapter, are all examples of passive attenuation systems.

The simplest passive isolator we can consider is an unidimensional spring with elastic constant k connected to a pointlike mass M. The equation of motion is

$$M\ddot{x} = -k(x - x_0) \tag{3.1}$$

Defining the transfer function of a linear system as the ratio between the Fourier transform of the output and the Fourier transform of the input, we can write

$$H_X \equiv \frac{X}{X_0} = \frac{\omega_0^2}{\omega_0^2 - \omega^2} \tag{3.2}$$

where $\omega_0 = \sqrt{k/M}$. If instead we apply to the mass an external force f, calculating the ratio between the Fourier transforms F and F_0, we get the force transfer function

$$H_F \equiv \frac{F}{F_0} = \frac{1}{\omega_0^2 - \omega^2} \tag{3.3}$$

As shown by the cyan and yellow curves of fig. 3.6, for frequencies $\omega \gg \omega_0$, $H_x, H_F \propto 1/\omega^2$. Therefore in the frequency domain a simple spring is equivalent to a low pass filter with two conjugate poles at ω_0^2.

Now, we are going to consider the spring massive and introduce viscous damping. Exciting the mass M with an external force f, assuming again unidimensional motion along the $\hat{x}$ axis, we can write:

$$M\ddot{x} + m\ddot{x_0} + k(1 + i\phi)(x - x_0) + \gamma\dot{x} = f \tag{3.4}$$

where m is the mass of the spring, γ is the damping coefficient, ϕ is the so called loss angle, a measure of the spring anelasticity. For an undamped low loss spring ($\phi \ll 1$), ϕ is approximately equal to the inverse of the oscillator quality factor, $\phi \simeq 1/Q$. Fourier transforming expression 3.4, we obtain:

$$-M\omega^2 X - m\omega^2 X_0 = -k(1 + i\phi)(X - X_0) - i\gamma\omega X + F \tag{3.5}$$

We can now write the displacement and force transfer functions:

$$H_X = \frac{\omega_0^2(1 + i\phi) + \frac{m}{M}\omega^2}{\omega_0^2(1 + i\phi) - \omega^2 + i\frac{\gamma}{M}\omega} \tag{3.6}$$

$$H_F = \frac{1}{\omega_0^2(1 + i\phi) - \omega^2 + i\frac{\gamma}{M}\omega} \tag{3.7}$$

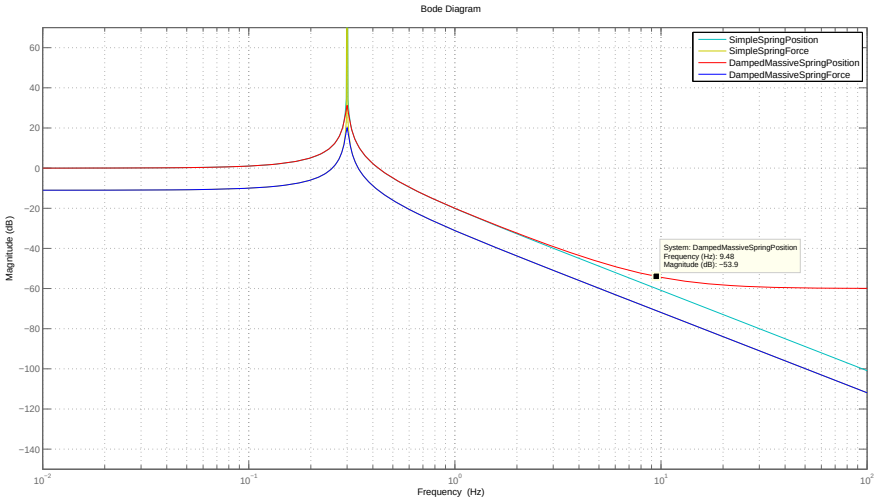

Figure 3.6: Position and Force transfer function magnitudes of a simple massless spring (cyan and yellow curves) and a massive viscously damped spring (blue and green curves) with $f_0 = 300$ mHz, $M = 1$ kg, $m = 0.001$ kg, $\gamma = 0.05$, $\phi = 0.001$. The label shows the cutoff frequency ($\omega_c/2\pi$) above which the position transfer function of the massive spring saturates.

As shown in the plots of last expressions magnitudes (blue and green curves of fig. 3.6), we can define a cutoff frequency $\omega_c = \sqrt{M/m}\omega_0$ above which the transfer function H_X saturates at the level m/M. This means that, for a real massive spring, the region of $1/\omega^2$ attenuation is limited to the interval between ω_0 and ω_c.

3.3.1.1 LIGO Seismic isolation stacks

The Seismic isolation stack (fig. 3.7) is a traditional mass-spring passive dampening system, used in initial LIGO, that is able to provide 120 dB of horizontal and vertical attenuation at 50 Hz [28]. It consists of several layers (four or three depending on the isolation requirements) of massive elements separated by sets of coil springs stuffed with constrained layers of damping material. The system is designed to have all its resonance frequencies in the 1.5-15 Hz range. The damping material is sandwiched between aluminum slugs and phosphor bronze walls, prior to coiling the springs. End caps are then e-beam welded onto the open ends of each coil to prevent contamination of the vacuum by the lossy damping material inside the spring. This results in a soft spring with mechanical $Q \sim 30$. In order to compensate the interferometer alignment for earth tides, the stacks installed on the end mirrors are equipped with fine actuators that are able to translate the system together with the optic suspension by 90 μm along the beam axis in a DC-10 Hz frequency range.

3.3.1.2 LIGO Triple and Quadruple Suspensions

The Triple Suspension passive seismic attenuation device, based on the Triple Pendulum design developed for GEO600 [29] - the German-British gravitational

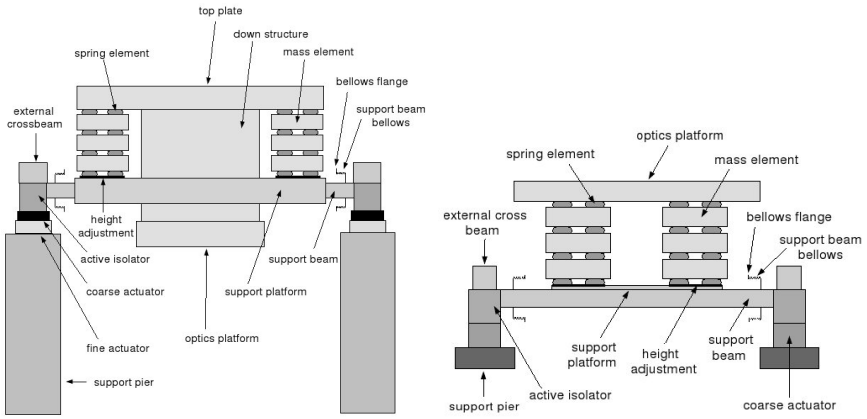

Figure 3.7: Seismic isolation stacks used in initial LIGO BSC (left) and HAM (right) vacuum chambers. A three layer version is used for the input optics.

wave detector -, is made of a chain of three pendulums and is capable of providing 90 dB of horizontal attenuation and 50 dB of vertical attenuation at 10 Hz. It's installed in every HAM vacuum chamber. The system (left photo of fig. 3.8) is composed by three bodies, called top, intermediate, and test mass that weight approximately 3 kg each and provide three stages of passive horizontal attenuation. The T-shaped top mass is suspended from the top of an external cage through two wires connected to two maraging steel blades. The blades are used in order to provide vertical attenuation. The intermediate mass is connected to the top mass through four wires and four maraging blades while the test mass is connected to the intermediate with four silica fibers. Both intermediate and test masses are made of fused silica. The triple pendulum has also 14 sensors and actuators, 6 on the top mass and 4 on both the intermediate and test masses, called OSEMs (Optical Sensor and ElectroMagnetic actuator). The top mass sensors and actuators are used for 6-degrees of freedom active damping of the structure resonances.

The input and end mirrors of AdLIGO will be suspended via a Quadruple pendulum system (Quad) [30]. The Quad is designed to attenuate seismic noise by about 120 dB and 70 dB at 10 Hz in the horizontal and vertical direction respectively. As shown in fig. 3.8, the Quad mechanical design is essentially the same of the Triple except for the number and weight of the masses. The suspension is composed by two steel T-shaped bodies of 22 kg each, called top and upper intermediate masses and two cylinders made of fused silica, called penultimate and test masses, that weight 40 kg each. In order to decrease the thermal noise, these last two stages are designed to be monolithic in the sense that the masses are connected through four tapered silica fibers that are pulled and welded with a CO_2 laser based machine developed specifically for this task [27]. Each of the four masses are suspended from two cantilever-mounted, approximately trapezoidal, pre-curved, blade springs, and four steel wires, of which two are attached to each blade. The blade springs are stressed to about half of the elastic limit. The upper suspension wires are not vertical and their lengths and angles gives some control over the mode frequencies and coupling factors. The Quad solid-body modes are damped using OSEMs capable of

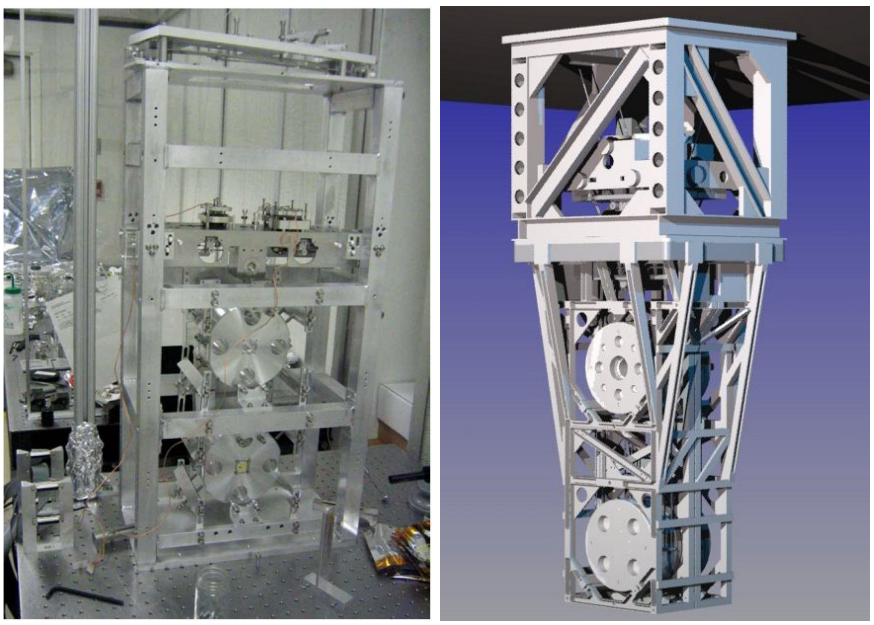

Figure 3.8: A photo of the triple suspension (left), CAD 3D drawings of the Quad (right)

0.1 nm sensitivity at 1 Hz on the upper stages and electrostatic actuators on the mirror itself with switchable high- and low-force modes for acquisition and operation respectively.

3.3.1.3 Virgo superattenuator

In order to get an uniform and gradual attenuation in all the degrees of freedom, the superattenuator (SA) has been designed as a chain of mechanical filters in cascade [31].

The SA, shown in fig. 3.9, can be essentially divided in three sections:

- the standard filters chain
- the pre-isolation stage
- the mirror control system

The entire chain, constituted by 6 filters, is about 10 m long and therefore has a main resonance frequency of $\frac{1}{2\pi}\sqrt{\frac{g}{l}} = 0.16$ Hz. The first and last stages, called filter 0 and filter 7, host the active controls of the suspension. Some of the interferometer optical components require a lower level of seismic attenuation: the injection bench, the detection bench and the mode-cleaner terminal mirror are suspended from smaller SAs, about 2 m long, called short towers.

The standard filters Each of the 4 standard filters is designed to reduce the propagation of mechanical vibrations by 2 orders of magnitude for frequencies greater than 10 Hz. The central body of the filter (see fig. 3.10) is constituted

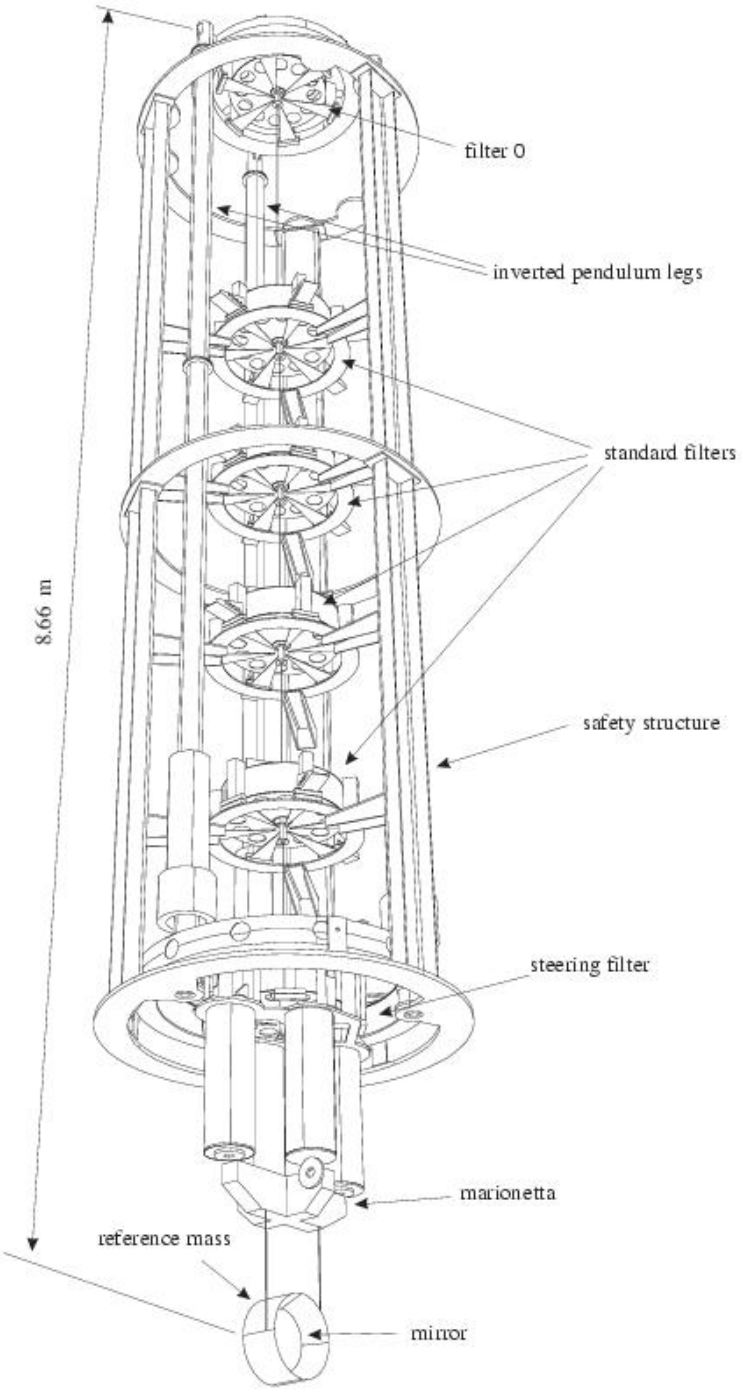

Figure 3.9: View from below of the VIRGO long superattenuator. We can distinguish two of the three legs of the inverted pendulum and, from the top to the bottom, the filter 0, the standard filters 1 to 4, the steering filter, the marionetta and the mirror–reference mass system.

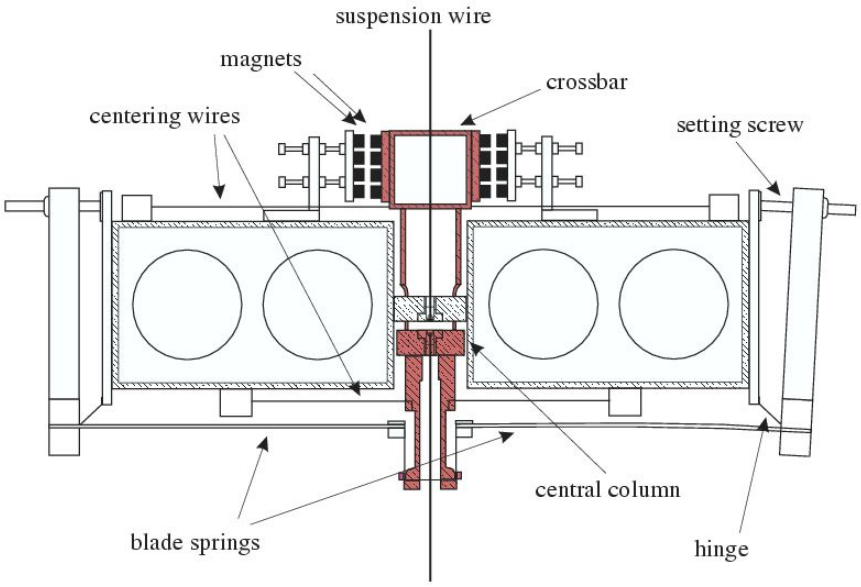

Figure 3.10: Section of a standard filter. The part in red can move with respect to the body of the filter.

by a rigid steel cylinder of 70 cm of diameter, 18.6 cm of height and 100 Kg of weight. The choice of these parameters is motivated by the need of an high moment of inertia in order to have the lowest rotational modes frequencies. The load of the lower stages is sustained through a series of elastic triangular blades that, working as springs, are responsible for the vertical attenuation. Thanks to their shape, the stress distribution, that is maintained at 2/3 of the material elastic limit, is uniform along the blade. Every blade is bent before mounting, so it can assume an horizontal configuration after being loaded. After several studies on the subject, the best material treatment to reduce the *creeping* of the metal has been identified [32].

The Pre-isolator The passive filters chain is suspended from a stage dedicated to low frequencies attenuation called pre-isolation stage [33]. This stage is a mechanical oscillator along $\hat{x}$, $\hat{y}$, $\hat{z}$, $\hat{\theta}_z$ with very low resonance frequencies ($f_0 \simeq 30$ mHz) compared to the standard filters. The system, shown in fig. 3.9, is constituted by three hollow rigid legs, connected to ground through Maraging steel flexible joints, that support a plate called top stage on which the filter 0 is located. The three legs can be physically described by an inverted pendulum (IP) and they are responsible for the horizontal attenuation. A detailed description of IP mechanical properties will be given in next chapters.

Mirror control system The mirror control system is constituted by the marionetta and the steering filter. The latter, also called filter 7, is a standard filter equipped with devices used to control the marionetta. Four columns about 1 m long extend from the bottom of the filter, each supporting a driving coil facing a corresponding magnet fixed to each arm of the marionetta. By driving the

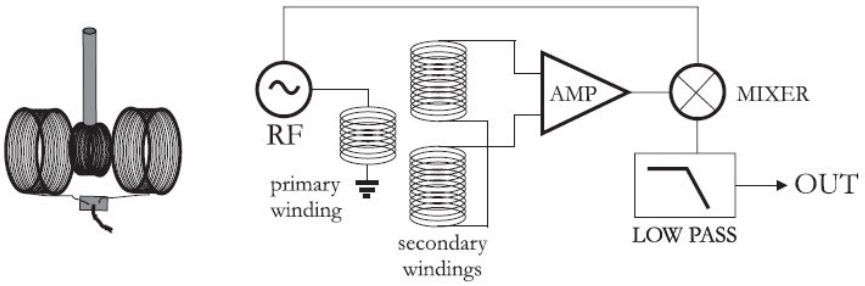

Figure 3.11: Left: sketch of a typical LVDT. Right: Diagram of the electronics used for read-out.

coils with proper currents, forces and torques can be applied to the marionetta in order to control the position of the mirror in the 0.1-1 Hz band.

The marionetta, hanging from the steering filter, is the last stage of the SA. It is essentially a cross shaped structure supporting the mirror and the reference mass, through four looping steel wires.

Final adjustment of the position of the mirror, along the beam direction, above 1 Hz, are applied directly to reference mass that surrounds mirror.

Sensors and actuators As we can see in fig. 3.12, the sensors and actuators, needed to control the IP, are mounted on the SA top stage and disposed in a equilateral triangle configuration. There are two kinds of sensors:

- Linear Variable Differential Transformers (LVDTs): LVDTs are displacement sensors constituted by a primary and secondary windings (fig. 3.11). The primary winding is fed with an audio frequency (usually in the range 10-20 kHz) sinusoidal signal. The secondary winding is composed by two coils wound in opposite directions. When the primary winding is displaced of an amount Δx, a current with the same frequency of the primary signal and modulated in amplitude proportionally to Δx is induced in the secondary winding. A mixer is then required to demodulate the secondary signal and produce a DC output proportional to Δx. Virgo LVDTs are linear within 1 % over a range of 1 cm.

- Accelerometers: they have been designed specifically for Virgo suspensions. The accelerometer mechanical structure is constituted by a brass rod loaded with two disks made of the same metal sustained by two plates of CuBe, in order to form an inverted pendulum [34]. The disks mass is chosen in order to obtain a resonance frequency of around 5 Hz, increasing in this way the device sensitivity to the SA normal modes frequency range. An LVDT of the same type of the one previously described is used to measure the masses positions respect to the suspension point. The device use a feedback control system. The $LVDT$ signal, after being filtered by a proportional–integral–derivative (PID) controller, is sent to a coil located at one end of the rod. The coil is sensible to the field generated by a permanent magnet fixed on the external structure and is able to maintain the system in its equilibrium position working as an electronic spring. The

system can be described by an harmonic oscillator with mass m, resonance frequency ω_0 and quality factor Q. In the frequency domain, the restoring force is proportional to the mass displacement:

$$\frac{f_{FB}}{m} = -F(\omega)[x(\omega) - x_0(\omega)] \tag{3.8}$$

where $F(\omega)$ is the transfer function of the control network. Combining (3.8) with the equation of motion, we get

$$\frac{f_{FB}}{m} = \frac{H(\omega)F(\omega)}{1 + H(\omega)F(\omega)}[-\omega^2 x_0(\omega)] \tag{3.9}$$

where

$$H(\omega) = \frac{1}{-\omega^2 + i\omega\omega_0/Q + \omega_0^2}$$

In the frequency range where the open-loop gain $|H(\omega)F(\omega)|$ is much greater than 1, we have

$$\frac{f_{FB}}{m} = \omega^2 x_0 \tag{3.10}$$

and the restoring force is therefore proportional to the acceleration. The sensitivity of the device is limited essentially by two types of noise: the Johnson noise of the LVDT secondary coil (1 $\mathrm{nV}/\sqrt{\mathrm{Hz}}$ at room temperature) and the noise of the amplifier (0.8 $\mathrm{nV}/\sqrt{\mathrm{Hz}}$). The spectral sensitivity function, defined as the minimum acceleration that induces the spectral noise measured at the output of the demodulator, is flat for frequencies lower than the resonance and can be written as

$$7 \cdot 10^{-10} \frac{\mathrm{m/s^2}}{\sqrt{\mathrm{Hz}}} \tag{3.11}$$

This means that the sensitivity of the device to displacement is

$$8 \cdot 10^{-13} \frac{\mathrm{m}}{\sqrt{\mathrm{Hz}}} \tag{3.12}$$

value that is more than 3 orders of magnitude lower than the seismic noise (see the empirical law 2.20). The amplitude of the output signal can be written as:

$$V_{out} = \sigma(g \sin\theta + \ddot{x}) \tag{3.13}$$

where σ is a calibration parameter and θ is the angle between the accelerometer, located on the top table, and the horizontal direction, called *tilt* angle.

Two types of actuators, electromagnetic and mechanical, are installed on the SA top table:

- coil-magnet: they are constituted by a couple of coils and by a central magnet of cubic shape (4 cm side) connected through a thin metallic beam.
- motor-spring: they are made by two horizontal springs connected to the inverted pendulum legs through a support moved using an endless screw controlled by an electric motor.

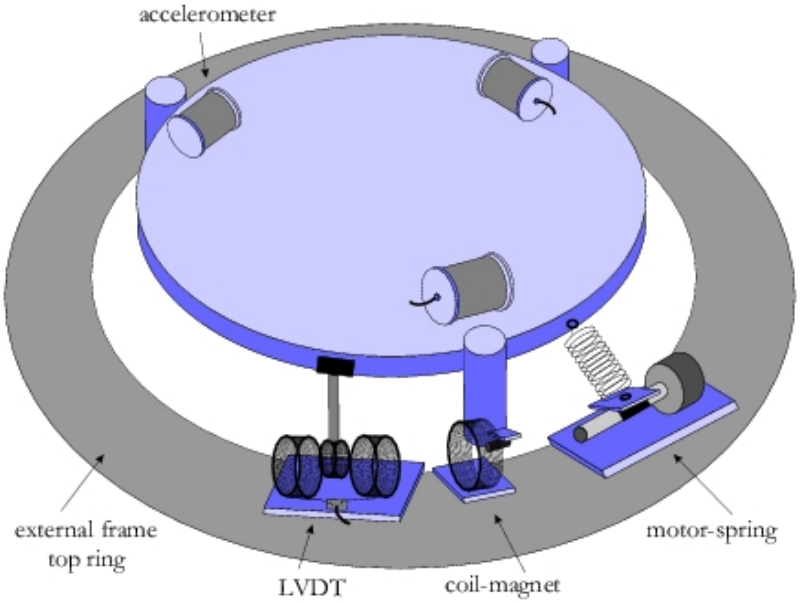

Figure 3.12: The sensors and actuators located on the VIRGO SA top table.

3.3.2 Active seismic attenuation

While the use of active controls in passive seismic attenuation systems is limited only to the damping of the mechanical structure normal modes, active attenuators heavily rely on control systems to reduce the ground motion.

3.3.2.1 HEPI

HEPI is an acronym for Hydraulic External Pre-Isolator [35], which in essence explains its functionality. The vacuum chambers installed at LIGO Livingston Observatory were initially isolated from ground noise by the seismic isolation stacks. This turned out to be inadequate since ground noise caused by passing trains, heavy lumber transportation, etc were amplified by the stack resonance frequencies. Every BSC vacuum chamber of AdLIGO will be equipped with HEPI.

HEPI is an active seismic attenuation system (fig. 3.13), capable of detecting real time ground noise and immediately compensating by displacing the piers of each optics vacuum chamber in a direction opposite of the motion caused by the ground noise, thus maintaining equilibrium for the chamber and its installed optics.

HEPI consists of five equally important mechanical entities:

- Rigid frame capable of supporting the weight of each vacuum chamber corner,
- Offload springs supporting the payload of each corner pier

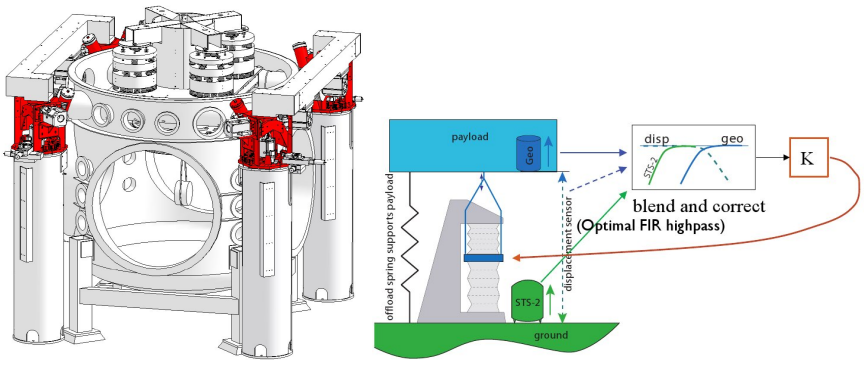

Figure 3.13: Left picture: drawing of a BSC chamber equipped with HEPI (red parts) and with isolation stacks (the crossed structure on top of the chamber). Right picture: diagram of the feedback loop used in HEPI.

- Vertical hydraulic actuator with flexible bellows, driven by a hydraulic servo valve, capable of causing payload offset in the vertical direction
- Horizontal hydraulic actuator with flexible bellows, driven by a hydraulic servo valve, capable of causing payload offset in the horizontal direction.

Geophones and position sensors are used to measure displacement caused by ground noise, giving feedback to the HEPI control system. In right side of figure 3.13 is shown the feedback loop from the seismometer (STS-2) placed on the ground and the geophone (Geo) placed on each corner of the vacuum chamber crossbeam. The feedback signals are passed through a blended and corrected high-pass filter before giving input back to the hydraulic actuation system, taking compensating action.

3.3.2.2 BSC-ISI and HAM-ISI

The BSC and HAM Internal Seismic Isolation systems (BSC-ISI and HAM-ISI) are respectively double- and single-stage active attenuators designed by J. Giaime, B. Lantz and their collaborators at LSU and Stanford University. Their designs are both derived from a prototype built and tested between 1990 and 2000 at JILA laboratory [36]. BSC-ISI and HAM-ISI are capable of providing 40 dB and 70 dB respectively of horizontal and vertical attenuation at 1 Hz. The BSC-ISI, shown in the top picture of fig. 3.14, will be installed in every AdLIGO BSC chamber and is constituted by three sections:

- Stage 0: an external frame designed to be interfaced with the HEPI pre-isolator that holds three pre-bent maraging blade springs connected to Stage 1 with stiffness chosen to obtain resonance frequencies in 2-6 Hz range.
- Stage 1: is the main isolation filter. The structure is designed to have resonance frequencies well above 50 Hz (the unity gain frequency of the servo system) and is connected to the other stages through stiff maraging blade springs. The signals used for control are obtained blending three sensors for each degree of freedom: two inertial sensors, a Streckeisen STS-2

broadband seismometer and a Geotech Instruments GS-13 geophone, that measure the platform motion respect to their suspended test masses and a position sensor that measures the displacement respect to the adjacent stage. The actuators consist of permanent magnets and non-contacting voice coils.

- Stage 2: supports the QUAD suspension. The stage is controlled using a position sensor and a geophone for each degree of freedom and the Stage 1 seismometer signals.

HAM-ISI is designed to respect the less stringent AdLIGO requirements (see next chapter) for the HAM chambers. It is constituted by

- Stage 0: a 190x150x10 cm aluminum plate supporting three posts that pass through next stage and hold three blade springs, with the same characteristics of those used in BSC-ISI, connected to Stage 1 through 4 mm thick maraging steel rods.

- Stage 1: the stage mechanics has been designed in order to be very stiff to bending and have high resonance frequencies. The structure, shown in bottom picture of fig. 3.14, is a thin walled hexagonal aggregate of closed cells separated by vertical plates. Stage 1 hosts all the sensors and actuators used for control: 6 GS-13s (the gray cylinders) that provide high frequency information (between 500 Hz and 0.5 Hz), 6 displacement sensors that provide alignment and low frequency information (between 10 Hz and DC), 3 horizontal actuators that are adjacent to the horizontal GS-13s and 3 vertical actuators located below the vertical GS-13s.

- Optical Table: an hexagonal platform circumscribed around a 193 cm circle that support the payload.

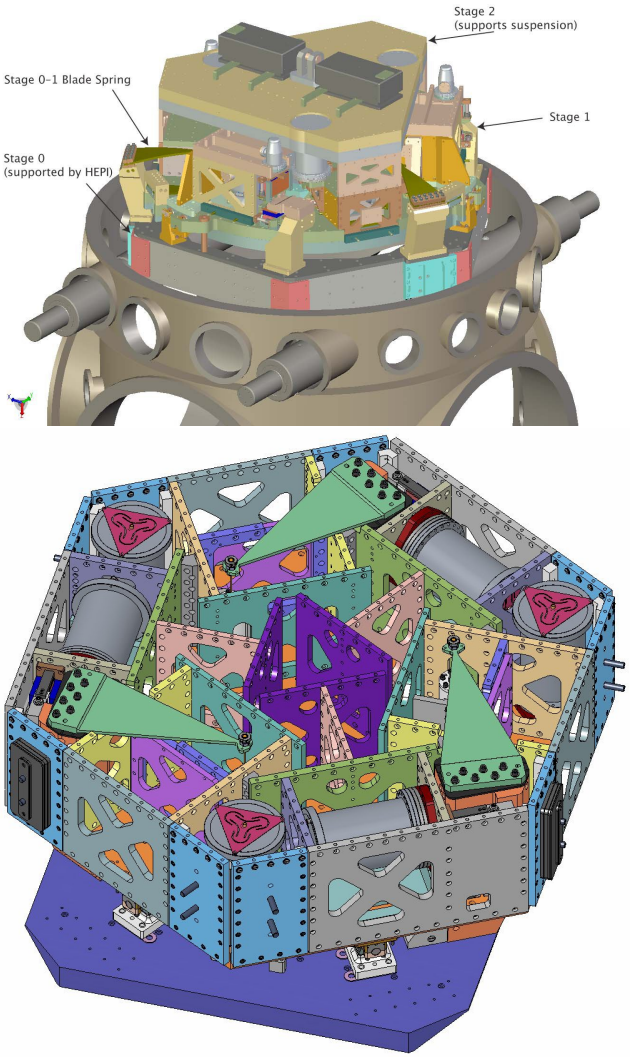

Figure 3.14: CAD rendering of the BSC-ISI (top) installed in its vacuum chamber. Top view of the HAM-ISI isolation stage (bottom) with the table top removed to show the placement of major components .

Part II

HAM-SAS Modeling

Chapter 4

HAM Seismic Attenuation System

4.1 HAM-SAS Mechanical Design

The HAM-SAS (fig. 4.1) [37, 38, 39] is a passive Seismic Attenuation System which is designed to provide 70-80 dB of horizontal and vertical attenuation above 10 Hz. Originally conceived for the isolation of the Output Mode Cleaner optics, it represents a low cost and less complex alternative to the HAM-ISI active system (see subsection 3.3.2.2) for the support of the HAM optical benches of the future Advanced LIGO interferometers. Without introducing any additional stage the mechanical structure could be scaled up and adapted to the requirement of BSC chambers.

The mechanical design is based on several years of R&D by the Caltech SAS group. The system is composed of

- A four leg Inverted Pendulum (IP) table for horizontal attenuation
- 4 Monolithic Geometric Anti-Spring (MGAS) filters dedicated to vertical attenuation held together by a rigid rectangular cage called Spring Box (called MGASF Box in figure 4.1).
- A set of 8 nm resolution LVDT position sensors and 8 voice-coil actuators to be used for active attenuation

In HAM-SAS the horizontal and vertical degrees of freedom are mechanically separated and orthogonal. A rectangular symmetry instead of the commonly used (Virgo, TAMA experiments) triangular symmetry is used in order to adapt the system to the HAM vacuum chamber geometry and to match the optical table symmetry and dimension.

4.1.1 Horizontal Stage

4.1.1.1 Basic Theory of Inverted Pendulum

The Inverted Pendulum (IP) is a tunable mechanical oscillator widely used for its good horizontal seismic attenuation performance. It is typically implemented

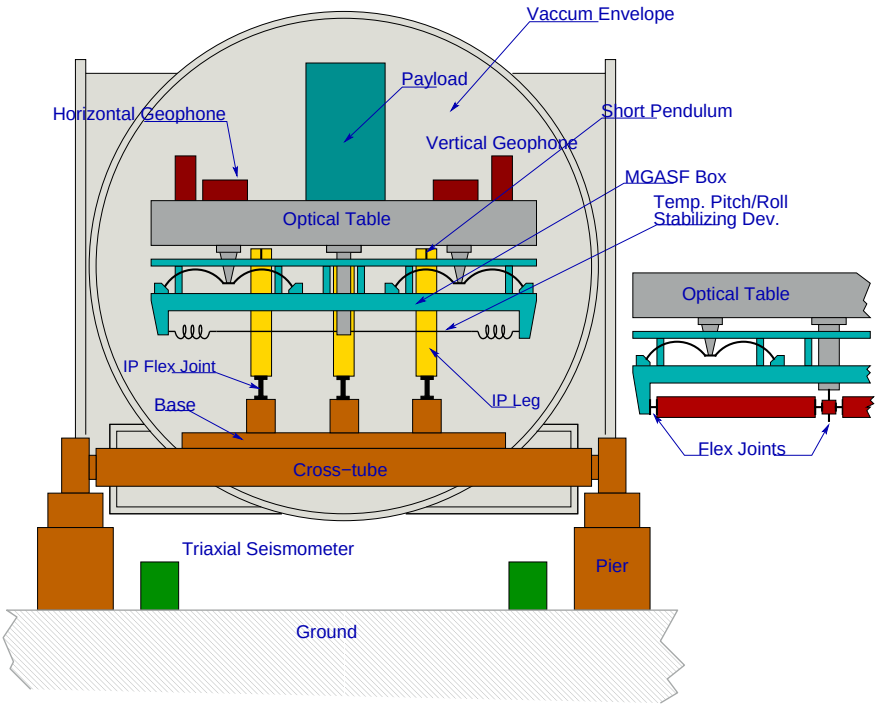

Figure 4.1: Sketch of HAM-SAS mechanical system, and the improved pitch/roll stabilizing device of the optical table. Black bold lines indicate elastic structures, same color filled parts indicate rigid structures.

using aluminum legs and maraging steel flexible joints. Resonant frequencies of tens of mHz have been routinely reached in many systems (Virgo, TAMA) simply increasing the payload. One of the main advantages of the IP is its very easy controllability. The force needed to statically move the load M of an amount x, at frequencies $f \ll f_0$ is simply $F \sim M\omega_0^2 x$. This means we can move the IP of a considerable amount introducing only limited noise in the interferometer detection band.

A simple unidimensional model is shown in fig. 4.2. It is constituted by a load of mass M supported by a rigid rod of length L, mass m and moment of inertia I connected to ground through a flexible joint with angular stiffness κ. Neglecting the viscous damping, the Lagrangian of the system can be written as

$$\mathfrak{L} = T_{Load} + T_{Leg} - U_{Load} - U_{Leg} - U_{FJ} \tag{4.1}$$

with

$$T_{Load} = \frac{1}{2}M\dot{x}^2 \tag{4.2}$$

$$T_{Leg} = \frac{1}{2}m\dot{x}_c^2 + \frac{1}{2}I\dot{\theta}^2 \tag{4.3}$$

$$U_{Load} = Mgz \tag{4.4}$$

$$U_{Leg} = mgz_c \tag{4.5}$$

$$U_{FJ} = \frac{1}{2}\kappa\theta^2 \tag{4.6}$$

Considering the system in the small oscillations condition and assuming the leg uniform we can rewrite the Lagrangian as

$$\mathfrak{L} = \frac{1}{2}M\dot{x}^2 + \frac{1}{8}m(\dot{x}+\dot{x}_0)^2 + \frac{1}{2}\frac{I}{L^2}(\dot{x}-\dot{x}_0)^2 + \frac{1}{2}\frac{g}{L}\left(M+\frac{m}{2}\right)(x-x_0)^2 - \frac{1}{2}k(x-x_0)^2 \tag{4.7}$$

where $k = \kappa/L^2$. Calculating the Euler-Lagrange equation and making the Fourier transform, we obtain the IP transfer function

$$\frac{X(\omega)}{X_0(\omega)} = \frac{\omega_0^2 + \beta\omega^2}{\omega_0^2 - \omega^2} \tag{4.8}$$

where the resonance frequency ω_0 is

$$\omega_0 = \frac{k - (M + m/2)g/L}{M + m/4 + I/L^2} \tag{4.9}$$

and

$$\beta = \frac{m/4 - I/L^2}{M + m/4 + I/L^2} \tag{4.10}$$

Comparing the expression 4.9 with the resonance frequency of a simple spring, we see that gravity acts as an antispring with an approximate stiffness $M\frac{g}{l}$. Even if theoretically we could obtain an arbitrary low ω_0 by changing the load and the joint stiffness, in order to avoid instabilities in the system, we have to choose a conservative value of the resonance frequency ($f_0 > 10$ mHz).

Plotting the transfer function, see fig. 4.2, we notice the critical effect of the factor β on the attenuation. For $\beta \neq 0$ the curve saturates as in the case of a massive spring. This is caused by the center of percussion effect (COP): at high frequencies the IP leg actually rotates around a point, called center of percussion, that does not coincide with the hinge point of the flex joint. The solution to this problem is to place a counterweight on the bottom of leg to change its moment of inertia, trying to obtain the smallest possible value of β.

4.1.1.2 HAM-SAS IP

As shown in the left picture of fig. 4.3, the IP leg used in HAM-SAS (A) is a 5 cm diameter, 50 cm length, tube made of aluminum. It connects to ground through a stiff cylindrical flex joint (B) made of maraging steel. Rigidly connected to the bottom end of the leg is a light aluminum bell, which carries a circular counterweight mass (C) at its bottom rim. As we have seen in previous paragraph, the counterweight is essential in obtaining the desired level of horizontal attenuation. The top of the leg is sliced on a diameter for a width of 2

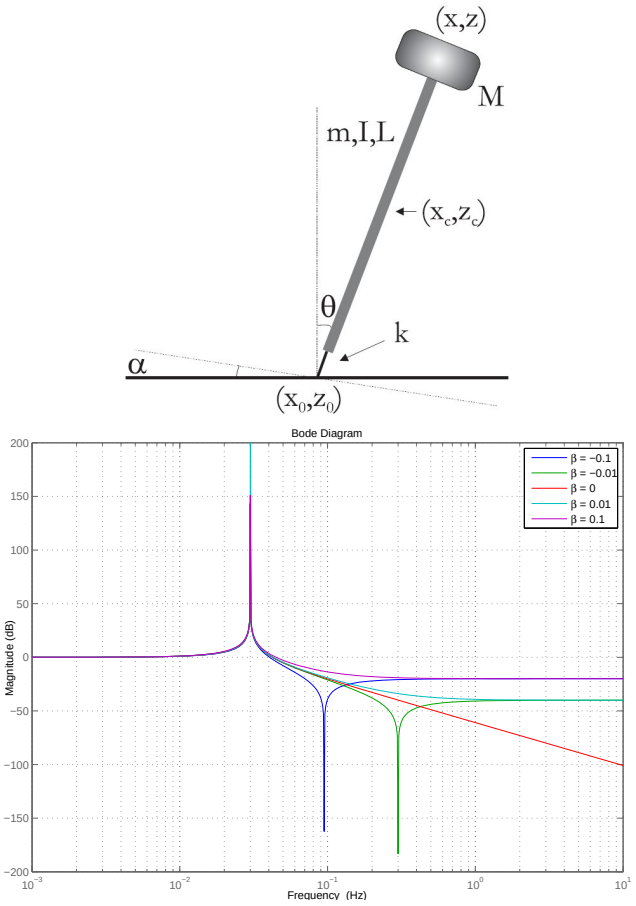

Figure 4.2: A simple model of an IP: sketch (top), transfer function for $f_0 = 30$ mHz and several values of β (bottom).

cm to allow the passage of the bridge (D) bolted to the spring box top plate. A 2.5 cm length thin wire flexture (F), called Little Pendulum, extends from the cap (E) to the bridge providing a flexible connection to the spring box plate. As we will see in the next chapter it essentially behaves as a spherical joint.

4.1.1.3 Tilt stabilizing device

In order to increase the angular stiffness of the optical table, a temporary pitch/roll stabilizing device (see fig. 4.1) has been introduced. Such a device comprises a vertical shaft, four helicoidal springs, and four wires. The shaft is connected to one end to the plate supporting the optical table. The other end holds the helicoidal springs each one attached to the spring box corners through a wire. Four screws, each one placed between a wire and a corner, allow the fine tuning of pitch and roll DOFs.

The tilt stabilizing device can be improved implementing two alternative solutions. One simple solution is to damp the modes introduced by the stabilizing device using dissipative mechanical dampers. Measurements have shown that,

using a simple elastic-polymer damper, the resonances quality factor are reduced by a factor 100. An alternative solution is the redesign of the device as shown in the right side of figure 4.1 where the resonances are eliminated by replacing springs and wires with flex joints and rigid hollow structures analogous to those used in the IP legs.

4.1.2 Vertical Stage

It is more difficult to generate clean, low noise and compact mechanical oscillators with low resonant frequency in the vertical direction [40]. Helical springs tend to rotate while extending or contracting and are excessively long if low-frequency isolation is required. To avoid this problem almost every GW experiment uses cantilever blade springs of some kind and, when helical springs are used, counter-wound springs cancel the extensional-torsional coupling.

Compact springs even cantilever blades tend to be stiff and oscillate at too high frequencies. Several techniques have been developed to soften them up and suitably reduce their resonant frequency. The precursors of this technique were the magnetic anti-springs in the Virgo super attenuator chains. The use of anti-springs in parallel to the cantilever blades to reduce the spring's vertical resonant frequency around their working point, naturally introduced nonlinearity in the spring's behavior. While anti-spring equipped springs behave like normal lower frequency harmonic springs for small oscillations, their oscillations progressively deviate from purely sinusoidal for larger excursions and their resonant frequency changes if significant changes of load or temperature shift the spring equilibrium point.

4.1.2.1 Monolithic Geometric Anti-Spring

The MGAS (fig. 4.3) is a vertical oscillator which uses a crown of radially compressed curved blades to provide the mechanical compliance [41]. The blades are clamped on one end to a plate, and connected on the other end to a small disk. The load connected to the disk compresses and bends the blades. Each MGAS filter houses 8 blades, and depending on their thickness, each blade they can carry up to 38 kg. The blades stress is kept down to 40% - 60% of the yield point. Acting on the position of the clamps one can change the blades' compression, and tune the MGAS resonant frequency down to 100 mHz.

At frequencies lower than a critical value the GAS filter's vertical transmissibility from ground to the payload has the typical shape of a simple second order filter (fig. 4.4) transfer function. Due to the distributed mass of the blades, the transfer function saturates at high frequency, limiting the attenuation at -60dB.

4.1.2.2 MGAS Magic Wands

As we have seen in paragraph 3.3.1, a real massive spring can provide $1/\omega^2$ attenuation only in a frequency range $\omega_0 < \omega < \omega_c$. Above that cutoff, the transfer function saturates at a level $\beta = m/M$. Rewriting eq. 3.6 for an undamped massive spring, we have

$$H_z = \frac{\omega_0^2(1+i\phi)+\beta\omega^2}{\omega_0^2(1+i\phi)+\omega^2} \tag{4.11}$$

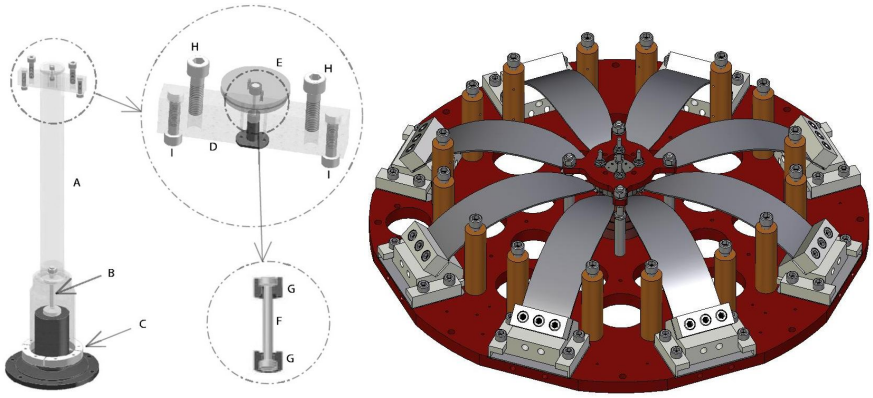

Figure 4.3: HAM-SAS IP (left) and MGAS (right) 3D CAD renderings

Since β is related to the mass distribution of the blades, we can use the center of percussion effect, in analogy of what what is done (see paragraph 4.1.1.1) for the inverted pendulum, to extend the attenuation range.

For this reason, a device equivalent to the IP counterweight (fig. 4.5), called "magic wand" has been developed [42]. It can be used to tune the effective MGAS COP, further improving the vertical filter attenuation for frequencies above a few Hz. The magic wand goes in parallel to the MGAS. It is constituted by a thin-wall carbon fiber tube hinged to the filter frame ring and the central keystone. A counterweight is attached to one in end in order to move the wand's COP out of the pivot.

A rigid body model of the system is shown in fig. 4.5. We will use this model in the next chapter. The MGAS is represented by a vertical undamped spring with linear stiffness k. The wand's tip and of the counterweight distances from the pivot point are the two arms lever L and l respectively. The wand is modeled as a massless hollow cylinder of length $L + l$, while the counterweight is considered a pointlike mass μ. We can now write the Lagrangian $\mathfrak{L}_{MW}$ of the system:

$$\mathfrak{L}_{MW} = T_{Load} + T_{MGAS} + T_{CW} - U_{CW} - U_{MGAS} \tag{4.12}$$

with

$$T_{Load} = \frac{1}{2} M \dot{z}^2 \tag{4.13}$$

$$T_{MGAS} = \frac{1}{2} m_{eff} \left(\frac{l_{eff}}{L} \right)^2 \dot{z}^2 + \frac{I_{eff}}{2L^2} (\dot{z} - \dot{z}_0)^2 \tag{4.14}$$

$$T_{CW} = \frac{1}{2} \mu \left(\frac{l}{L} \right)^2 \dot{z}^2 \tag{4.15}$$

and

$$U_{CW} = \frac{1}{2} g \mu l \left(\frac{z}{L} \right)^2 \tag{4.16}$$

$$U_{MGAS} = \frac{1}{2} k (z - z_0)^2$$

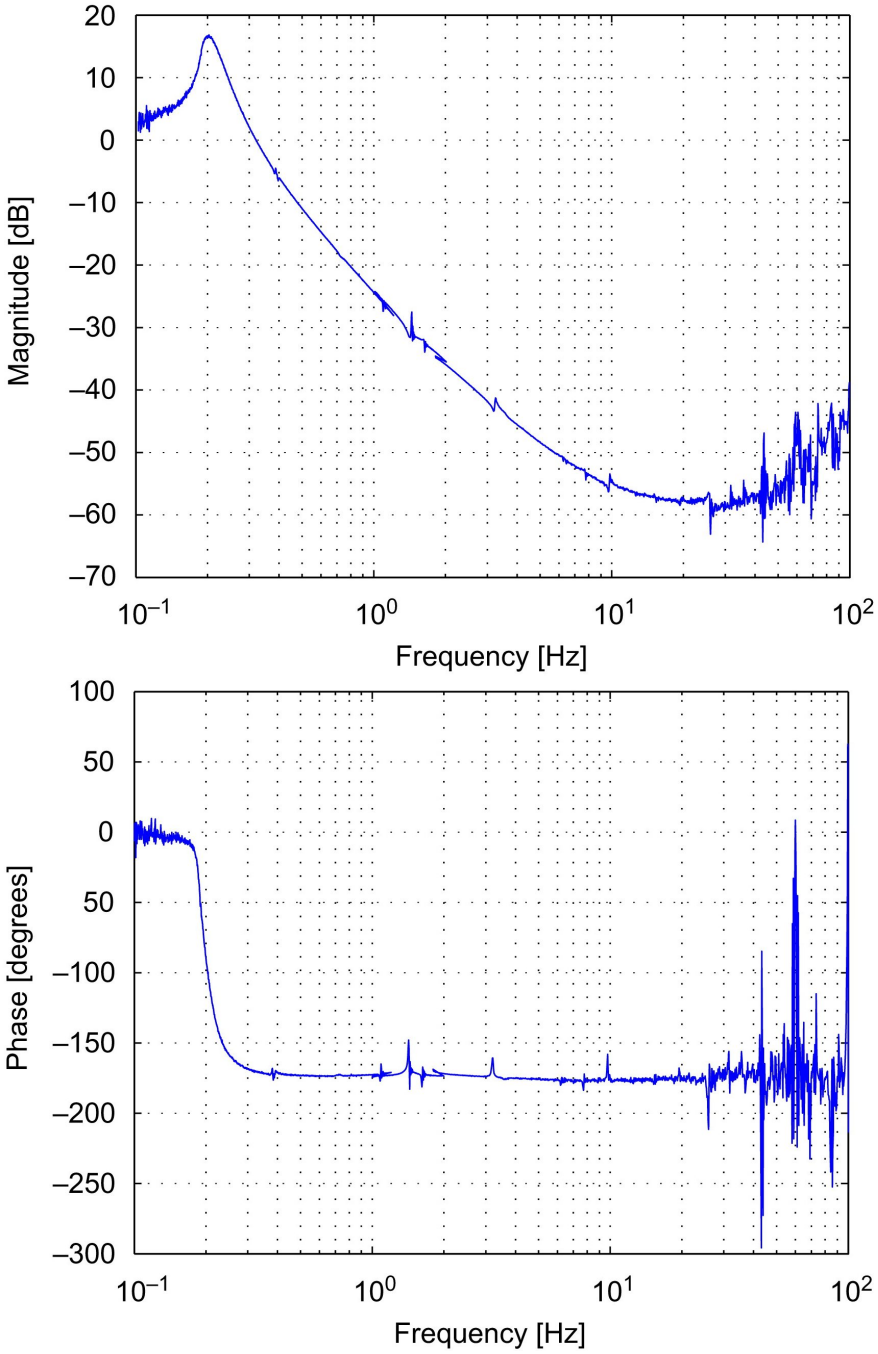

Figure 4.4: MGAS experimental transfer function magnitude (top) and phase (bottom). The high frequency plateau make the attenuation saturate at -60dB. It is more likely that the acoustic noise is dominant above 50 Hz where the accelerometers work as microphones.

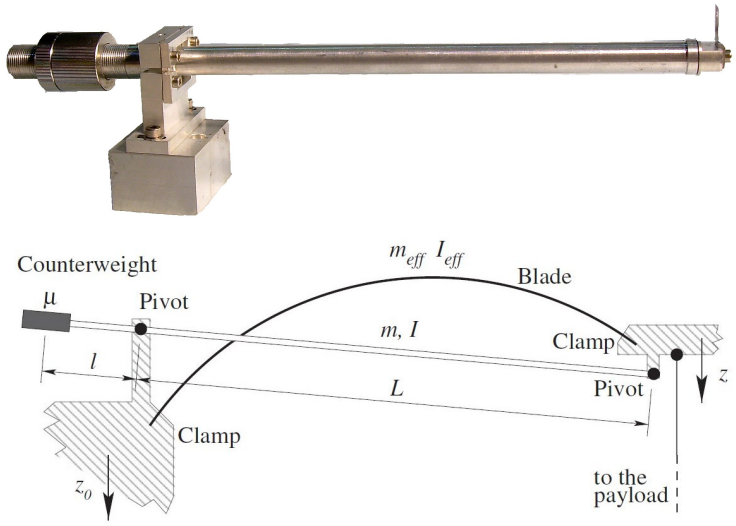

Figure 4.5: Top: Photo of one of the four magic wands that can be installed on each MGAS filter to improve its attenuation performance. Bottom: sketch of a simple rigid body mechanical model used in the text.

Obtaining the resulting equations of motion and calculating their Fourier transform, we can write the position transfer function in the form:

$$H = \frac{Z(\omega)}{Z_0(\omega)} = \frac{\omega_0^2 - A\omega}{\omega_0^2 - B\omega} \tag{4.17}$$

where $\omega_0^2 = k/(M + \mu l^2/L^2)$ and A and B are two constants. Theoretically choosing an appropriate value for the wand moment of inertia μl^2, in order to have $A = 0$, we could restore the infinite $1/\omega^2$ unlimited attenuation of a simple spring. In practice it's impossible to obtain the ideal value of μl^2 and a complex conjugate zero appears in the transfer function, in a similar way to what we have seen for the IP when $\beta \neq 0$.

4.1.3 Sensors and Actuators

4.1.3.1 LVDTs

HAM-SAS contains two sets of four LVDTs [43] for the controls and an additional set for monitoring. Each of the control LVDTs is co-located with a coaxial voice-coil actuator (fig. 4.6). Four vertical LVDTs, coaxially located inside the GAS filters, measure the vertical positions of four points of the optics table with respect to the spring box. Four horizontal LVDTs, located in correspondence of the inverted pendulum leg, measure the horizontal displacement of the spring box. The last four are witness LVDTs mounted underneath the top plate supporting the optics table and measure directly the displacement of the table respect to the base, three horizontal and one vertical.

A VME LVDT driver board have been used in HAM-SAS control. The LVDT board specifications are:

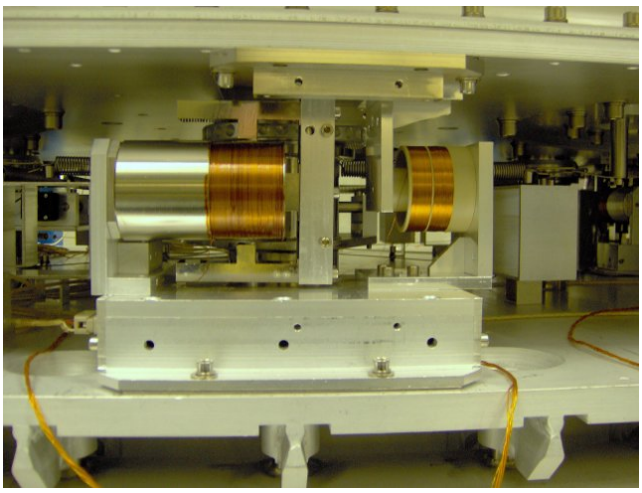

Figure 4.6: Photo of an horizontal LVDT and its associated electromagnetic actuator used in HAM-SAS

- 8 independent channels, first channel set as master in master-slave trigger configurations.
- One single-ended output per channel for signal monitoring
- One single-ended input, for external oscillator operation
- One single-ended output, for board synchronization
- Master-slave/asynchronous operation selectable through onboard jumpers.
- External/internal oscillator operation selectable through onboard jumpers.
- $\pm$ 22 Vpp primary output voltage
- $\pm$15 V - $\pm$18 V Supply operating voltage.
- 3 24-pin connectors for LVDT primary winding excitations, LVDT secondary winding readbacks, ADC

The circuit, shown in figure 4.7, is based on the Analog Devices Universal LVDT Signal Conditioner AD698 chip [44]. The component feature are

- Tunable Internal oscillator from 20 Hz to 20 kHz
- Double channel demodulator: two synchronous demodulator channels are used to detect primary and secondary amplitude. The component divides the output of the secondary by the amplitude of the primary and multiplies by a scale factor in order to improve temperature performance and stability. In this way a typical offset drift of 5 ppm/^{0}C and a typical gain drift of 20 ppm/^{0}C are reached.
- Tunable low pass filter for each demodulator
- Amplifying stage at the output

A phase compensation network is used to add a phase lead or lag to one of the modulator channels in order to compensate for the LVDT primary to secondary phase shift. A low noise instrumentation amplifier, INA217, is used for LVDT secondary readbacks differential input. Specifically designed for audio signal amplification, this component has a voltage noise of 1.4 nV/$\sqrt{\text{Hz}}$ at 1 kHz and a THD of 0.004% at 1kHz for a 100 gain factor. The gain can be adjusted through an external potentiometer. A wide-band fully differential amplifier, THS4131, is used for primary winding excitation output.

Several measurements have been done in order characterize the performance of the three versions of the board [45]. An experimental setup, composed by a 50 μm resolution Line Tool micropositioner fixed on an optical table and rigidly connected to the LVDT primary winding, has been used. Several custom made Horizontal LVDT prototypes have been realized in order to determine the optimal ratio between the radii of primary and secondary windings. LVDT spectral density noise measurements (figure 4.8) have been done after centering the LVDT primary coil to get zero signal output. Several independent measurements have been performed to cover different frequency ranges. Calibration measurements have shown a low level of nonlinearity (less than 1% of the range). Residual displacement noise of 2 nm/$\sqrt{\text{Hz}}$ @ 10 Hz has been measured for both LVDTs. Crosstalks of 1% between the horizontal and longitudinal and between horizontal and vertical degrees of freedom have been obtained. The results obtained in an optimized configuration are summarized in the following table:

	Horizontal LVDT	Vertical LVDT
Nonlinearity	0.88%	0.26%
Sensitivity	6.49 V/mm	7.85 V/mm
Range	20 mm	20 mm
Displacement Noise	2 nm/$\sqrt{\text{Hz}}$ @ 10 Hz	2 nm/$\sqrt{\text{Hz}}$ @ 10 Hz

4.1.3.2 Electromagnetic Actuators

In the Virgo seismic isolation system, a contact-free actuator was achieved using two large coils in a Helmholtz pair configuration, and a small permanent dipole magnet in the central volume of constant field gradient. In the Helmholtz pair, the two coils are positioned so that the increasing field gradient of one coil is canceled by a corresponding decrease in the other coil. Sufficient gradient uniformity is obtained in a volume typically 5% of the coil dimension. The main disadvantage of this configuration is that, in order to obtain a reasonable movement range, large coils are required along with a corresponding large dissipation of power in vacuum. To alleviate this problem a relatively large permanent magnet dipole is used. However a disadvantage of this scheme is that the absence of a magnetic field returns yoke allows formation of large dimension open magnetic fields, which can either perturb or be perturbed by external fields. Additionally, relatively large currents (and power dissipation) are necessary to produce the required forces.

For this reason, the SAS group designed and implemented a contact-free actuator [46] made of a racetrack coil mounted on the IP table, floating in the confined magnetic field of a twin-gap magnetic yoke. The yoke is attached to the external reference structure and energized by two permanent magnets. A current passing through the coil will generate a force proportional to the integral

of the yoke's magnetic field combined with the distributed current in the coil. This arrangement does not generally produce a force that is independent of the relative position of the coil and the yoke. A careful design of both the coil and yoke solved this problem.

4.2 HAM-SAS Prototype testing

The installation and commissioning of HAM-SAS was done at the LASTI (LIGO Advanced System Test Interferometer) facility during a short period of less than four months. The LASTI is made up of standard full-scale LIGO vacuum chambers, arrayed in an 'L' configuration with arms lengths of 15 m. Measurements to characterize the performance of HAM-SAS mechanical system were done under vacuum to eliminate acoustic noise, air flow perturbations, and to reduce thermal drifts.

4.2.1 Experimental Setup

The tests performed at LASTI tried to simulate the AdLIGO conditions. As shown in fig. 4.9, the triple pendulum suspension was installed on the optical table and several weights were arranged to simulate the same mass distribution and height of the optics that will be installed.

4.2.1.1 Geophones

Six unidirectional Mark L-4C geophones were placed on the optical table and suitably oriented to detect the residual excitation of all the six DOFs. As shown in fig. 4.9, three of them are aligned with the optical table plane in a pinwheel configuration while the remaining three are orthogonal, disposed in a triangular configuration.

Geophone are simple passive electro-mechanical sensors. Mark L4C model contains a permanent magnet and a moving coil attached to a 1 kg proof mass suspended on soft springs with resonant frequency around 1 Hz. For frequencies greater than the mechanical resonance, the geophone produces an output voltage proportional to the relative velocity of the mass, $\dot{x}-\dot{x}_g$, measured with respect to the permanent magnet which is fixed in the housing of the transducer. For lower frequencies, voltage falls as proof mass motion starts to follow ground motion. In a more subtle way, because of the Principle of Equivalence, at low frequency, geophones are affected by tilt- to-horizontal coupling, which prevents them from distinguishing the accelerations along x and y from the angular ones along θ_x and θ_y. For this reasons an high pass filter that removes the components below 100 mHz from the output signal has been used. Moreover, in order to pass from velocity to position, a simple calibration filter constituted by a single pole at low frequency, has to be applied to the signal.

4.2.1.2 Seismometers

Three tri-axial force-feedback Guralp CMG-40T seismometers, placed around the HAM chamber in an L configuration, measured the six-DOF excitation of the ground. As in the case of geophones, Guralp CMG-40T generates an output signal proportional to the ground velocity in a frequency band that is declared

by the manufacturer to be between 0.033 Hz and 50 Hz. The seismometer uses two independent sensors for horizontal and vertical DOFs that can be considered orthogonal with an accuracy of 0.2 degrees. The horizontal sensor is constituted by an inverted pendulum supported by two parallel leaf springs while the vertical one consists in a mass, connected to an horizontal blade spring. The total weight of each sensor is approximately 35 g.

4.2.1.3 Optical Lever

The optical lever monitors the triple pendulum providing an auxiliary measurement of the optical table motion along θ_z and θ_y. A diode laser, positioned on top of a pier just outside the HAM chamber, emits a beam that enters the chamber through a glass porthole and hits the mirror in the middle of the bottom mass of the triple pendulum. The reflected beam reaches the center of a QPD (Quadruple Photo-Detector) sensor placed right next of the laser source. A QPD is made of a four quadrant photodiode in which each quadrant gives a voltage proportional to the impinging power. The signal share between the four channels depends on the position hit by the beam spot. The linearity range and sensitivity of this detector depend on the laser spot size.

4.2.2 Measurements

Figure 4.10 shows the measured transmissibility along the Cartesian coordinates x, y, z from ground to the optical table. The plot is obtained calculating the transfer function between the signals of the geophones placed on the optical table and the ambient anthropogenic noise measured by the Guralps. The first resonance at approximately 65 mHz, present in x and y plots, corresponds to the IP flexible joints resonant frequency. The resonance at approximately 100 mHz in z plot is due to the MGAS resonance frequency. The second peak in x and y at 125 mHz indicates a crosscoupling between the horizontal and vertical DOFs that is due to the fact that the Spring Box platform is probably tilted respect to ground. The third resonance in x and y at 265 mHz is caused by a horizontal resonant frequency of the MGAS springs. This resonance is due to the fact that the optical bench is connected to the MGAS filters by four vertical small piers. Those piers couple to the angular compliance of the MGAS filters, allowing horizontal motion. Below about 50 mHz the measurement showed almost zero coherence due to the poor sensitivity of the seismometers. Peaks between 15 Hz and 30 Hz are due to internal resonances attributed to the tilt stabilizing device.

The seismic attenuation performance measured with all the active controls on is shown in fig. 4.11 for x and z DOFs. The red curves shows the seismic noise measured by the Guralps, while the blue ones are the optical table motion obtained from the geophone signals. We see that the measurements meets the AdLIGO HAM requirements in most of the frequency range with the exception of a few regions. Along z for $f \simeq 200$ mHz and along x for $f \lesssim 100$ mHz, the noise introduced by the suspension exceeds the seismic motion. This is caused in the first case by the MGAS filters resonance frequency while in the second one is probably due to imperfect controls designed over a not fine enough diagonalization of the physical plant matrix. The marked peak at around 20 Hz is a spurious resonance and appeared after the installation of the tilt sta-

bilizing springs. Two possible solutions to this problem have been described in subsection 4.1.1.3.

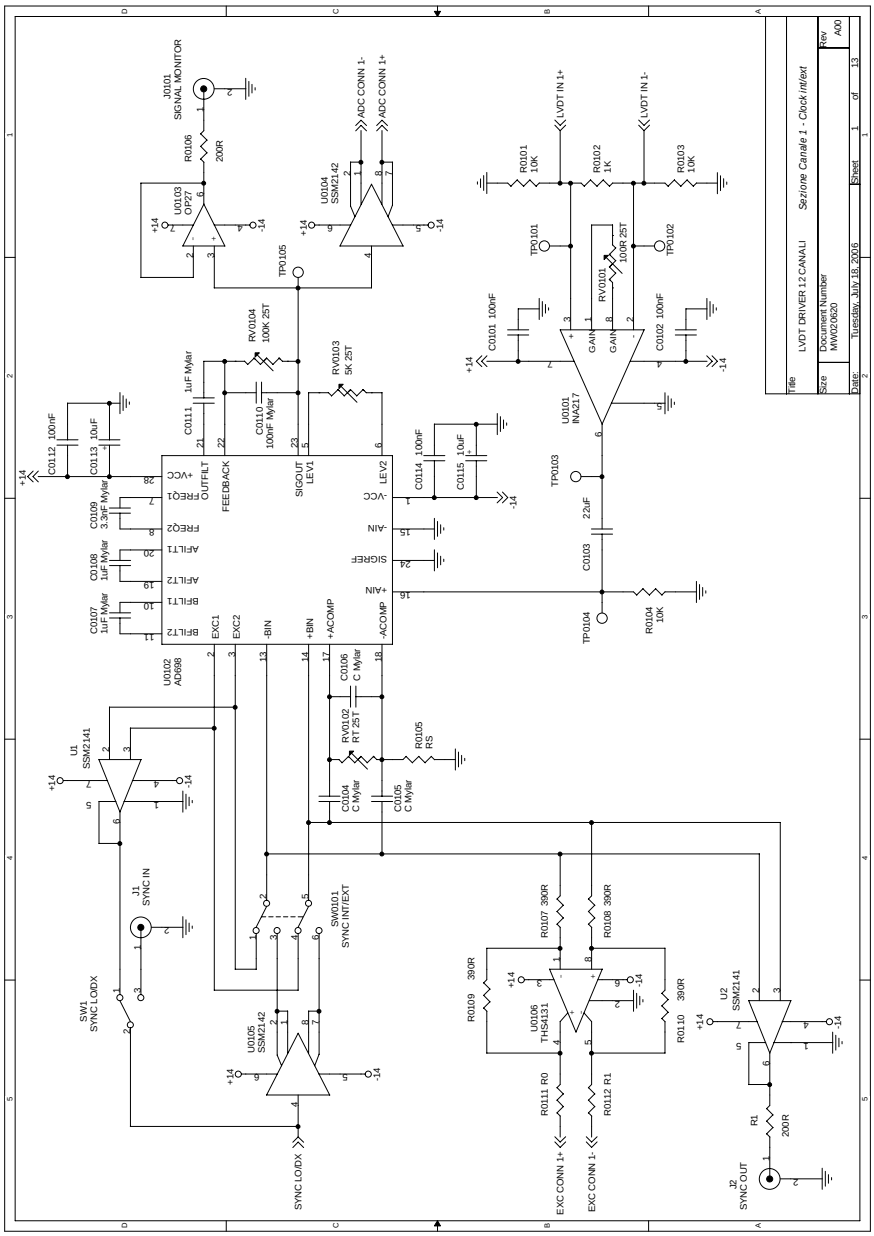

Figure 4.7: Schematics of LVDT Board master channel

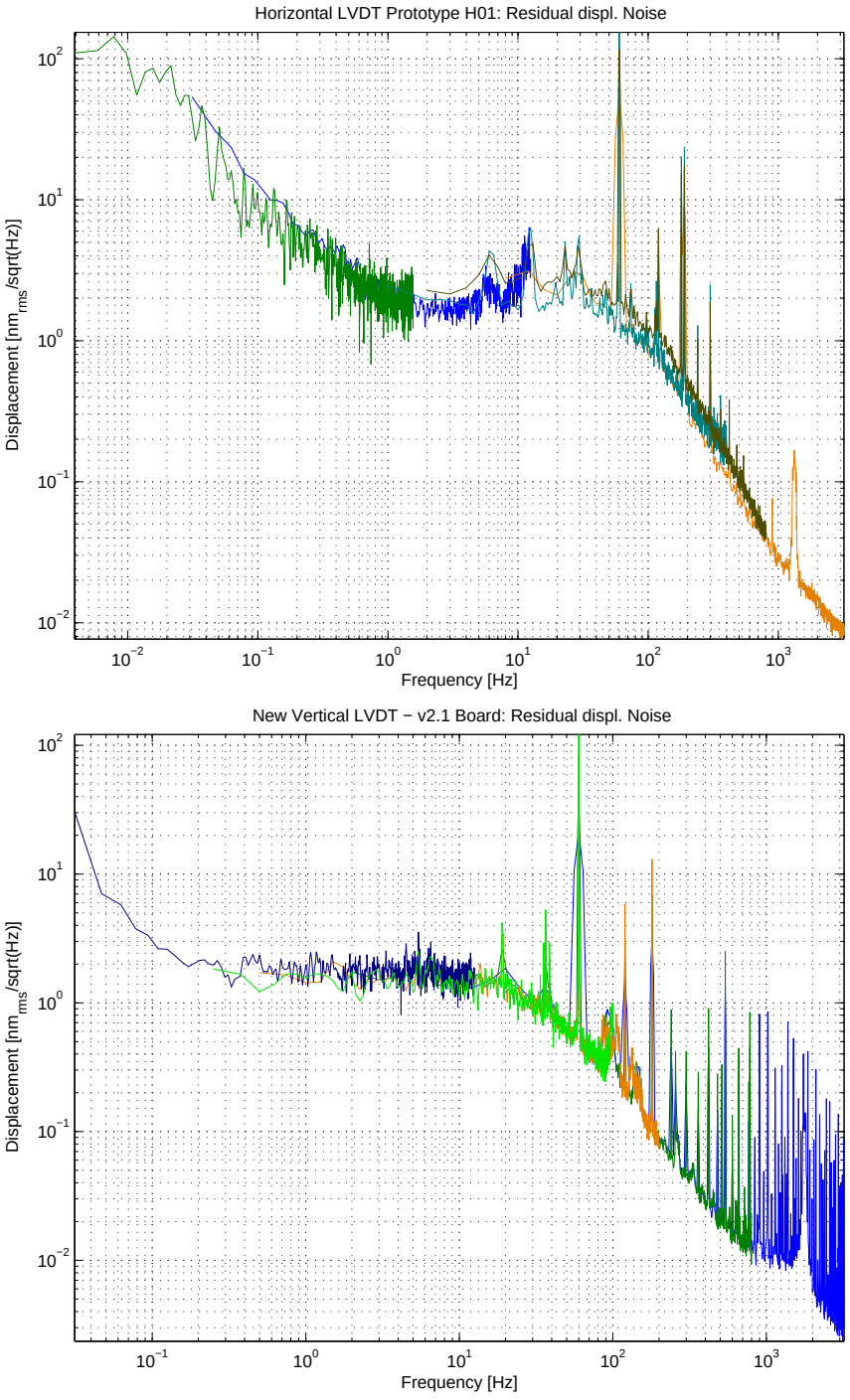

Figure 4.8: Square root power spectral densities of horizontal and vertical LVDT displacement noise.

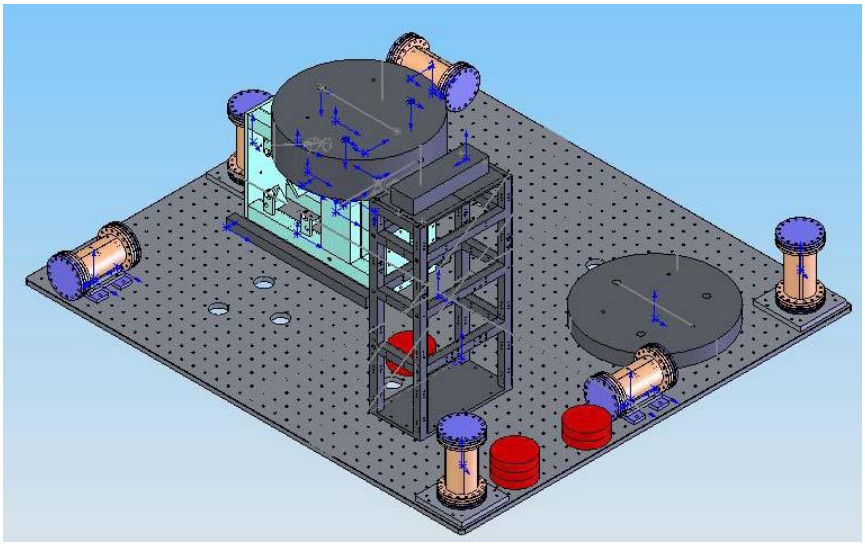

Figure 4.9: Optics table installed on HAM-SAS for measurements and testing inside the LASTI HAM vacuum chamber.

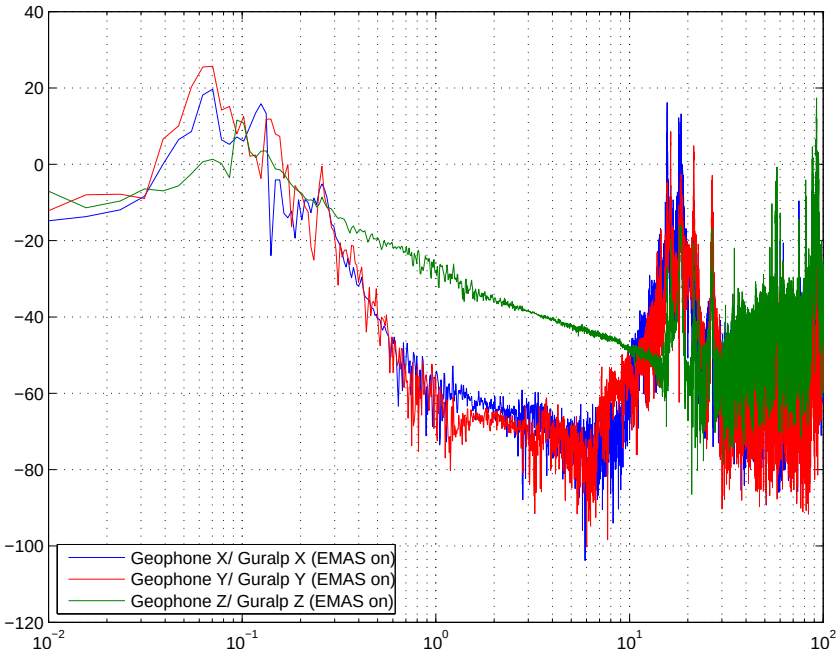

Figure 4.10: Experimental transmissibilities along x (blue), y (red) and z (green) obtained calculating for each DOFs the transfer function between the Geophones signals and the ground motion measured by the Guralps.

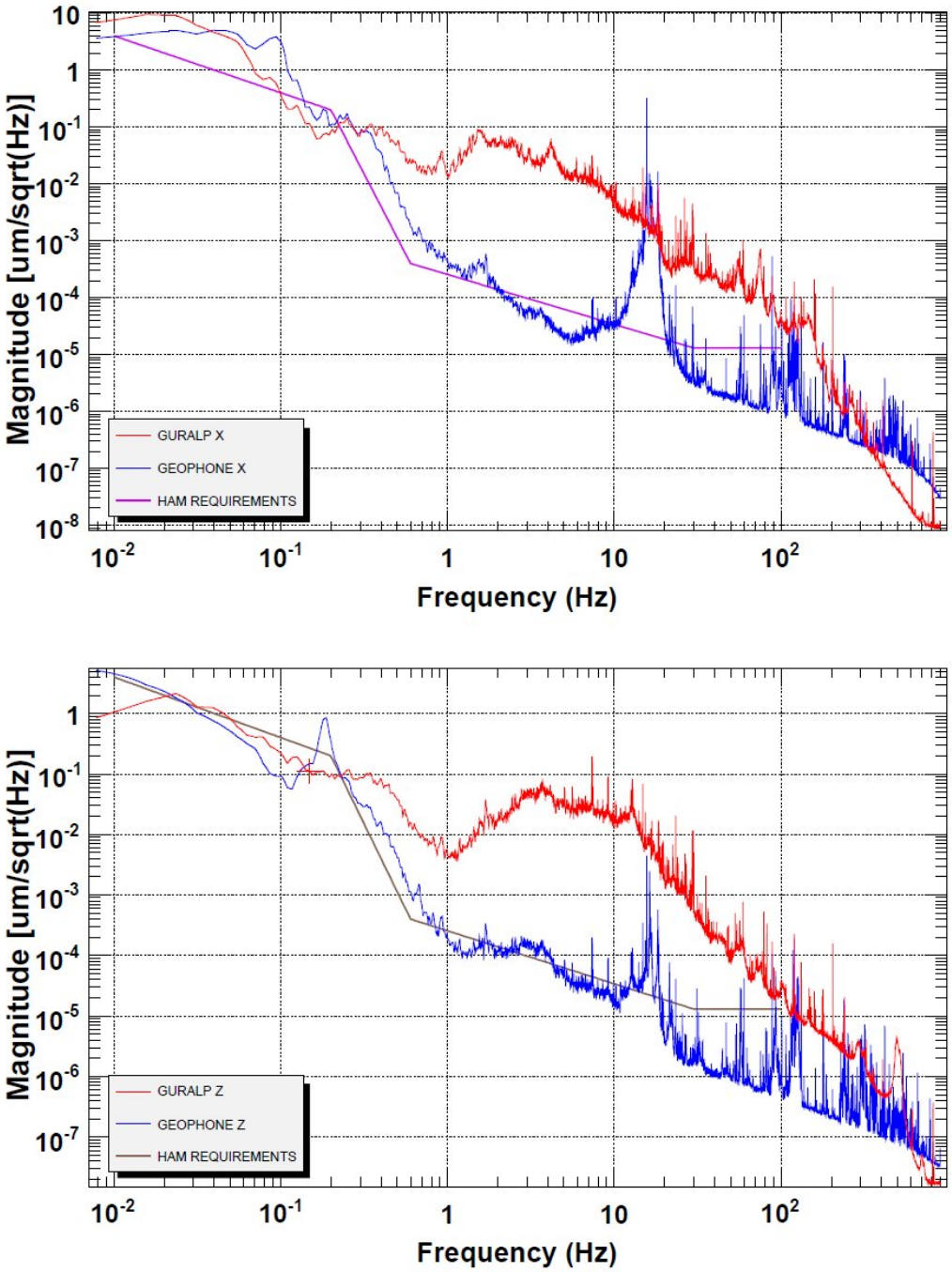

Figure 4.11: HAM-SAS prototype measured performance along x and z DOFs. All controls are active. Red curves are the power spectra of ground motion measured by the Guralps, Blue curves represent the displacement spectra of the Optical Table obtained from the Geophone signals. Gray and Magenta curves are the HAM AdLIGO requirements.

Chapter 5

HAM-SAS Analytical Multibody Modeling

During HAM-SAS designing phase, in order to evaluate its performance and allow the design of the control system, we developed two sets of multibody, three-dimensional, multiple-degrees of freedom models. The set described in this chapter is constituted by linear analytical models written in Maple symbolic language, while the one detailed in chapters 6 and 7, consists of non-linear numerical models developed with MultiBody Dynamics (MBDyn) simulation software. In both model sets the angular wires' stiffness is neglected and the dissipation mechanisms are accounted using viscous damping to approximate structural/hysteretic damping.

5.1 Modeling of mechanical systems

Models of vibrating systems can essentially divided in two broad classes [47], lumped or continuous, depending on the nature of their parameters. In the case of lumped-parameter systems, the components are discrete with the mass assumed to be rigid and concentrated at individual points and with the stiffness in the form of massless springs. This approach is commonly called multibody dynamics modeling. The motion of this systems is described by ordinary differential equations, one for each mass, and the number of masses defines the number of degrees of freedom of the system. Since for each independent variable we have an initial condition, this kind of problems are known as Initial Value Problems.

When the elastic components cannot be regarded as equivalent springs, because their mass is no longer negligible, the system has to be described with a continuous-parameter model. In this case the mass and stiffness parameters are in general function of the spatial variable x, and referred to as distributions, with the mass being given in the form of mass linear density. The displacements are now dependent by x and by the time t. As a result the motion of distributed-parameter systems is governed by partial differential equations to be satisfied over the domain of the system. This means that the equations are subject to boundary conditions at the end points of the domain, and we have to solve a Boundary Value Problem.

Since, for the most part, this kind of problems doesn't admit exact solution, several approximate methods have been developed. The Finite-Element Method (FEM) is the most common technique used to simulate complex continuous-parameter systems. This method tries to find an approximate solution of the equation of motion in the form of linear combinations of known trial functions multiplied by undetermined coefficients. The trial functions extend over small subdomains of the system, called finite elements, and are usually constituted by low degree polynomials.

Although the most common way to simulate a complex mechanical system is by means of FEM techniques, this approach for HAM-SAS was not entirely successful. Even though FEM simulations have been useful to study the internal modes of the rigid structure [48, 49], they were unable to accurately reproduce its dynamic behavior, especially at low frequency. For this reason, a multibody approach was preferred.

5.2 Model description

Let's list first the most important approximations used in the model:

- Lumped-parameter system,
- elastic elements approximated using quadratic potentials, i.e. small oscillation regime,
- dissipation mechanisms accounted using viscous damping to approximate structural/hysteretic damping,
- system assumed to be symmetric enough to separate horizontal displacements x, y, and yaw θ_z from pitch θ_y roll θ_x and vertical displacement z,
- internal modes of the mechanical structures not accounted,
- angular wires' stiffness neglected,

Using lumped elements limits the accuracy of the simulation to frequency lower than the lowest internal frequency. HAM-SAS is expected to have internal modes frequencies starting at around 100 Hz.

The reason of using viscous instead of hysteretic damping is because of the need of having a straightforward state-space representation for time domain simulations studies. In the small oscillation regime, the major difference between the two kind of damping is that the viscous damping changes the resonant frequencies of the modes. Practically, this turns out to be just a minor drawback because resonances are tuned to some nominal frequencies.

A symmetric system such as HAM-SAS has some orthogonal degrees of freedom that simplify the implementation of the dynamic model. Asymmetries are expected to introduce coupling no more than 1% among degrees of freedom. Therefore, for seismic attenuation performance estimation purposes such approximation should be reasonable.

Neglecting angular wires' stiffness produces an underestimation of the pendular modes frequencies, which is negligible in our case vis-a-vis the wires' cross section and tensions.

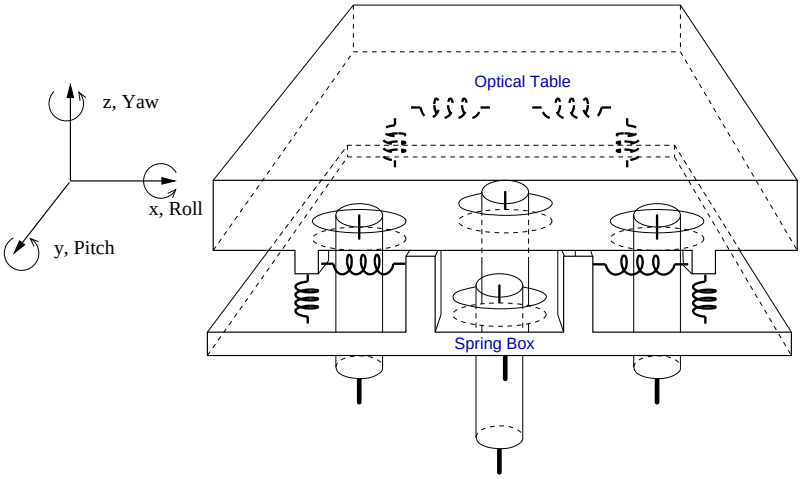

Figure 5.1: Simplified sketch of the analytical mechanical models developed (IP counterweight bells, MGAS wands and wands' counterweights not shown).

Figure 5.1 shows a sketch of this mechanical model with rigid bodies, linear springs, and flexural joints. Inverted pendulums counterweight bells and MGAS wands and wands' counterweights are not shown for sake of simplicity. More detailed sketches are shown in figures 5.2 and 5.4.

The physical parameters used in the model have been in part extracted from HAM-SAS official production drawings [50], in part evaluated to match experimental data acquired on several prototypes. Masses and moments of inertia have been calculated using SolidWorks CAD from the three-dimensional drawings of the system realized by Y.Huang.

In the model the entire mechanical system is sitting on a base which is used to excite the Attenuator in all the 6 degree of freedom. Internal resonances of the IP legs and other supporting structures are not included in the simulation.

The mechanical model has been implemented using scripts in Maple symbolic language. Those scripts produce a state-space representation of the system that can be easily imported into Matlab and Simulink for control simulations. The way that the code has been written is such that allows to progressively introduce new features to improve the accuracy and remove degrees of freedom to check the consistency of the simulation. For example, it is possible to freeze all the degrees of freedom but the one describing the IP and verify that the model gives the expected simple response similar to a compound pendulum. This feature allowed us to increase our confidence about the model.

5.2.1 Equations of motion

The equations of motion of an n-degree of freedom mechanical system with viscous damping subject to holonomic constraints can be written, in Lagrange's

formulation, as

$$\frac{d}{dt}\left(\frac{\partial T}{\partial \dot{q_k}}\right) - \frac{\partial T}{\partial q_k} + \frac{\partial U}{\partial q_k} + \frac{\partial \mathfrak{F}}{\partial \dot{q_k}} = Q_k \quad k = 1, 2, \dots n \tag{5.1}$$

where $T = T(q_1, \dots, q_n, \dot{q_1}, \dots, \dot{q_n})$ is the kinetic energy, $U = U(q_1, \dots, q_n)$ is the potential energy, $\mathfrak{F} = \mathfrak{F}(\dot{q_1}, \dots, \dot{q_n})$ is the Rayleigh's dissipation function, $q_k(t)$ are generalized coordinates and Q_k are generalized non conservative forces. The function $\mathfrak{F}$ is defined as

$$\mathfrak{F} = \frac{1}{2}\sum_{i=1}^{n} \gamma_i \dot{q_i} \tag{5.2}$$

and represents the physical work done by the system against the friction forces. In order to simplify 5.1, the variable, $\mathfrak{L} = T - U$, called Lagrangian function, is commonly used.

Even though the equations 5.1 are in general non-linear, we are interested in the small motions around the equilibrium points of the system, the so called small oscillation regime. In this condition we express the displacements in the form

$$q_k(t) = q_k^{eq}(t) + \tilde{q_k}(t) \quad k = 1, 2, \dots n \tag{5.3}$$

where q_k^{eq} are the displacements when the system is the equilibrium position and $\tilde{q_k}$ are small perturbations. Consequently the generalized velocities satisfy

$$\dot{q_k}(t) = \dot{\tilde{q_k}}(t) \quad k = 1, 2, \dots n \tag{5.4}$$

Introducing the conditions 5.3 and 5.4 in 5.1, it's easy to proof that, the equations of motion of a n-degree of freedom system become linear and can be written as

$$M\ddot{\mathbf{q}}(t) + \Gamma\dot{\mathbf{q}}(t) + K\mathbf{q}(t) = \mathbf{Q}(t) \tag{5.5}$$

where $\mathbf{q}(t) = (q_1(t), q_2(t), \dots, q_n(t))$, M is the mass matrix, Γ is the damping matrix, K is the stiffness matrix and $\mathbf{Q}(t)$ is a vector of generalized non conservative forces.

In order to easily use the models for control simulation, we need to convert them in the canonic state space representation. To this end we introduce the identity

$$\ddot{\mathbf{q}}(t) = -M^{-1}\Gamma\dot{\mathbf{q}} - M^{-1}K\mathbf{q} + M^{-1}\mathbf{Q}(t) \tag{5.6}$$

Introducing the $2n$-dimensional state vector $\mathbf{x}(t) = \left[\mathbf{q}^T(t), \dot{\mathbf{q}}^T(t)\right]$, we can write the 5.5 in the state-space representation

$$\dot{\mathbf{x}}(t) = A\mathbf{x}(t) + B\mathbf{Q}(t) \tag{5.7}$$

with

$$A = \begin{pmatrix} \mathbf{0}_{n\times n} & I_n \\ -M^{-1}K & -M^{-1}\Gamma \end{pmatrix} \tag{5.8}$$

and

$$B = \begin{pmatrix} \mathbf{0}_{n\times n} \\ M^{-1} \end{pmatrix} \tag{5.9}$$

where $\mathbf{0}_{n\times n}$ is an $n \times n$ matrix with all elements equals to zero and I_n is the $n \times n$ identity matrix. The vector $\mathbf{Q}(t)$ represents the input of the state-space model and is constituted by the set of forces used to excite the system. The second equation of the state space representation is by definition

$$\mathbf{Y}(t) = C\mathbf{x}(t) + D\mathbf{Q}(t)$$

In our case the matrices C and D are not univocally determined since they depend by the chosen outputs $\mathbf{Y}(t)$ and inputs $\mathbf{Q}(t)$.

5.2.2 MGAS Table Model

The MGAS table model is shown in figure 5.2. Their constituents are

- **7 Rigid Bodies**: 1 massive Base used to excite the system with respect to the ground in the vertical DOFs, 1 Optical Table (OT), 1 Spring Box (SB), 4 Vertical CounterWeights (VCW) connected to the "magic wands".
- **8 Linear Springs with viscous damping**: four of them constitute, together with the wands, the Vertical MGAS (HMGAS) filter. The other four springs are used to simulate the vertical stiffness of the little pendulums.
- **7 Force Actuators**: Three of them are used to excite the Base, acting on its center of mass, the other four shake the system acting on points corresponding to the actual positions of the electromagnetic actuators.

The MGAS filter is modeled with an equivalent system which is able to account for most of the blades' mechanical compliances, and for attenuation saturation effects. The equivalence is achieved by tuning the model with measurements. Three orthogonal springs with the proper elastic constant are connected together by one end to the payload (the optical table), and the other three ends are attached to the filter frame. Saturation effects due to the blade's distributed mass are simulated with a wand pivoting around a point rigidly connected to the filter frame. One wand's end is then attached to a counterweight and the other is free to rotate about the point connected to the payload. The tuning of the attenuation saturation is done by changing the counterweight and/or the wand's length and/or wand's central pivot point. As we have seen in last chapter, in the actual MGAS filter wands are introduced to neutralize the attenuation saturation effects, while in the model the wands are used both to generate, and eventually to neutralize the saturations. This phenomenological model with two wands plus counterweight system is used to simulate the horizontal and vertical saturations of MGAS transmissibility. In both IP Table and MGAS Table Model we kept the mass of the counterweights, M^i_{HCW}, M^i_{VCW}, and the length of the arm levers , L^i_{HCW}, L^i_{VCW}, fixed and we calculated the length of the other arm levers, l^i_{HCW}, l^i_{VCW}, in order to have, in each transmissibility, a

notch at frequencies $fxnotch^i_{MGAS}$ and $fznotch^i_{MGAS}$ respectively. So we have

$$l^i_{HCW} = -\frac{fx^i_{MGAS} L^i_{HCW} \sqrt{-M^i_{HCW}\left(\left(fx^i_{MGAS}\right)^2-\left(fxnotch^i_{MGAS}\right)^2\right)M_{OT}/4}}{M^i_{HCW}\left(\left(fx^i_{MGAS}\right)^2-\left(fxnotch^i_{MGAS}\right)^2\right)} \tag{5.10}$$

$$l^i_{VCW} = -\frac{fz^i_{MGAS} L^i_{VCW} \sqrt{-M^i_{HCW}\left(\left(fz^i_{MGAS}\right)^2-\left(fznotch^i_{MGAS}\right)^2\right)M_{OT}/4}}{M^i_{VCW}\left(\left(fz^i_{MGAS}\right)^2-\left(fznotch^i_{MGAS}\right)^2\right)} \tag{5.11}$$

where fx^i_{MGAS} and fz^i_{MGAS} are the horizontal and vertical resonance frequencies of i-th MGAS filter.

Figure 5.3 shows a comparison between a model result and measurements of the vertical transmissibility of a MGAS blade with a single counterweight and wand. The model has been tuned in order to match the resonance and the notch frequencies of the measurement. A significant systematic discrepancy at low frequency (below 0.2 Hz) of approximately a 5 dB is clearly visible. The large uncertainty of the accelerometers calibration at low frequency used to take the measurement can partially explain such difference. Discrepancies above 50Hz are mainly due to the internal resonances of the supporting frame, the shaker, and the blade support designed for filter tuning studies.

We can write the Lagrangian $\mathfrak{L}_{MGT}$ of the MGAS table as

$$\mathfrak{L}_{MGT} = T_{MGT} - U_{MGT} \tag{5.12}$$

with

$$T_{MGT} = T_{Base} + T_{SB} + T_{OT} + T_{VCW} \tag{5.13}$$

$$U_{MGT} = U_{LP} + U_{MGAS} + U_{VCW} \tag{5.14}$$

where, using

$$T_{Base} = \frac{1}{2}M_{Base}\dot{z}^2_{Base} + \frac{1}{2}Ixx_{Base}\dot{\theta x}^2_{Base} + \frac{1}{2}Iyy_{Base}\dot{\theta y}^2_{Base} \tag{5.15}$$

$$T_{SB} = \frac{1}{2}M_{SB}\dot{z_{SB}}^2 + \frac{1}{2}Ixx_{SB}\dot{\theta x}^2_{SB} + \frac{1}{2}Iyy_{SB}\dot{\theta y}^2_{SB} \tag{5.16}$$

$$T_{OT} = \frac{1}{2}M_{OT}\dot{z_{OT}}^2 + \frac{1}{2}Ixx_{OT}\dot{\theta x}^2_{OT} + \frac{1}{2}Iyy_{OT}\dot{\theta y}^2_{OT} \tag{5.17}$$

$$T_{VCW} = \frac{1}{2}\sum_{i=1}^{4} M^i_{VCW}\left(\frac{l^i_{VCW}}{L^i_{VCW}}\right)^2(\dot{\eta}^i)^2 \tag{5.18}$$

and

$$U_{LP} = \frac{1}{2}\sum_{i=1}^{4} kz^i_{LP}(\psi^i)^2 \tag{5.19}$$

$$U_{MGAS} = \frac{1}{2}\sum_{i=1}^{4} kz^i_{MGAS}(\eta^i)^2 \tag{5.20}$$

$$U_{VCW} = \frac{1}{2}g\sum_{i=1}^{4} M^i_{VCW} l^i_{VCW}\left(\frac{\eta^i}{L^i_{VCW}}\right)^2 \tag{5.21}$$

The vertical stiffness of the MGAS kz^i_{MGAS} is estimated in order to have a resonance frequency fz^i_{MGAS}. We obtain

$$kz^i_{MGAS} = \left(2\pi fz^i_{MGAS}\right)^2 \left(\frac{M_{OT}}{4} + M^i_{VCW}\left(\frac{l^i_{VCW}}{L^i_{VCW}}\right)^2\right) \tag{5.22}$$

The vertical stiffness kz^i_{LP} has been evaluated considering the little pendulum as an homogeneous cylindrical beam of maraging steel

$$kz^i_{LP} = \pi \frac{(r^i_{LP})^2}{l^i_{LP}} Y_{mar} \tag{5.23}$$

where r^i_{LP} is the radius of i-th little pendulum and Y_{mar} is the maraging Young's modulus.

The MGAS table dissipation function, $\mathfrak{F}_{MGT}$, is

$$\mathfrak{F}_{MGT} = \frac{1}{2}\left(\gamma_1 \dot{z}^2_{SB} + \gamma_2 \dot{z}^2_{OT} + \gamma_3 \dot{\theta z}^2_{SB} + \gamma_4 \dot{\theta y}^2_{SB} + \gamma_5 \dot{\theta x}^2_{OT} + \gamma_6 \dot{\theta y}^2_{OT}\right) \tag{5.24}$$

The external forces applied to the system can be written as

$$Q_{MGT} = \sum_{i=1}^{4} Fz^i_{Coil} + Fz_{Base} + Ftx_{Base} + Fty_{Base} \tag{5.25}$$

The meaning of the coordinates is described in table 5.1. We can rewrite equations 5.15-5.21 using only the Lagrangian coordinates

$$(\mathbf{q}, \mathbf{p}) = (z_{Base}, \theta x_{Base}, \theta y_{Base}, \psi^i, \eta^i, \dot{z}_{Base}, \dot{\theta x}_{Base}, \dot{\theta y}_{Base}, \dot{\psi}^i, \dot{\eta}^i) \quad i = 1, 2, 3 \tag{5.26}$$

5.2.3 IP Table Model

As shown in fig. 5.4 the IP table model is constituted by

- **11 Rigid Bodies**: 1 massive Base used to excite the system with respect to the ground in the horizontal DOFs, 1 Optical Table (OT), 1 Spring Box (SB), 4 Inverted Pendulum (IP) legs, 4 Horizontal CounterWeights (HCW) connected to the "magic wands" (see next subsection). The 4 Little Pendulums (LP) are not counted since their mass is considered null.
- **4 Linear Springs with viscous damping**: Together with the four wands, they constitute the Horizontal MGAS (HMGAS)
- **4 Angular Springs with viscous damping**: They are used to simulate the inverted pendulum Flex Joints (FJ).
- **6 Force Actuators**: Two of them are used to excite the Base, acting on its center of mass, the other four shake the system acting on points corresponding to the actual positions of the electromagnetic actuators.

Parameter	Description	Value
M_{Base}	Mass of the shaker base	10^{10} kg
M_{SB}	Mass of the spring box	281 kg
M_{OT}	Mass of the optical table	906 kg
M^i_{VCW}	Mass of the vertical wand counterweight of the i-th MGAS spring	0.1 kg
Ixx_{Base}	First diagonal component of the base inertia tensor	10^{10} kgm^2
Iyy_{Base}	Second diagonal component of the base inertia tensor	10^{10}kgm^2
Ixx_{SB}	First diagonal component of the SB inertia tensor	78.87 kgm^2
Iyy_{SB}	Second diagonal component of the SB inertia tensor	164.88 kgm^2
Ixx_{OT}	First diagonal component of the OT inertia tensor	254.3 kg
Iyy_{OT}	Second diagonal component of the OT inertia tensor	531.6 kg
kz^i_{LP}	z component of i-th little pendulum stiffness. The value is calculated using	$5.457 \cdot 10^9$ N/m
kz^i_{MGAS}	z component of i-th MGAS linear stiffness. The value is calculated using eq. 5.22.	89.3 N/m
L_{LP}	Little pendulum length	$25 \cdot 10^{-3}$ m
L^i_{VCW}	Arm lever of the vertical wand	0.2 m
l^i_{VCW}	Arm lever of the vertical wand. The value is calculated using eq. 5.11.	0.0952 m
$(\gamma_1, \gamma_2, \gamma_3, \gamma_4, \gamma_5, \gamma_6)$	Damping coefficients	(250, 75, 100, 250, 75, 100)
Excitations		
Fz^i_{Coil}	Force applied to the SB through the i-th MGAS actuator along z direction	
Fz_{Base}, Ftx_{Base}, Fty_{Base}	Forces/Torques applied to the Base along z, θ_x, θ_y directions respectively	
Lagrangian coordinates $(\mathbf{q}, \mathbf{p})$		
z_{Base}, $\dot{z}_{Base}$	Displacement and velocity of the base center of mass along z	
θx_{Base}, $\dot{\theta x}_{Base}$	Rotation and angular velocity of the base center of mass along θy	
θy_{Base}, $\dot{\theta y}_{Base}$	Rotation and angular velocity of the base center of mass along θy	
η^i, $\dot{\eta}^i$	Displacement and velocity of the MGAS along z	
ψ^i, $\dot{\psi}^i$	Displacement and velocity of the little pendulum along z	

Table 5.1: Parameters used in MGAS table analytical model

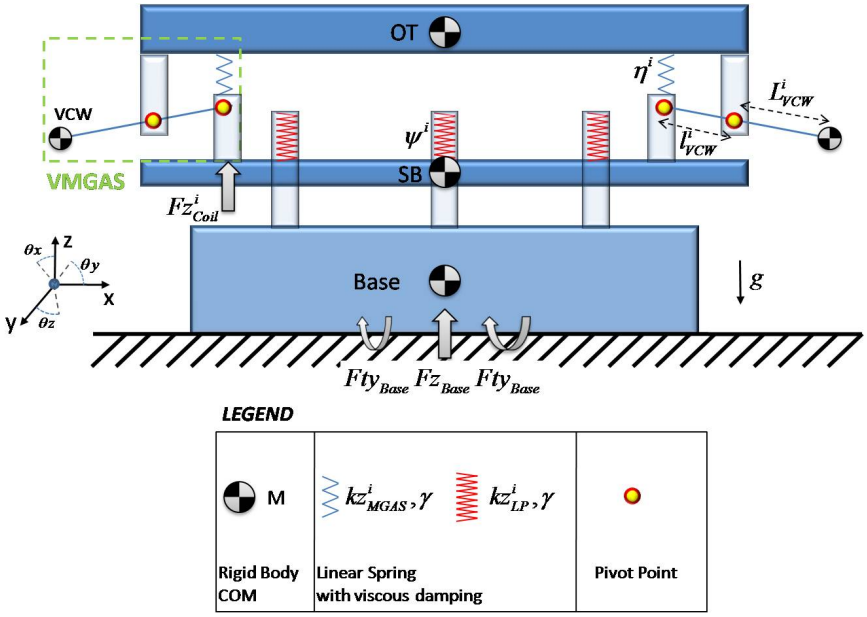

Figure 5.2: MGAS table model sketch viewed from the xz plane .

The inverted pendulum dynamics have been modeled with an ideal flexural joint connected to a leg with a counterweight as shown in figure 5.4. The transmissibility saturation has been tuned to about -60dB, which is a conservative number considering previous measurement with the HAM-SAS IP legs. IP Resonant frequency was tuned to 30 mHz, which is a frequency routinely obtained by Virgo superattenuators and also obtained by SAS prototypes.

In order to use the procedure described in last subsection we need to write the Lagrangian $\mathfrak{L}_{IPT}$, the dissipation function $\mathfrak{F}_{IPT}$ and the external forces Q_{IPT} of the IP table. We have

$$\mathfrak{L}_{IPT} = T_{IPT} - U_{IPT} \tag{5.27}$$

with

$$T_{IPT} = T_{Base} + T_{IP} + T_{SB} + T_{OT} + T_{HCW} \tag{5.28}$$

$$U_{IPT} = U_{Base} + U_{IP} + U_{SB} + U_{OT} + U_{HCW} + U_{FJ} + U_{MGAS} \tag{5.29}$$

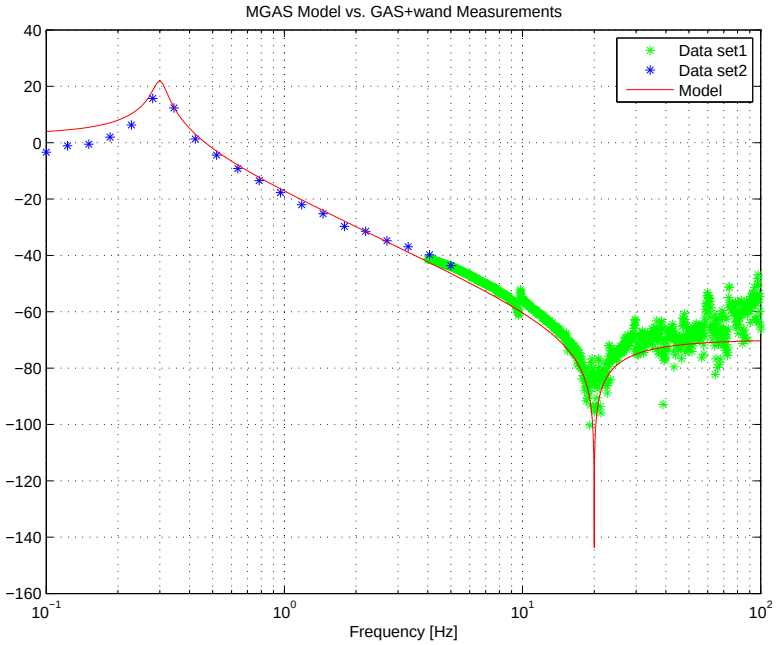

Figure 5.3: Comparison of modeled and experimental vertical transmissibility of an MGAS filter with assembled with a wand with a counterweight. Experimental data were taken in two separate measurements [38]: green asterisks Dataset #1, blue asterisks Dataset #2.

Using the coordinate system shown in figure 5.4 and the parameters described in table 5.2, we can write

$$T_{Base} = \frac{1}{2}M_{Base}\dot{x}_{Base} + \frac{1}{2}Izz_{Base}\dot{\theta z}^{2}_{Base} \tag{5.30}$$

$$T_{IP} = \sum_{i=1}^{4}\frac{1}{2}M^{i}_{IP}(\dot{x}^{i}_{IP})^2 + \frac{1}{2}Iyy^{i}_{IP}(\dot{\theta x}^{i})^2 \tag{5.31}$$

$$T_{SB} = \frac{1}{2}M_{SB}\dot{x}^2_{SB} + \frac{1}{2}Izz_{SB}\dot{\theta z}^{2}_{SB} \tag{5.32}$$

$$T_{OT} = \frac{1}{2}M_{OT}\dot{x}^2_{OT} + \frac{1}{2}Izz_{OT}\dot{\theta z}^{2}_{OT} \tag{5.33}$$

$$T_{HCW} = \sum_{i=1}^{4}\frac{1}{2}M^{i}_{HCW}\left(x_{SB} - \frac{l^{i}_{HCW}}{L^{i}_{HCW}}\dot{\xi}_i\right)^2 \tag{5.34}$$

and

$$U_{IP} = -\frac{1}{2}g\sum_{i=1}^{4}\frac{M_{IP}^{i}H_{IP}^{i}(\dot{\theta x}^{i})^{2}}{4} \tag{5.35}$$

$$U_{SB} = -\frac{1}{2}gM_{SB}\frac{\sum_{i=1}^{4}H_{SB}(\theta x^{i})^{2}}{4}+\frac{1}{2}gM_{SB}\frac{\sum_{i=1}^{4}L_{LP}^{i}(\phi x^{i})^{2}}{4} \tag{5.36}$$

$$U_{OT} = -\frac{1}{2}gM_{OT}\frac{\sum_{i=1}^{4}H_{OT}(\theta x^{i})^{2}}{4}+\frac{1}{2}gM_{OT}\frac{\sum_{i=1}^{4}L_{LP}^{i}(\phi x^{i})^{2}}{4} \tag{5.37}$$

$$U_{HCW} = \frac{1}{2}g\sum_{i=1}^{4}M_{HCW}^{i}l_{HCW}^{i}\left(\frac{\xi^{i}}{L_{HCW}^{i}}\right)^{2} \tag{5.38}$$

$$U_{FJ} = \frac{1}{2}\sum_{i=1}^{4}kx_{IP}^{i}(L_{IP}^{i}\theta x^{i})^{2} \tag{5.39}$$

$$U_{MGAS} = \frac{1}{2}\sum_{i=1}^{4}kx_{MGAS}^{i}(\xi^{i})^{2} \tag{5.40}$$

The flex joint stiffness have been evaluated imposing a resonance frequency $f_0 = 30$ mHz in eq.:

$$kx_{IP}^{i} = \frac{(2\pi f_0)^2}{Izz_{OT}+Iyy_{IP}^{i}+\frac{1}{4}(M_{OT}+M_{SB})L_{IP}^{i}+M_{IP}^{i}H_{IP}^{i}} +g\left[\frac{1}{4}(M_{OT}+M_{SB})+M_{IP}^{i}H_{IP}^{i}\right] \tag{5.41}$$

The Rayleigh's dissipation function of the system results

$$\begin{aligned}\mathfrak{F}_{IPT} = {} & \frac{1}{2}(\Gamma_1\dot{x}_{OT}^{2}+\Gamma_2\dot{\theta z}_{OT}^{2}+\Gamma_3\dot{x}_{SB}^{2}+\Gamma_4\dot{\theta z}_{SB}^{2}) \\ & +\frac{1}{2}\sum_{i=1}^{4}\gamma_i\left(\dot{x}_0^{i}\right)^{2}+\frac{1}{2}\sum_{i=1}^{4}\gamma_{i+4}\left(\dot{\theta x}_0^{i}\right)^{2} \\ & +\frac{1}{2}\sum_{i=1}^{4}\gamma_{i+8}\left(\dot{\phi x}^{i}\right)^{2}+\frac{1}{2}\sum_{i=1}^{4}\gamma_{i+12}\left(\dot{\xi}^{i}\right)^{2}\end{aligned} \tag{5.42}$$

The external forces applied to the system can be written as

$$Q_{IPT} = F_x^{Base}+F_y^{Base}+F_{\theta z}^{Base}+F_x^{Coil}+F_y^{Coil}+F_{\theta z}^{Coil} \tag{5.43}$$

As we have done in the previous subsection, all the equations 5.15-5.21 can be rewritten using only the Lagrangian coordinates

$$(\mathbf{q},\mathbf{p}) = (x_0^{i},\theta x^{i},\phi x^{i},\xi^{i},\dot{x}_0^{i},\dot{\theta x}_0^{i},\dot{\phi x}^{i},\dot{\xi}^{i}) \quad i=1,\ldots,4 \tag{5.44}$$

5.3 Ground Transmissibilities

The transmissibility is essentially a measure of how a mechanical system respond, in the frequency domain, to a generic excitation. Mathematically, the

Parameter	Description	Value
M_{Base}	Mass of the shaker base	10^{10} kg
M_{SB}	Mass of the spring box	281 kg
M_{OT}	Mass of the optical table	906 kg
M_{IP}^{i}	Mass of the i-th IP leg	2.608 kg
M_{HCW}^{i}	Mass of the horizontal wand counterweight of the MGAS springs	0.1 kg
Izz_{Base}	Third diagonal component of the base inertia tensor	10^{10} kgm^2
Iyy_{IP}	Second diagonal component of the IP leg inertia tensor	$5.99 \cdot 10^{-2}$ kgm^2
Izz_{SB}	Third diagonal component of the SB inertia tensor	281 kgm^2
Izz_{OT}	Third diagonal component of the OT inertia tensor	306 kgm^2
kx_{IP}^{i}	x component of i-th flex joint linear stiffness. The value is calculated using eq. 5.41.	5882 N/m
kx_{MGAS}^{i}	x component of i-th MGAS linear stiffness	12863 N/m
H_{OT}	Height of the optical table center of mass respect to the base.	0.650 m
H_{SB}	Height of the spring box center of mass respect to the base.	0.5 m
H_{IP}^{i}	Height of the IP leg center of mass respect to the base.	$6 \cdot 10^{-2}$m
L_{IP}^{i}	Inverted Pendulum leg length	0.5 m
L_{LP}	Little Pendulum length	$2.5 \cdot 10^{-3}$ m
L_{HCW}^{i}	Arm lever of the horizontal wand	0.2 m
l_{HCW}^{i}	Arm lever of the horizontal wand. The value is calculated using eq. 5.10.	0.0706 m
x_{IP}^{i}, $\dot{x}_{IP}^{i}$	Displacement and velocity of the i-th IP leg center of mass	—
x_{SB}, $\dot{x}_{SB}$	Displacement and velocity of the SB center of mass	—
x_{OT}, $\dot{x}_{OT}$	Displacement and velocity of the OT center of mass	—
Excitations		
F_{x}^{Base}, F_{y}^{Base}, $F_{\theta z}^{Base}$	Forces/Torques applied to the base along x, y and θz directions	
F_{x}^{Coil}, F_{y}^{Coil},$F_{\theta z}^{Coil}$	Forces/Torques applied to the SB along x, y and θz directions	
Lagrangian coordinates $(\mathbf{q}, \mathbf{p})$		
x_0^i, $\dot{x}_0^i$	Displacement e velocity of the i-th IP leg lower hinge point	
θx^i, $\dot{\theta x}^i$	Angle and angular velocity of the i-th IP leg respect to the vertical direction	
ϕx^i, $\dot{\phi x}^i$	Angle and angular velocity of the i-th LP leg respect to the vertical direction	
ξ^i, $\dot{\xi}^i$	Displacement and velocity of the i-th MGAS along x	

Table 5.2: Parameters used in IP table analytical model

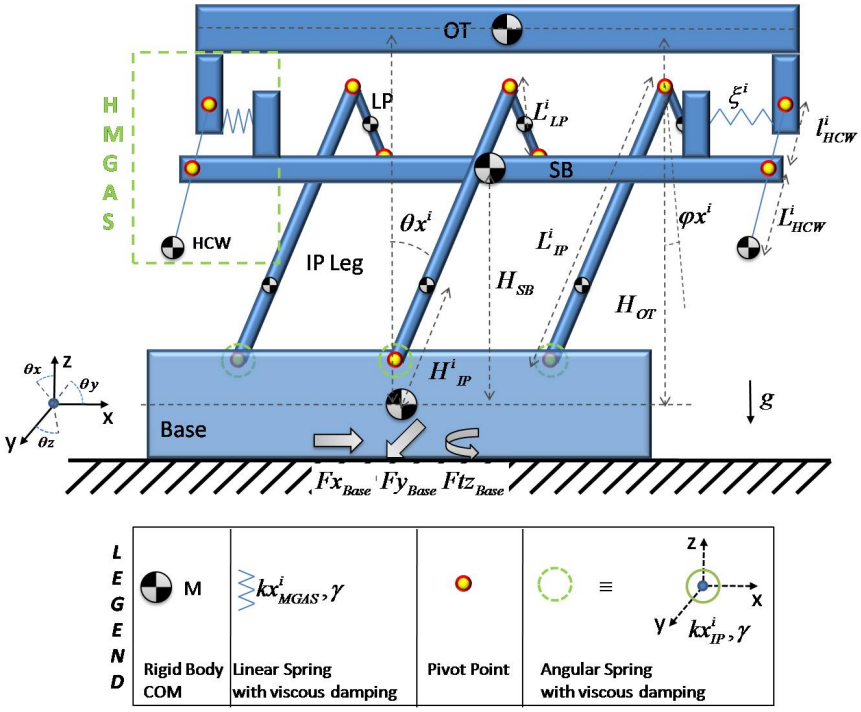

Figure 5.4: IP Table mechanical model sketch viewed from the xz plane.

transmissibility $T_i(s)$ along the i-th degree of freedom of a mechanical system is defined as the ratio, dependent on the Laplace variable $s = j\omega$,

$$T_i(s) = \frac{Q^i(s)}{Q_0^i(s)}$$

between the Laplace transform of the vibration $q^i(t)$ of the system and the Laplace transform of the excitation $q_0^i(t)$ applied to the system, along the i-th degree of freedom. For example, in the case of a simple unidimensional damped harmonic oscillator, excited with a sinusoidal displacement $x_0 \sin(\omega t)$, the transmissibility magnitude is

$$|T(s)| = \frac{x}{x_0} = \sqrt{\frac{1 + 4\gamma^2(\omega/\omega_0)^2}{(1 - (\omega/\omega_0)^2)^2 + 4\gamma^2(\omega/\omega_0)^2}}$$

where ω_0 is the oscillator resonance frequency and γ is the resonance damping factor.

The two state-space models generated by the Maple scripts have a total of 13 inputs and 18 outputs. The inputs are constituted by 7 force/torque actuators F^i placed on the system and 6 force/torque actuators F_0^i, one for every degree of freedom i, placed on an ideal infinite mass base platform, representing the ground, that is used to shake the system. In particular we have, for the IP table model, the inputs:

$$\mathbf{Q}_{IPT} = (\mathbf{F}^{IPT}, \mathbf{F}_0^{IPT}) = (F_x^{Coil}, F_y^{Coil}, F_{\theta z}^{Coil}, F_x^{Base}, F_y^{Base}, F_{\theta z}^{Base}) \quad (5.45)$$

and for the MGAS table

$$\mathbf{Q}_{MGT} = (\mathbf{F}^{MGT}, \mathbf{F}_0^{MGT}) = (Fz^i_{Coil}, Fz_{Base}, Ftx_{Base}, Fty_{Base}) \tag{5.46}$$

The outputs are composed by the 6 degrees of freedom of the optical table, of the spring box , q^i, and of the base, q^i_0, centers of mass. So we have

$$\mathbf{Y}_{IPT} = (x_{OT}, y_{OT}, \theta z_{OT}, x_{SB}, y_{SB}, \theta z_{SB}, x_{Base}, y_{Base}, \theta z_{Base}) \tag{5.47}$$

and

$$\mathbf{Y}_{MGT} = (z_{OT}, \theta x_{OT}, \theta y_{OT}, z_{SB}, \theta x_{SB}, \theta y_{SB}, z_{Base}, \theta x_{Base}, \theta y_{Base}) \tag{5.48}$$

The frames are oriented as shown in figures 5.4 and 5.2.

Transmissibilities from ground to the optical table center of mass and from ground to spring box center of mass for all the six degrees of freedom are shown in figures 5.5 and 5.6. To compute such transmissibilities we first calculate the transfer functions from generalized forces/torques F^i_0 applied to the shaker base, to the optical table and spring box degrees of freedom q^i. Then the transmissibilities have been obtained applying the proper transfer function ratios to remove the dependency on the generalized forces:

$$T_i(s) = \frac{Q^i(s)}{F^i_0(s)} \frac{F^i_0(s)}{Q^i_0(s)}$$

for the generic ith degree of freedom. Because internal modes are not included in the mechanical models, this simulations are valid up to approximately 50 Hz. Above that frequencies discrepancies are expected to be large especially around the internal mode frequencies due to effect of distributed masses.

The transmissibility generated by the model are

- **Horizontal x/x_0 transmissibility**. The blue and green curves of figure 5.5 upper plot are the transmissibilities of the horizontal degree of freedom x. The resonance at 30 mHz with very low quality factor corresponds to the inverted pendulum mode frequency. The 1.2 Hz resonance is due to the horizontal stiffness of the MGAS blades, which has been experimentally measured to be about 0.54 Hz using a MGAS filter prototype. Finally, the resonance at 103 Hz is due to the short pendulums which connect the inverted pendulum legs to the MGAS frame. The presence of this resonance is well known and has been confirmed by ANSYS FEM simulations [48]. Saturation above 2 Hz has been tuned using the inverted pendulum counter-weight to about -65 dB, which is considered a reasonable value after the past Virgo results and measurements on HAM-SAS legs.

- **Longitudinal y/y_0 transmissibility**. Because of the symmetry of the system, the transmissibility curves for the longitudinal degree of freedom y (red and cyan curves of figure 5.5 upper plot) are essentially the same as the x degree of freedom. Minor differences come from the moments of inertia and lever arms which are differ by less than 10% in the two orthogonal directions.

- **Yaw $\theta_z/\theta^{(0)}_z$ transmissibility**. The blue and green curves of figure 5.5 lower plot show the transmissibility for the angular degree of freedom θ_z (yaw).

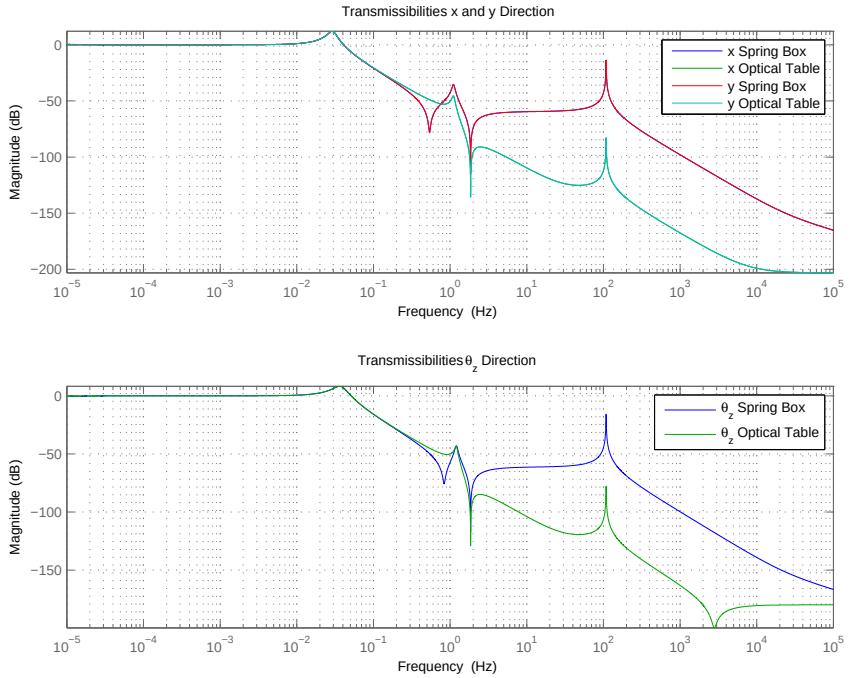

Figure 5.5: Transmissibilities for the horizontal (x, y) and (θ_z) degrees of freedom for a system with IPs tuned at 30 mHz.

- **Vertical z/z_0 transmissibility.** The blue and green traces of figure 5.6 upper plot show the transmissibility of the vertical degree of freedom z. The vertical resonance has been tuned at 100 mHz and the saturation has been set to about -80dB. Those values have been experimentally obtained for a MGAS with a payload of about the same of the HAM-SAS system. This saturation level can be reached using a properly tuned wand and counterweight. The major advantage in lowering the saturation levels is to reduce the magnitude of the internal resonances in the transmissibility curves. The quality factor for the vertical resonance was set to about 3.

- **Roll $\theta_x/\theta_x^{(0)}$ transmissibility**. The red and green traces of figure 5.6 lower plot show the transmissibility of the angular degree of freedom θ_x (roll). As expected this transfer function is similar to the vertical transfer function but with different resonant frequencies (the resonances depends on the moment of inertia of the payload and not just on the mass)

- **Pitch $\theta_y/\theta_y^{(0)}$ transmissibility**. The blue and magenta traces of figure 5.6 lower plot represent the transmissibility of the angular degree of freedom θ_y (pitch). The differences respect to the previous transmissibility are mainly due to the different moment of inertia about the x and y axis.

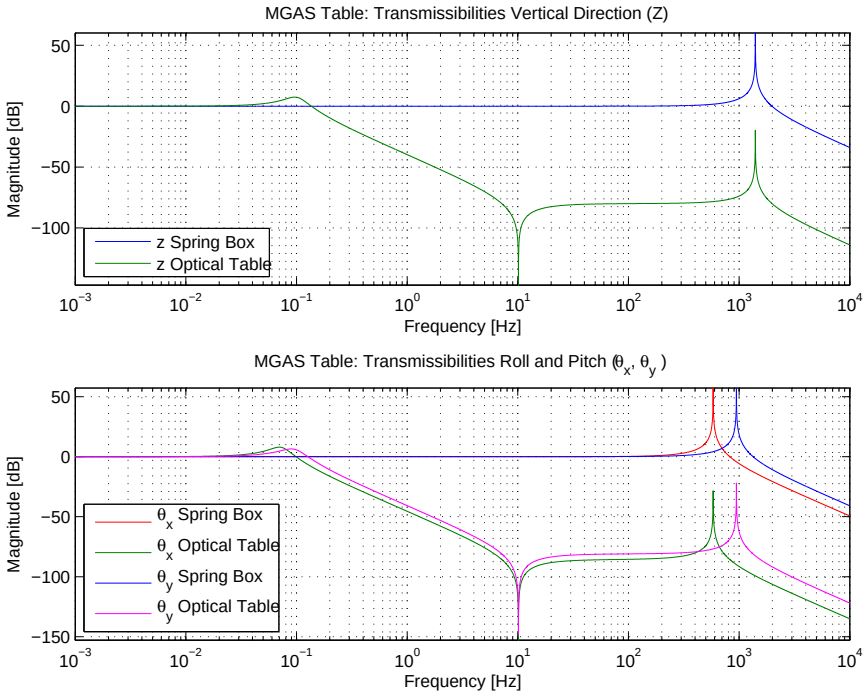

Figure 5.6: Transmissibilities for the vertical (z), pitch and roll (θ_x, θ_y) degrees of freedom for a system with MGAS tuned at 100 mHz with 80 dB attenuation factor.

5.4 Attenuation Performance

The seismic noise reference spectra of Hanford (LHO) and Livingston (LLO) sites, used to estimate the attenuation of the horizontal and vertical seismic spectra, are based on AdLIGO Seismic Isolation requirements design document [52]. The horizontal and vertical ground noise are considered equal and expressed, in the frequency range 100 mHz$<f<$40 Hz, as a polynomial expansion in log space:

$$\log x_g(f) = p_1(\log f)^n + p_2(\log f)^{n-1} + \cdots + p_n \log f + p_{n+1}$$

where $x_g(f)$ is the displacement spectral density. The LHO and LLO reference spectra have been merged and extrapolated below 100 mHz using the USGS New Low Noise Model developed by J.Peterson (see 2.3.1). The ground tilt noise was generated in the 10 mHz - 40 Hz band using the Rayleigh waves propagation model [51]. In this model the ground tilt noise spectrum is proportional to the vertical component of Rayleigh waves through the relation:

$$\theta_g(\omega) = \frac{\omega}{c} S_v$$

where $\theta_g(\omega)$ is expressed in rad/$\sqrt{\text{Hz}}$, S_v is the vertical seismic motion and c is the local speed of seismic waves. This is probably an underestimation of the actual LIGO sites angular noise especially because of asymmetries and of the

internal modes of the HAM supporting structure at low frequencies which introduce phase delays in the noise propagation. Direct measurements are needed to estimate the amount of angular noise.

The requirements, contained in document [52], set a displacement noise limit, for the Power Recycling and Mode Cleaner optics, of $2\text{x}10^{-7}\text{m}/\sqrt{\text{Hz}}$ in 0.1-0.2 Hz band, $2\text{x}10^{-13}\text{m}/\sqrt{\text{Hz}}$ at 10 Hz and $3\text{x}10^{-14}$ $\text{m}/\sqrt{\text{Hz}}$ above 10 Hz.

The spectra obtained filtering LHO and LLO combined seismic noise with the HAM-SAS model are:

- x/x_0 **power spectrum**. Figure 5.7 shows the reference spectrum, the design requirement spectrum and two predicted attenuated spectra for the horizontal degree of freedom. The blue curve is obtained considering the inverted pendulum resonant frequency tuned at 20 mHz and the red curve with the IP tuned at 30mHz. The red curve shows that requirements cannot be met in the 0.8-1.5 Hz interval. There are essentially three possible solutions to this problem that can be combined together. The first solution is to tune the notch produced by the inverted pendulums counterweight at the MGAS resonant frequency to add passive attenuation in correspondence of that MGAS horizontal resonance. The second solution is to tune the inverted pendulum resonance frequency at 20 mHz as shown in the red curve. Finally the third solution is to use the active damping control to reduce the height of 1.2 Hz resonance.

- y/y_0 **power spectrum**. The filtered seismic noise spectrum for the horizontal degree of freedom y is not reported because is essentially the same as the x horizontal degree of freedom. In fact the only differences comes from a slight difference on the two horizontal transmissibilities.

- $\theta_z/\theta_z^{(0)}$ **power spectrum**. Figure 5.8 shows the filtered and unfiltered power spectral density of the angular degree of freedom θ_z (yaw). Requirements are met everywhere with a quite large safety margin. As in the other angular degrees of freedom, the angular noise roughly translates into position noise expressed in meters. As previously mentioned, it is important to notice that the angular noise spectrum could be underestimated.

- z/z_0 **power spectrum**. Figure 5.9 shows the filtered and unfiltered power spectral density of the vertical degree of freedom z. Using a 100 mHz MGAS resonance frequency, even with a -80dB saturation, experimentally reached with magic wands, requirements cannot be met. However this problem does not compromise HAM-SAS performance because HAM chambers requirements defined in [52] are probably too stringent. A study performed by P. Fritschel [53], one of the authors of the original seismic requirement document, has shown that the Mode Cleaner noise limit at 10 Hz can be increased of 1-2 orders of magnitude with no problem for AdLIGO target sensitivity. We have also to notice that considering the horizontal and vertical components of seismic noise to be equal causes an overestimation of the real displacement noise along vertical direction.

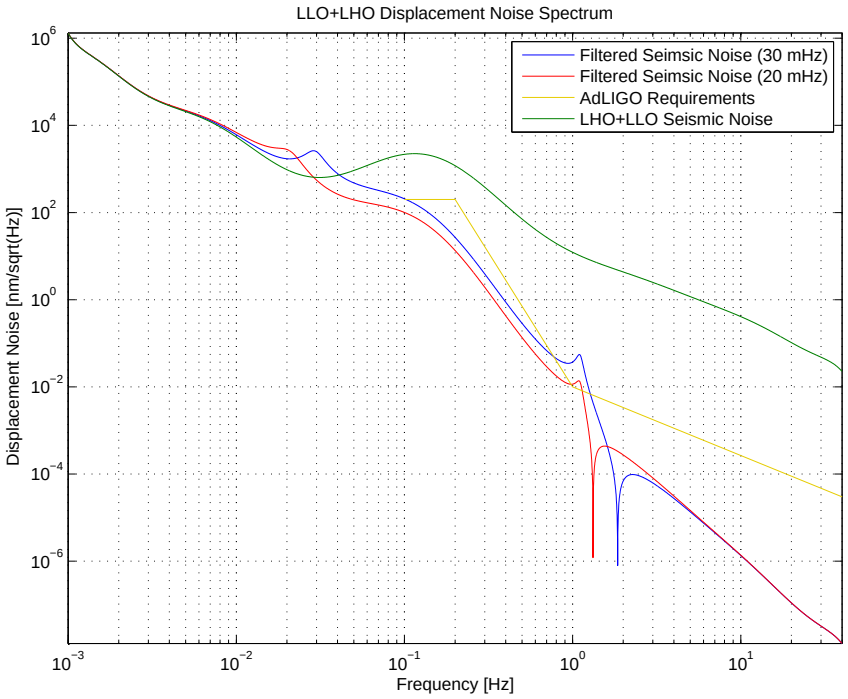

Figure 5.7: Seismic noise square-root power spectral densities of the horizontal (x) degree of freedom: gold curve required AdLIGO noise performance, green curve LHO+LLO seismic noise model, blue and red curve filtered seismic noise for a system with IPs tuned at 30 mHz and 20 mHz respectively.

- $\theta_x/\theta_x^{(0)}$ **and** $\theta_y/\theta_y^{(0)}$ **power spectra**. Figure 5.10 shows the filtered and unfiltered power spectral density of the angular degree of freedom θ_x (roll). Requirements are met everywhere with a quite large safety margin. Because the arm lever of the triple pendulum supporting frame is about 1 m long, the angular noise translates directly into meters. It is again important to mention that the ground angular noise spectrum could be underestimated.

5.5 Effect of Asymmetric Parameters

A preliminary study on the effects of the introduction of asymmetric parameters in the model have been performed. This has done in order to help to determine the precision required for HAM-SAS construction and assembly.

Two cases have been considered:

- **Asymmetric IP leg lengths**: Two of the four IP legs have lengths different (-1 mm$< \Delta l <$1 mm) from the design value i.e. the intermediate and top platforms are inclined by an angle θ_x or θ_y respect to the ground. This case has to be considered because it's difficult to manufacture metallic surfaces of the dimension required for the top and intermediate platforms

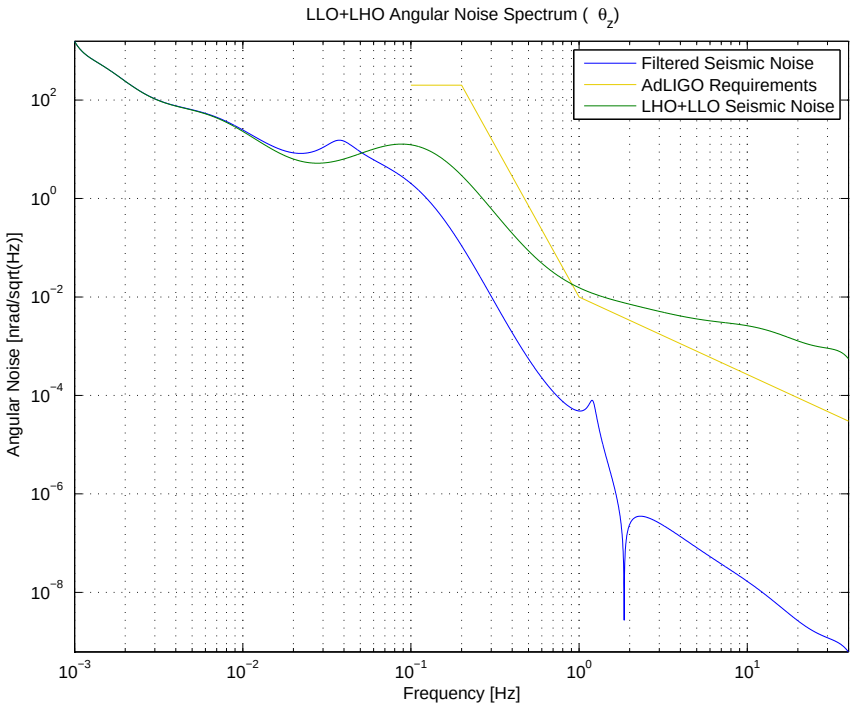

Figure 5.8: Seismic noise square-root power spectral densities of the yaw (θ_z) degree of freedom: gold curve required AdLIGO noise performance, green curve LHO+LLO seismic noise model, blue and red curve filtered seismic noise for a system with IPs tuned at 30 mHz.

(1.9 x 1.7 m) with an high level of planarity . The transmissibilities and the filtered seismic spectral densities for the horizontal and yaw degrees of freedom are shown in figures 5.11 and 5.12 respectively. As expected, the asymmetry introduces a coupling between the horizontal and angular directions. This causes the IP tuning frequency along the excited direction to change and to mix with the main resonance frequency of the non-excited degree of freedom. Since, as shown in fig. 5.7, the height of 1.2 Hz resonance depends strongly on the IP tuning frequency, when the system is excited along x, the 0.8 - 1.5 Hz region is over the requirements in the case of positive Δl and under them in the case of negative Δl. When the system is excited along θ_z instead, we can see that AdLIGO requirements are met with a good margin even with an asymmetric system. As before, we have to notice that ground angular seismic noise spectrum could be underestimated.

- **Asymmetric MGAS elastic constants**: Two of the four MGAS springs have elastic constants different ($-0.2k_0 < \Delta k < 0.2k_0$) from the design value k_0. Since MGAS are systems in a quasi-equilibrium state, a precise tuning of the spring box is very difficult. For this reason, in the real system, a 10% error in the value of the elastic constants is expected. The transmissibilities for the vertical, pitch and roll degrees of freedom

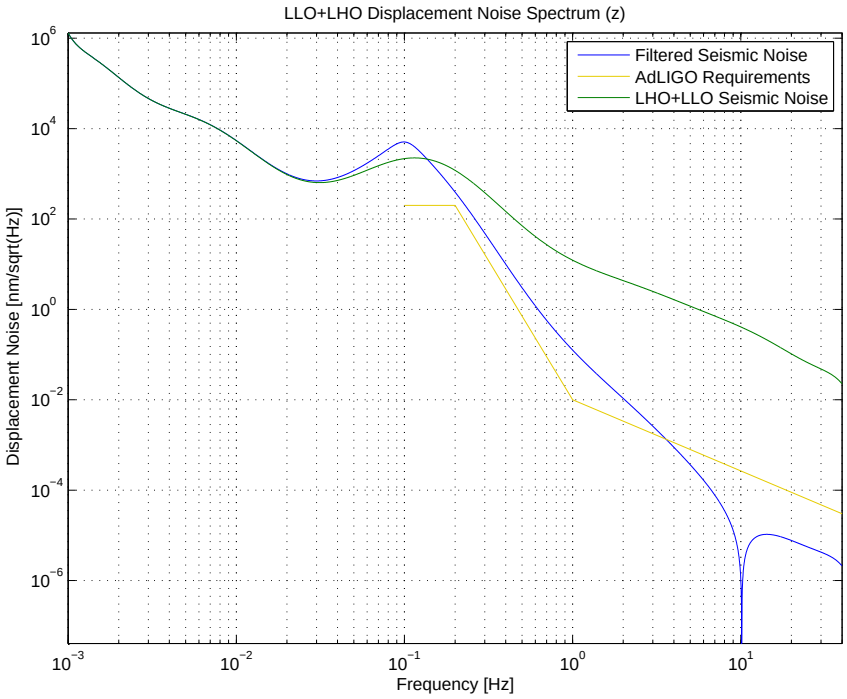

Figure 5.9: Seismic noise square-root power spectral densities of the vertical (z) degree of freedom: gold curve required AdLIGO noise performance, green curve LHO+LLO seismic noise model, blue and red curve filtered seismic noise for a system with MGAS tuned at 100 mHz with 80 dB attenuation factor.

are shown in figures 5.13 and 5.14 respectively. In order to amplify the effects of asymmetry, the quality factors of all resonances are set to infinity. Looking at the 60 - 140 mHz region we can see, as in the asymmetric IP table case, the presence of coupling between the vertical and angular degrees of freedom. However, unlike the previous case, the effects are very small and become completely negligible when we use the expected resonance quality factors. This result is expected since for an ideal spring the resonance frequency $f_0 \propto \sqrt{k_0}$.

These results have been presented at the August 2006 LIGO Scientific Collaboration Meeting.

5.6 Mode Cleaner suspension model

Every HAM vacuum chamber is equipped with a so called Triple suspension (see subsection 3.3.1.2). The triple pendulum external cage is supported by the optical table, that will be placed on HAM-SAS top platform. In this way the motion of the test mass will be attenuated by both HAM-SAS and the Triple suspension. It's therefore important to study the combined attenuation of the two systems.

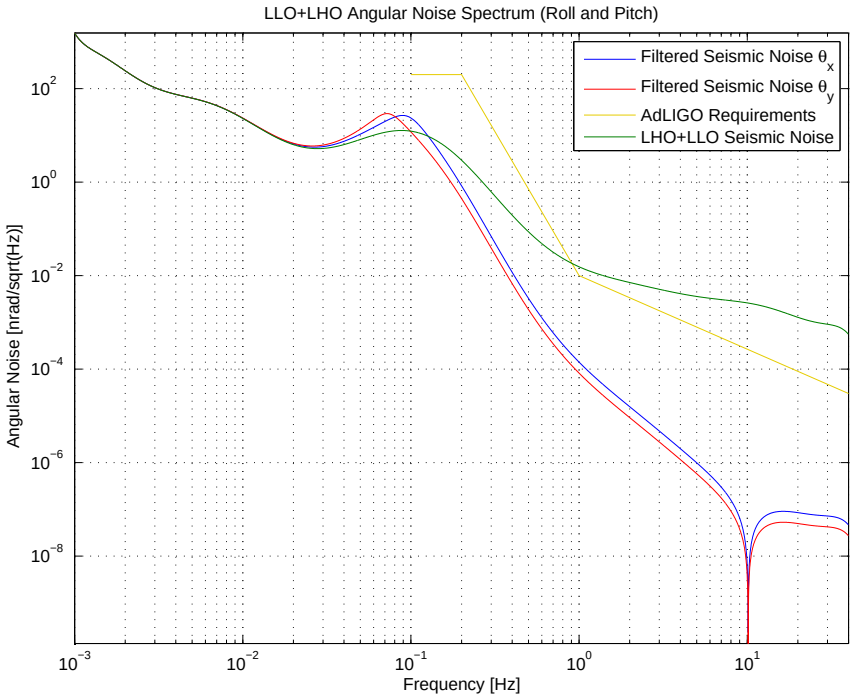

Figure 5.10: Seismic noise square-root power spectral densities of the roll (θ_x) and pitch (θ_y) degrees of freedom: gold curve required AdLIGO noise performance, green curve LHO+LLO seismic noise model, blue and red curve filtered seismic noise for a system with MGAS tuned at 100 mHz with 80 dB attenuation factor.

For this reason, in order to allow a preliminary study of the combined suspensions system, an independent model for the horizontal degrees of freedom of the Triple suspension has been developed. The model, shown in the sketch of figure 5.15, uses the same approach and code structure of the HAM-SAS simulation. Similarly to what we have done before, an ideal infinite mass platform, placed at the suspension point of the pendulum chain, is used to shake the system. The Lagrangian of the mode cleaner triple suspension, $\mathfrak{L}_{MCT}$, can be written as

$$\mathfrak{L}_{MCT} = T_{SP} + T_{MC} - U_{MC} \tag{5.49}$$

where

$$T_{SP} = \frac{1}{2} M_{SP} \dot{x}_{SP}^2 + \frac{1}{2} Izz_{SP} \dot{\theta z}_{SP}^2 \tag{5.50}$$

$$T_{MC} = \sum_{i=1}^{3} \frac{1}{2} M_{MC}^i \left(\dot{x}_{MC}^i\right)^2 + \frac{1}{2} Izz_{MC}^i \left(\dot{\theta z}_{MC}^i\right)^2 + \frac{1}{2} Ixx_{MC}^i \dot{\phi}_i^{\,2} \tag{5.51}$$

$$U_{MC} = \frac{1}{2} g \sum_{i=1}^{3} M_{MC}^i H_{MC}^i \frac{(\theta_1^i)^2 + (\theta_2^i)^2}{2} + \frac{1}{2} g \sum_{i=1}^{3} M_{MC}^i h_{MC}^i (\phi^i)^2 \tag{5.52}$$

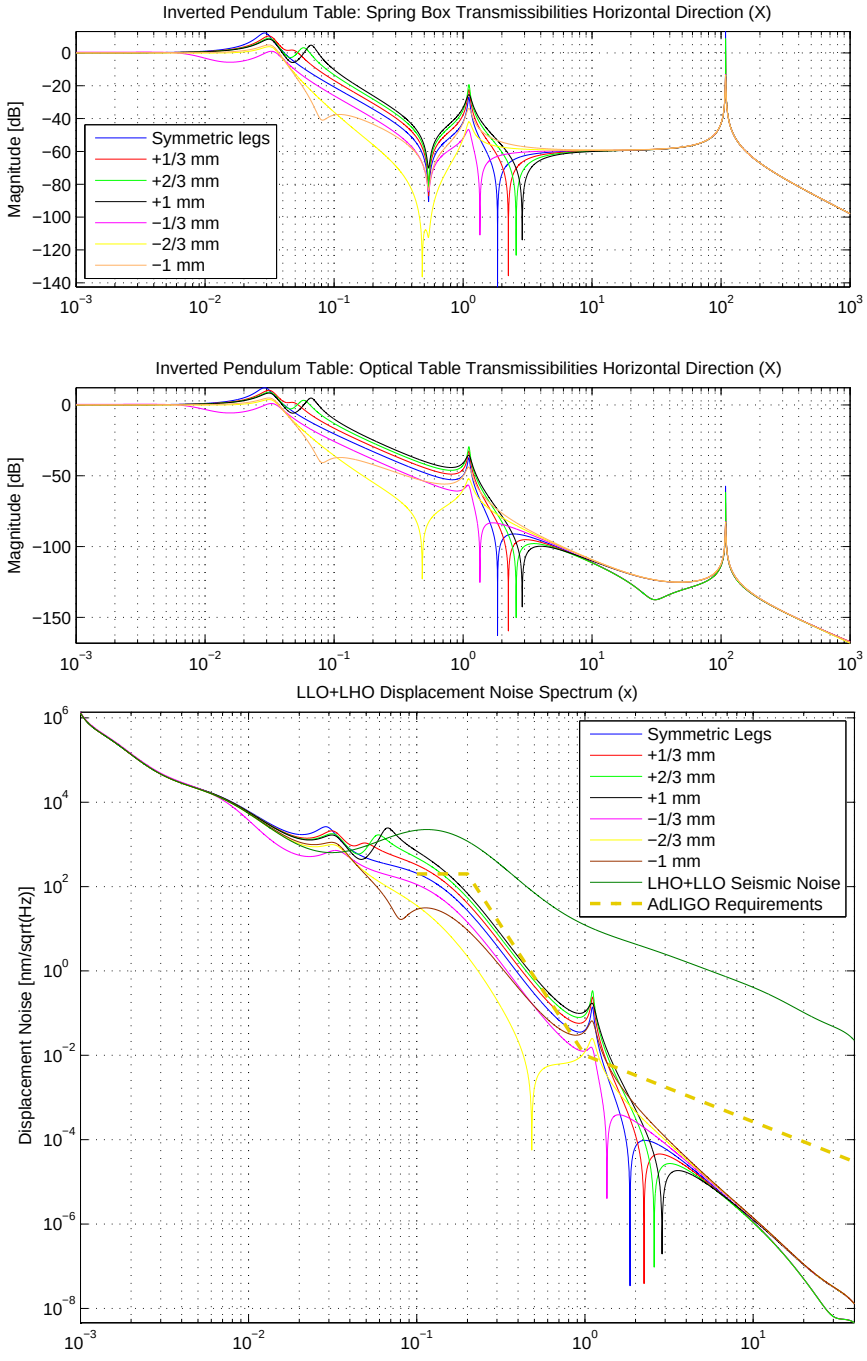

Figure 5.11: Effect of asymmetric IP leg lengths in the horizontal (x) transmissibility. The 30 mHz IP resonance frequency changes, due to the expected coupling between rotational and translational degrees of freedom. In the lower plot are shown the effects of asymmetry on the seismic attenuation performance.

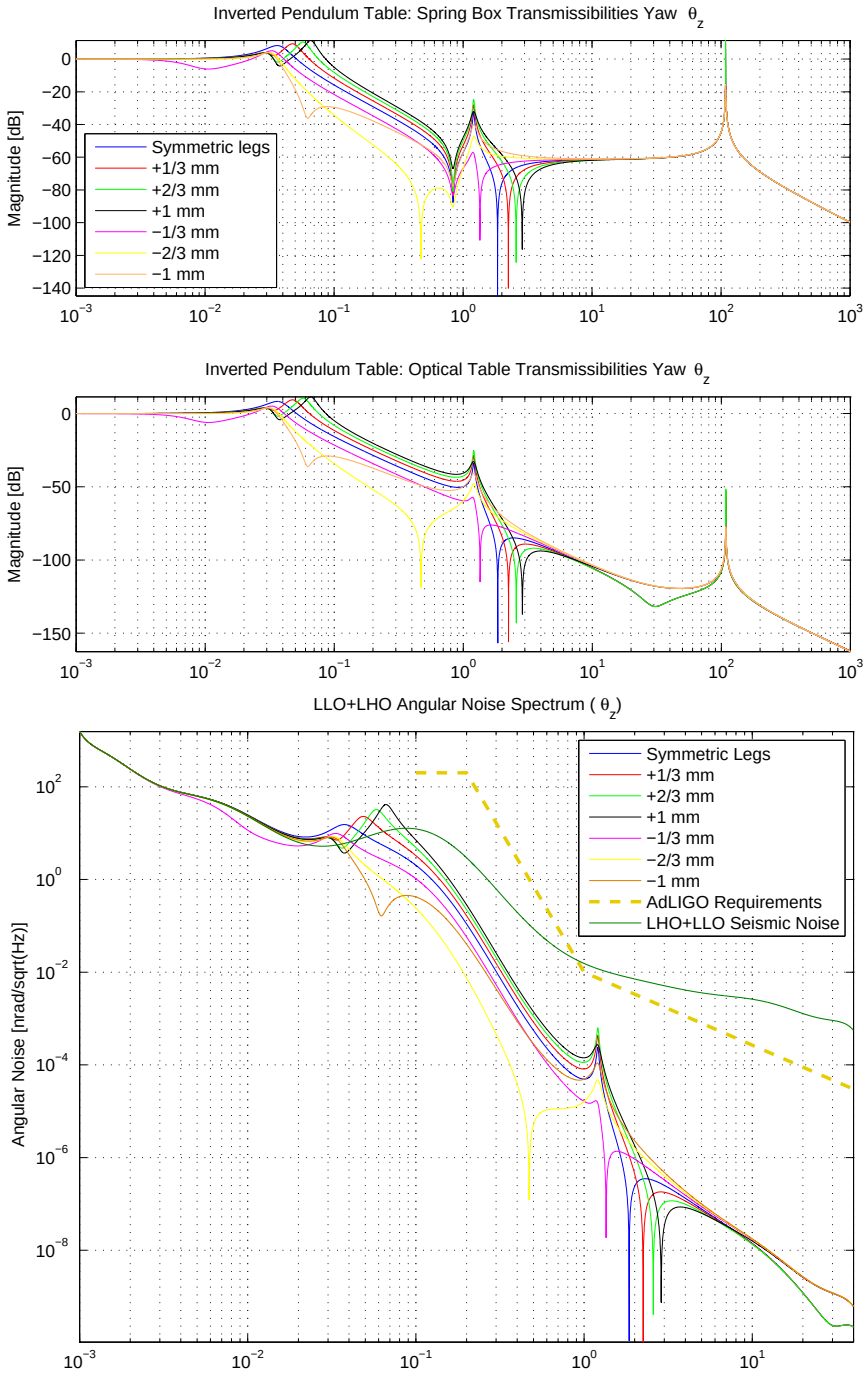

Figure 5.12: Effect of asymmetric IP leg lengths in the yaw (θ_z) transmissibility. The 30 mHz IP resonance frequency changes, due to the expected coupling between rotational and translational degrees of freedom. In the lower plot are shown the effects of asymmetry on the seismic attenuation performance.

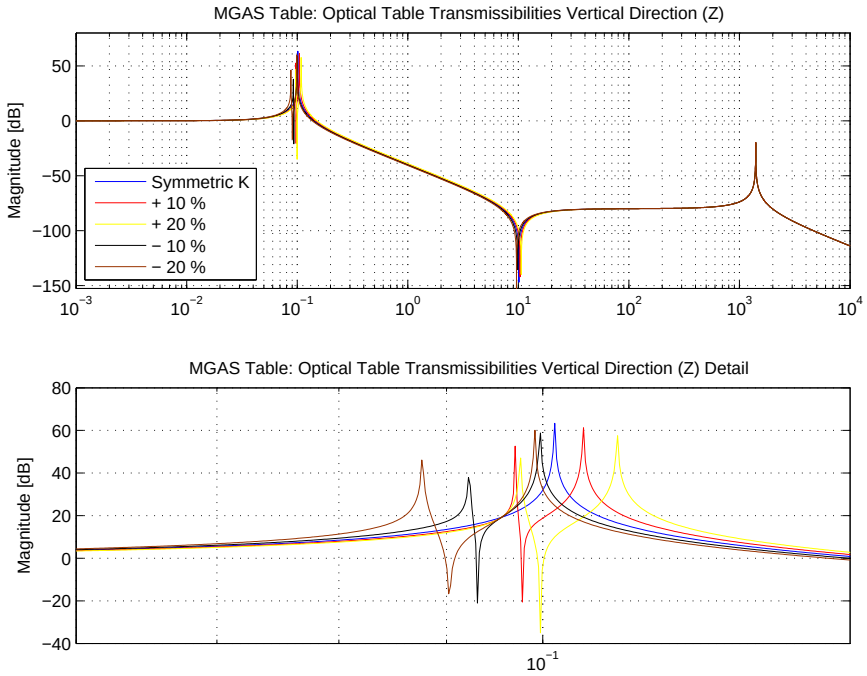

Figure 5.13: Effect of asymmetric MGAS elastic constants in the vertical (z) transmissibility. In the lower plot, detail of the region 60 mHz< f <140 mHz. The quality factors of all resonances are set to infinity in order to amplify the coupling effects.

The external forces applied to the system are

$$Q_{MCT} = \sum_{i=1}^{3} Fx^i + \sum_{i=1}^{3} Ft^i + Fx_{SP} + Ft_{SP} \tag{5.53}$$

The Mode Cleaner suspension model dissipation function is

$$\mathfrak{F}_{MCT} = \frac{1}{2}\sum_{i=1}^{3} \gamma_i \left(\dot{x}^i_{MC}\right) + \frac{1}{2}\gamma_4 \dot{x}_{SP} + \frac{1}{2}\gamma_5 \dot{\theta} z_{SP} \tag{5.54}$$

The description and the values of the parameters are summarized in table 5.3. Again we use a coordinate transformation in order to rewrite the equations in the generalized coordinates

$$(\mathbf{q}, \mathbf{p}) = \left(x_{SP}, \theta_1^i, \theta_2^i, \phi^i, \dot{x}_{SP}, \dot{\theta_1}^i, \dot{\theta_2}^i, \dot{\phi}^i\right) \quad i = 1, 2, 3 \tag{5.55}$$

The generated state-space representation has 8 inputs and 9 outputs. The horizontal transmissibilities obtained from the model are shown in the upper two plots of figure 5.16.

Thanks to the modular structure of the code, the connection of the Triple Pendulum to the HAM-SAS system can be done, just making a single coordinate transformation and adding the respective Lagrangian:

$$\mathfrak{L}_{MCS} = \mathfrak{L}_{MCT} + \mathfrak{L}_{IPT}$$

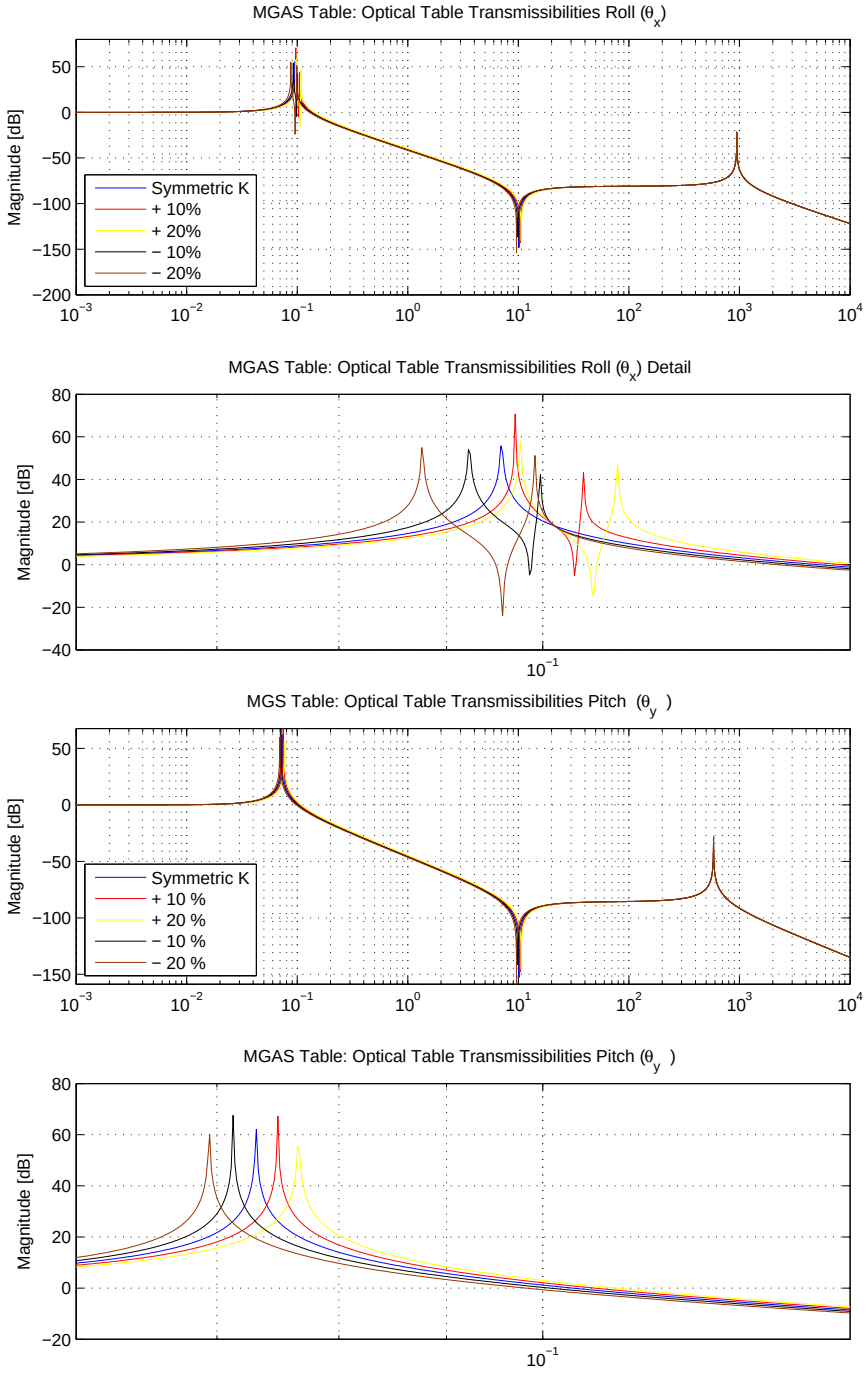

Figure 5.14: Effect of asymmetric MGAS elastic constants in the pitch and roll (θ_x, θ_y) transmissibilities. In the lower plots, detail of the region 60 mHz< f <140 mHz. The resonances quality factors are set to infinity in order to amplify the coupling effects.

. Therefore the Lagrange coordinate set for the complete model is

$$\begin{aligned}(\mathbf{q},\mathbf{p}) \quad = \quad & \big(x_0^i, \theta x^i, \phi x^i, \xi^i, \dot{x_0}^i, \theta_1^k, \theta_2^k, \phi^k, \\ & \dot{\theta x_0}^i, \dot{\phi x}^i, \dot{\xi}^i, \dot{\theta_1}^k, \dot{\theta_2}^k, \dot{\phi}^k\big) \quad i = 1,\ldots,4 \quad k = 1,2,3\end{aligned} \tag{5.56}$$

The Triple shaking platform coordinates does not appear since the excitation is applied to the IP table base.

In figure 5.16 are shown the transmissibilities of the Triple Suspension combined with HAM-SAS in the horizontal (x) and yaw (θ_z) degrees of freedom for the Spring Box, Optical Table, Triple Pendulum suspension point (MC_SP_X), Triple Pendulum top (MC_X[1]), intermediate (MC_X[2]) and test (MC_X[3]) mass. We can see the triple pendulum resonance frequencies, in 0.67 - 1.5 Hz region, and the three levels of attenuation introduced by three masses at higher frequencies.

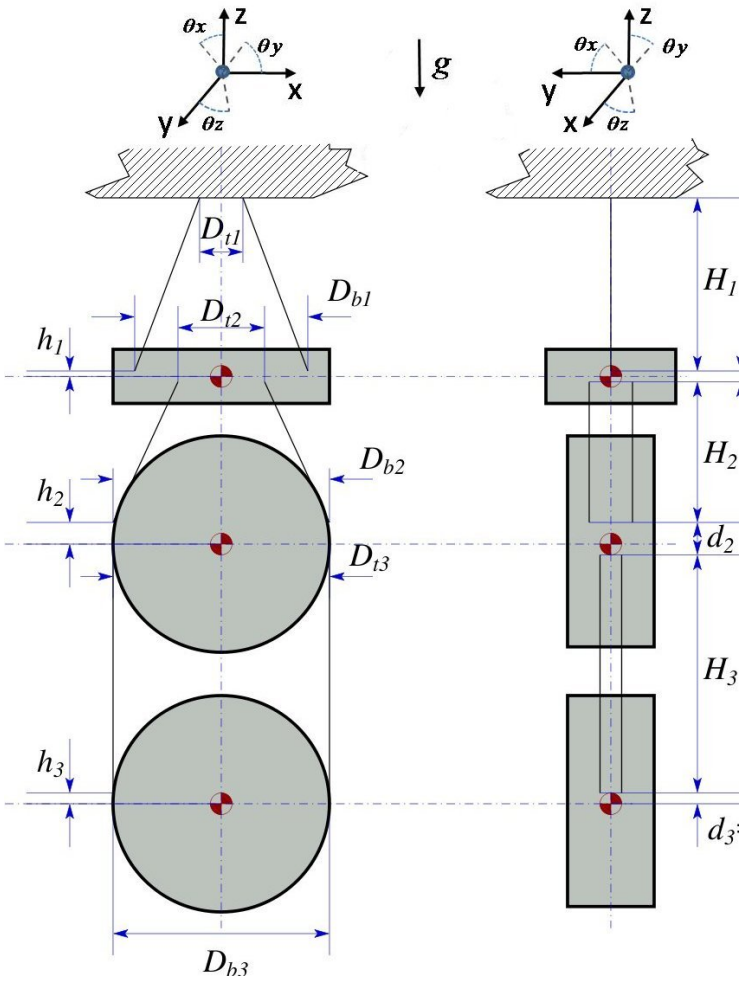

Figure 5.15: Sketch of the Triple Suspension mechanical model developed.

Parameter	Description	Value
M_{SP}	Mass of the shaking platform	10^{12} kg
Izz_{SP}	Third diagonal component of the shaking platform	10^{12}kgm^2
M^1_{MC}	Mass of the TP first mass	3.110 kg
M^2_{MC}	Mass of the TP intermediate mass	2.979 kg
M^3_{MC}	Mass of the TP test mass	3.040 kg
Ixx^1_{MC},	First diagonal component of the TP first mass inertia tensor	$2.4 \cdot 10^{-3}$ kgm^2
Ixx^2_{MC}	First diagonal component of the TP intermediate mass inertia tensor	$5.64 \cdot 10^{-3}$ kgm^2
Ixx^3_{MC}	First diagonal component of the TP test mass inertia tensor	$5.65 \cdot 10^{-3}$ kgm^2
Izz^1_{MC}	Third diagonal component of the TP first mass inertia tensor	$2.38 \cdot 10^{-2}$ kgm^2
Izz^2_{MC}	Third diagonal component of the TP intermediate mass inertia tensor	$5.74 \cdot 10^{-3}$ kgm^2
Izz^3_{MC}	Third diagonal component of the TP test mass inertia tensor	$5.89 \cdot 10^{-3}$ kgm^2
H^1_{MC}	Distance along z between the upper suspension points of the TP top mass and the lower suspension points of the shaking platform	0.294 m
H^2_{MC}	Distance along z between the upper suspension points of the TP intermediate mass and the lower suspension points of the TP test mass	0.163 m
H^3_{MC}	Distance along z between the upper suspension points of the TP test mass and the lower suspension points of the TP intermediate mass	0.22 m
h^1_{MC}	Distance along z between the first mass COM and its upper suspension points	$5.0 \cdot 10^{-3}$ m
h^2_{MC}	Distance along z between the intermediate mass COM and its upper suspension points	$1.0 \cdot 10^{-3}$ m
h^3_{MC}	Distance along z between the test mass COM and its upper suspension point	$2.5 \cdot 10^{-3}$ m
Db^1_{MC}	Distance along x between the upper suspension points of the TP first mass	0.2 m
Db^2_{MC}	Distance along x between the upper suspension points of the TP intermediate mass	0.153 m
Db^3_{MC}	Distance along x between the upper suspension points of the TP test mass	0.153 m
$(\gamma_1, \gamma_2, \gamma_3, \gamma_4, \gamma_5)$	Damping coefficients of the dissipation function 5.54.	(0.1, 0.1, 0.1, 10^3, 10^3)
Excitations		
Fx_{SP}, Ft_{SP}	Forces/Torques applied to the suspension point shaking platform	
Fx^i, Ft^i	Forces/Torques applied to the i-th TP mass	
Lagrangian coordinates $(\mathbf{q}, \mathbf{p})$		
x_{SP}, $\dot{x}_{SP}$	Displacement and velocity of the SP shaking platform COM along x	
θ^i_1, $\dot{\theta_1}^i$	Rotation and angular velocity of i-th TP mass upper suspension points along θ_y	
θ^i_2, $\dot{\theta_2}^i$	Rotation and angular velocity of i-th TP mass lower suspension points along θ_y	
ϕ^i, $\dot{\phi}^i$	Rotation and angular velocity of i-th TP mass along θ_z	

Table 5.3: Parameters of the mode cleaner triple suspension analytical model

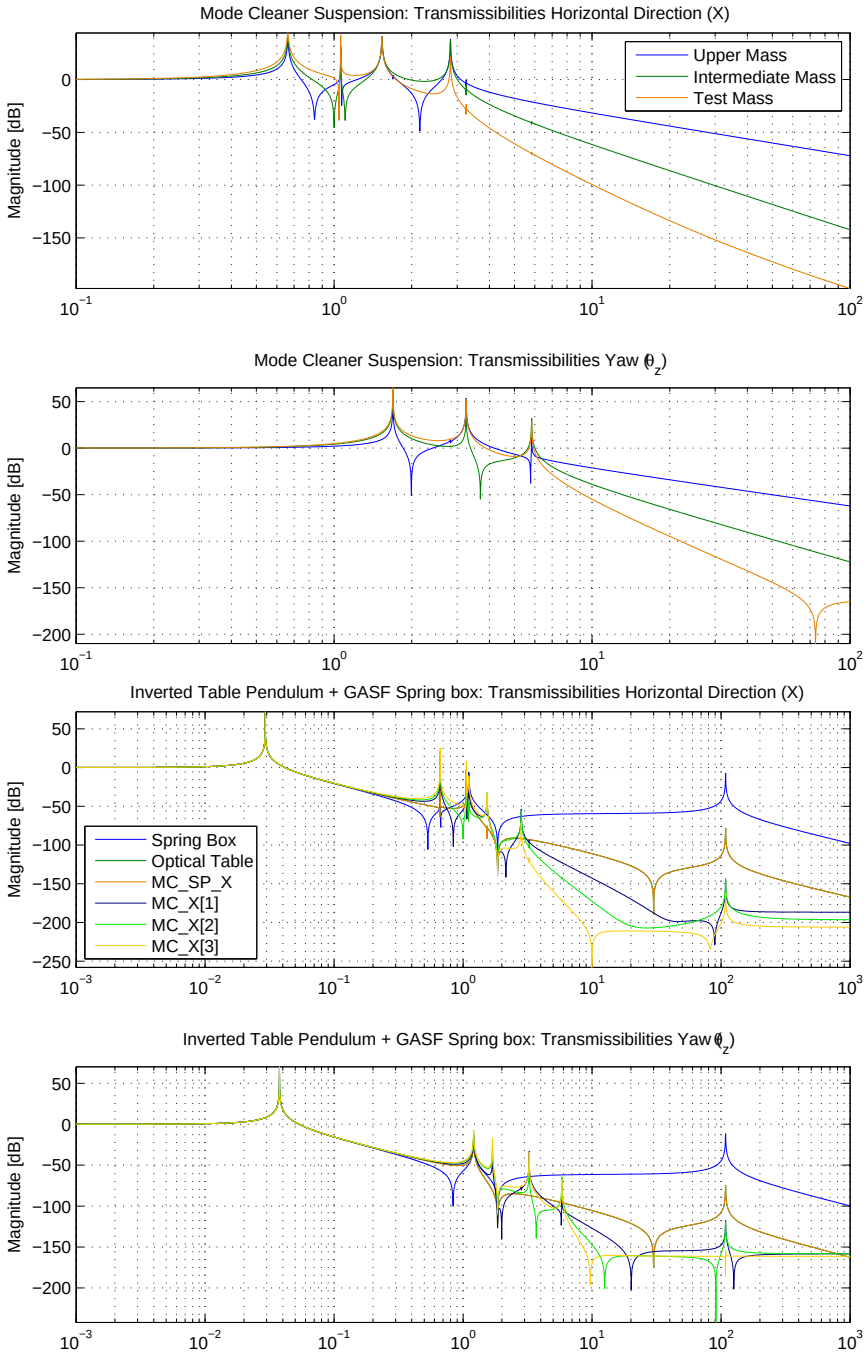

Figure 5.16: Upper two plots: Transmissibilities of the Triple Suspension in the horizontal (x) and yaw (θ_z) degrees of freedom for the top (MC_X[1]), intermediate (MC_X[2]) and test (MC_X[3]) mass. Lower two plots: Transmissibilities of the Triple Suspension combined with HAM-SAS in the horizontal (x) and yaw (θ_z) degrees of freedom for the Spring Box, Optical Table, Triple Pendulum suspension point (MC_SP_X), Triple Pendulum top (MC_X[1]), intermediate (MC_X[2]) and test (MC_X[3]) mass. The quality factors of all resonances are set to infinity.

Chapter 6

HAM-SAS Numerical Multibody Modeling

Since all the Lagrangians have to be written manually, the development of analytical models can be time consuming and error prone. At the same time the models described in last chapter neglect factors like small misalignments of the spring box with respect to the horizontal plane or the uneven balancing of the mass on the optics table, and other effects of a not optimal tuning of the system which generate the cross-talk among the DOFs observed in the actual prototype (see subsection 4.2.2).

For these reasons we explored several multibody simulations tools that could represent an alternative to analytical modeling. In particular we developed a series of toy models in DynaflexPro and SimMechanics, two commercial packages respectively produced by Mathworks and Maplesoft. Dynaflex Pro is based on Graph-Theoretic Dynamics [54], a modeling approach to multibody simulation that use graph theory in order to calculate the system equations of motion, while SimMechanics uses Simulink environment to represent a mechanical system with a hierarchical connected block diagram and integrate its equations of motion in the time domain. Even though simple systems produced the expected results, when we increased the complexity of the models, we encountered several problems with both tools. In particular we were unable to obtain accurate state space representations of the systems.

We then decided to test the open source package MBDyn (MultiBody Dynamics) and we started a collaboration with the developers to improve some of its features. Since this software is used to simulate stiff structures such as helicopter rotors, it was never tested a the very low frequency regimes required to simulate HAM-SAS dynamics. The results we have obtained are discussed in this chapter and in the next one.

6.1 MBDyn simulation software

MBDyn is an open-source multibody analysis tool [55, 56] developed at the Politecnico di Milano, extensively used in the aerospace field, that allows to analyze the dynamics of complex non-linear multibody systems in the time domain. From a numerical point of view, it is a solver of Differential-Algebraic-

Equations (DAE) that uses a family of implicit multistep integration algorithms in predictor-corrector form. We will discuss some details of this integration scheme in the next chapter.

In MBDyn a mechanical system is represented as a set of nodes, bodies, joints and external forces, described in an input text file. Nodes and bodies can simply be viewed as owners of kinematic (the nodes) and dynamic (the bodies) DOFs while joints are essentially the constrains between the nodes. MBDyn generates an output constituted by several ASCII files with different extensions. In particular the `.mov` file contains the motion data of every node in the system, calculated at each time step, respect to an inertial reference frame connected to ground. The data are constituted by the position and velocity of the nodes along the translational $(x, y, z, \dot{x}, \dot{y}, \dot{z})$ and angular $(\xi, \eta, \phi, \dot{\xi}, \dot{\eta}, \dot{\phi})$ DOFs, where (ξ, η, ϕ) are the Euler angles. We obtain therefore an output matrix $N * T/t_{step} \times 12$ where N is the number of nodes, T is the total simulation time, t_{step} is the chosen time step. In order to load, manipulate, visualize the simulations data we developed a collection of scripts in Matlab language [57].

6.2 MBDyn Models

We developed a preliminary model for the vertical degrees of freedom of HAM-SAS, and a complete three dimensional suspension model. The time step used in all simulations is $t_{step} = 10^{-3}$ s. The parameters have been chosen, using the measurement discussed in section 4.2.2 as a reference. In order to avoid over-constraining the model, each spherical joint has been implemented with three dimensional linear springs, much stiffer (10^8 N/m) than the elastic elements of the system. This allows us to clearly identify the high frequency dummy resonances introduced in the transmissibility, and does not deteriorate the quality of the models.

6.2.1 MGAS Table Model

As shown in the sketch of fig. 6.1, the model is constituted by

- 6 **Rigid Bodies**: 1 massive base used to excite the system with respect to ground in all six DOFs through a force/position actuator, 1 optical table, 4 wand counterweighs;
- 4 **Linear Springs** with 3D diagonal stiffness matrix representing the MGAS springs;
- 8 **Wand Joints** that connects the wand counterweighs to the optical table and to the base. This joints have been implemented with linear springs with very low stiffness along x (k in figg. 6.1, 6.3) and very high elastic constant along y and z (K in the sketches). As it will be more evident in the HAM-SAS model, this has been done in order to allow the optical table to move horizontally respect to the spring box and to introduce a coupling between the vertical and horizontal DOFs.

As for the corresponding analytical model, the wands are used to introduce the desired saturation in the vertical transmissibilities. The parameters used in the simulation and their relative description are summarized in table 6.1. The

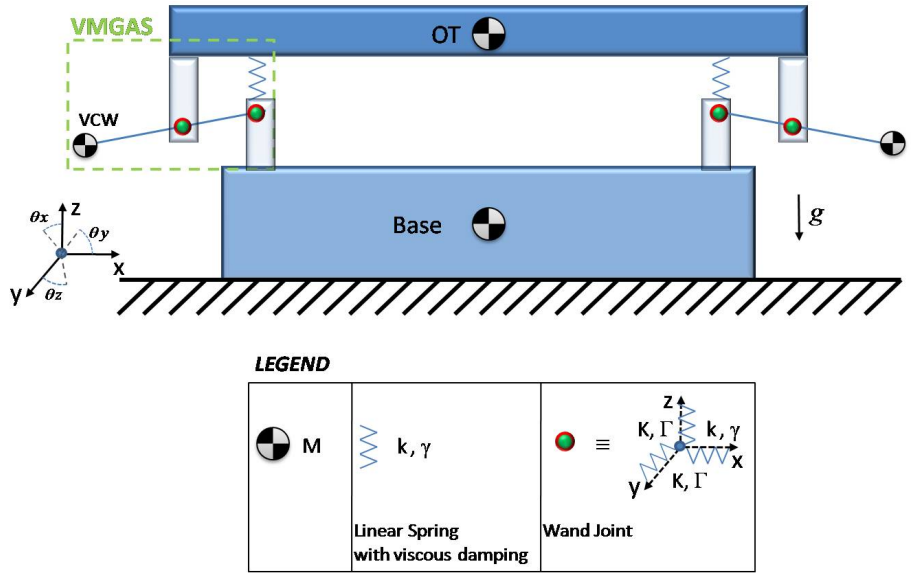

Figure 6.1: Sketch of x-z section of the MGAS Table mechanical model developed with MBDyn.

frequency of the notches of the vertical transfer functions have been tuned to 9 Hz instead of the 10 Hz used in the analytical models. Fig. 6.2 shows the transmissibility calculated from 500 s of simulated data. The transfer functions have been obtained exciting the base COM with white noise and analyzing the optical table COM along the vertical DOFs (z, θ_x, θ_y). Since MBDyn analyzes numerically the system dynamics in the time domain, the frequency resolution of the simulated transfer function is inversely proportional to the number of seconds calculated, exactly as in a real measurement.

6.2.2 The HAM-SAS Model

Adding to the MGAS Table model the mechanical components of the horizontal stage, we obtained a simulation of the complete HAM-SAS mechanical structure. As shown in the sketch of Fig. 6.3, this model incorporates

- 15 **Rigid Bodies**: 1 massive base used to excite the system with respect to the ground in all six DOFs through a force/position actuator, 1 optical table, 1 spring box, 4 inverted pendulum (IP) legs, 4 little pendulums, 4 wand counterweights;
- 4 **Angular Springs** with 3D diagonal stiffness and viscous matrices representing the flexible joints at the bottom of the IP legs;
- 4 **Linear Springs** with 3D diagonal stiffness matrix representing the MGAS springs;
- 12 **Spherical Joints**: 8 connecting the little pendulums to the IP legs and to the spring box, 4 connecting the IP legs to the base;

Parameter	Description	Value
(Dx_{MGAS}, Dy_{MGAS})	Relative distance of the MGAS springs along x and y (see fig. 6.3)	$(0.5525, 0.500)$ m
M_{Base}	Mass of the shaker base	10^6 kg
M_{OT}	Mass of the optical table	906 kg
M_{VCW}	Mass of each wand counterweight of the MGAS springs	0.1 kg
$(Ixx_{Base}, Iyy_{Base}, Izz_{Base})$	Diagonal components of base inertia tensor	$(10^6, 10^6, 10^6)$ kgm^2
$(Ixx_{VCW}, Iyy_{VCW}, Izz_{VCW})$	Diagonal components of wand counterweight inertia tensor	$(10^{-6}, 10^{-6}, 10^{-6})$ kgm^2
$(Ixx_{OT}, Iyy_{OT}, Izz_{OT})$	Diagonal components of OT inertia tensor	$(306, 306, 306)$ kgm^2
$(kx_{MGAS}, ky_{MGAS}, kz_{MGAS})$	Diagonal components of MGAS linear stiffness matrix. The value of kz_{MGAS} is calculated using eq. 5.22.	$(50, 50, 8)$ N/m
$(\Gamma x_{MGAS}, \Gamma y_{MGAS}, \Gamma z_{MGAS})$	Damping factors of the MGAS filters	$(1, 1, 1)$
$(kx_{VCW}, ky_{VCW}, kz_{VCW})$	Diagonal components of wand joint linear stiffness matrix	$(5, 10^7, 10^7)$ N/m
$(\Gamma_{VCW}, \Gamma_{VCW}, \Gamma_{VCW})$	Damping factors of the wand joints	10^2
H_{OT}	Height of the optical table center of mass respect to the base.	0.650 m
L^i_{VCW}	Arm lever of the wands	0.1 m
l^i_{VCW}	Arm lever of the wands. The value is calculated using eq. 5.10.	0.0706 m

Table 6.1: Parameters used in MBDyn MGAS Table model

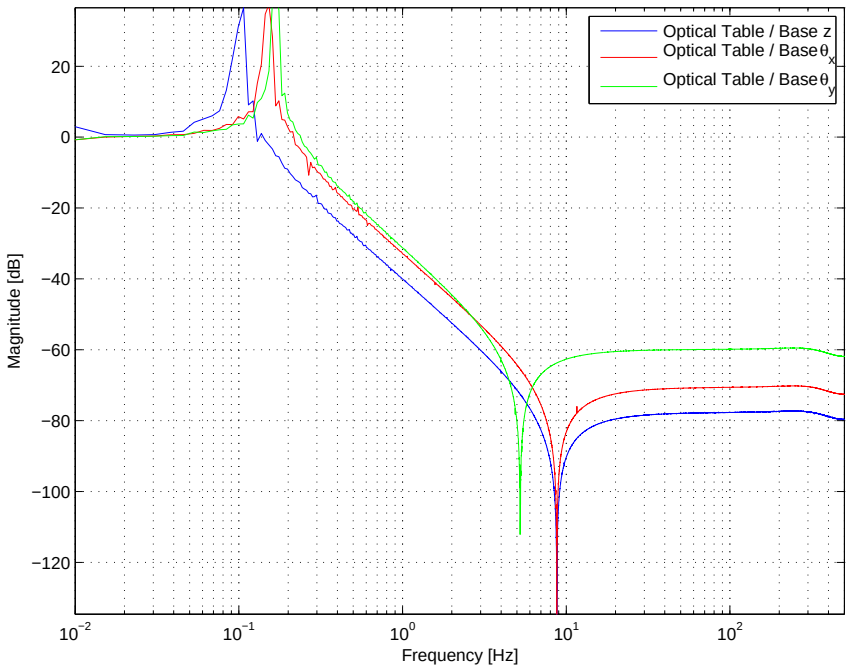

Figure 6.2: Transfer function of MBDyn MGAS Table model along the vertical DOFs z, θ_x, θ_y obtained from $T = 500$ s of simulation data.

- 8 **Wand Joints**: that connects the wand counterweights to the optical table and to the spring box. These joints are used to avoid the overconstraining of the model along the horizontal direction.
- 8 **Displacement Sensors** placed on the spring box that measure its position with respect to the base;
- 8 **Force Actuators** placed in the same position of the sensors.

The parameters used and their description are summarized in table 6.2. The presence of the wands makes the system asymmetric respect to y-z plane. For this reason only the horizontal DOFs x and θ_z (top) and the vertical DOFs x and θ_z, reported in fig. 6.4, include the effect of the wands.

In fig. 6.5 we compare HAM-SAS experimental transmissibilities that we discussed in section 4.2.2 with their relative analytical and numerical models tuned with the same parameters. As expected, the agreement between the data and the simulation, along x and y, improves as the model complexity increases. In particular the notch at 0.8 Hz introduced by the wands in the numerical simulation seems to be well reproduced by the experimental data. For $f > 10$ Hz the experimental transfer function is dominated by the noise introduced by the tilt stabilizing device.

While the vertical transmissibilities show essentially the same frequency response of the MGAS Table analytical model, the attenuation along the horizontal DOFs is much lower, for $f > 1$ Hz, than the IP Table model of chapter 5.

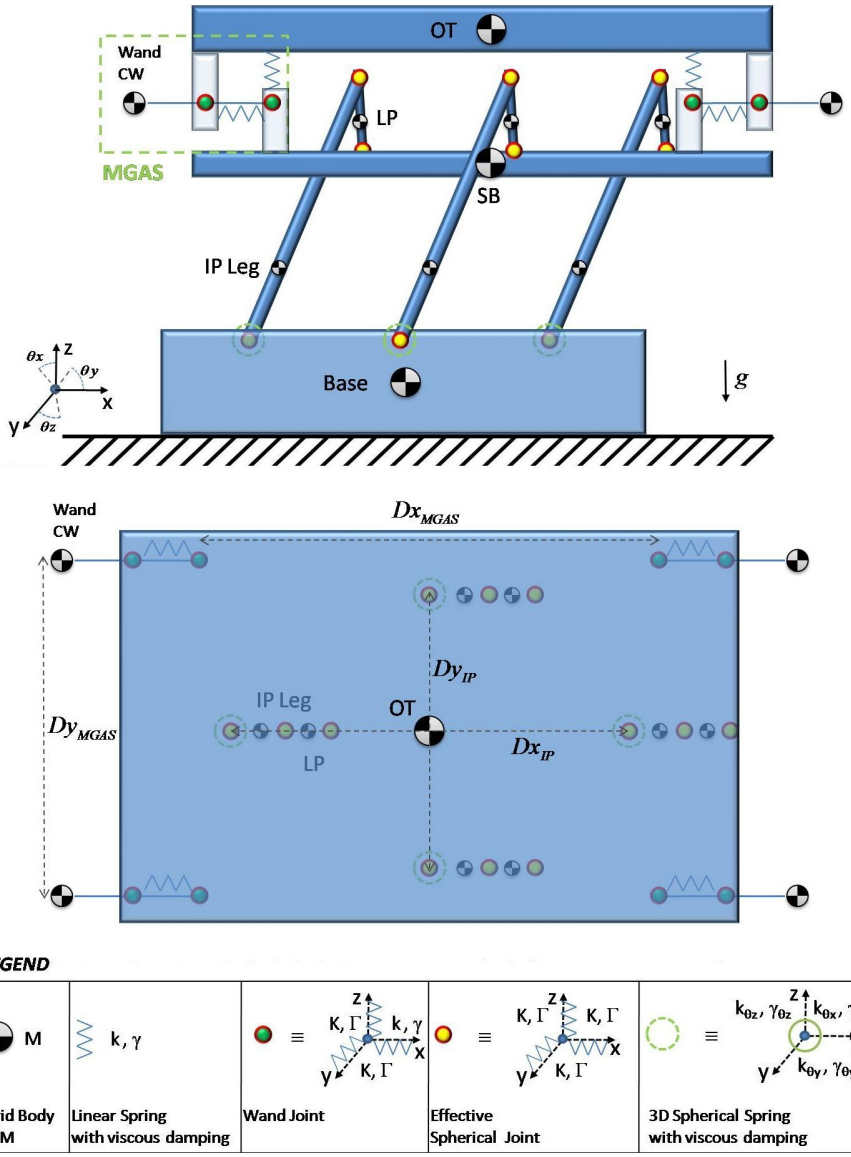

Figure 6.3: Sketch of side (top) and top (bottom) views of the HAM-SAS mechanical model developed with MBDyn.

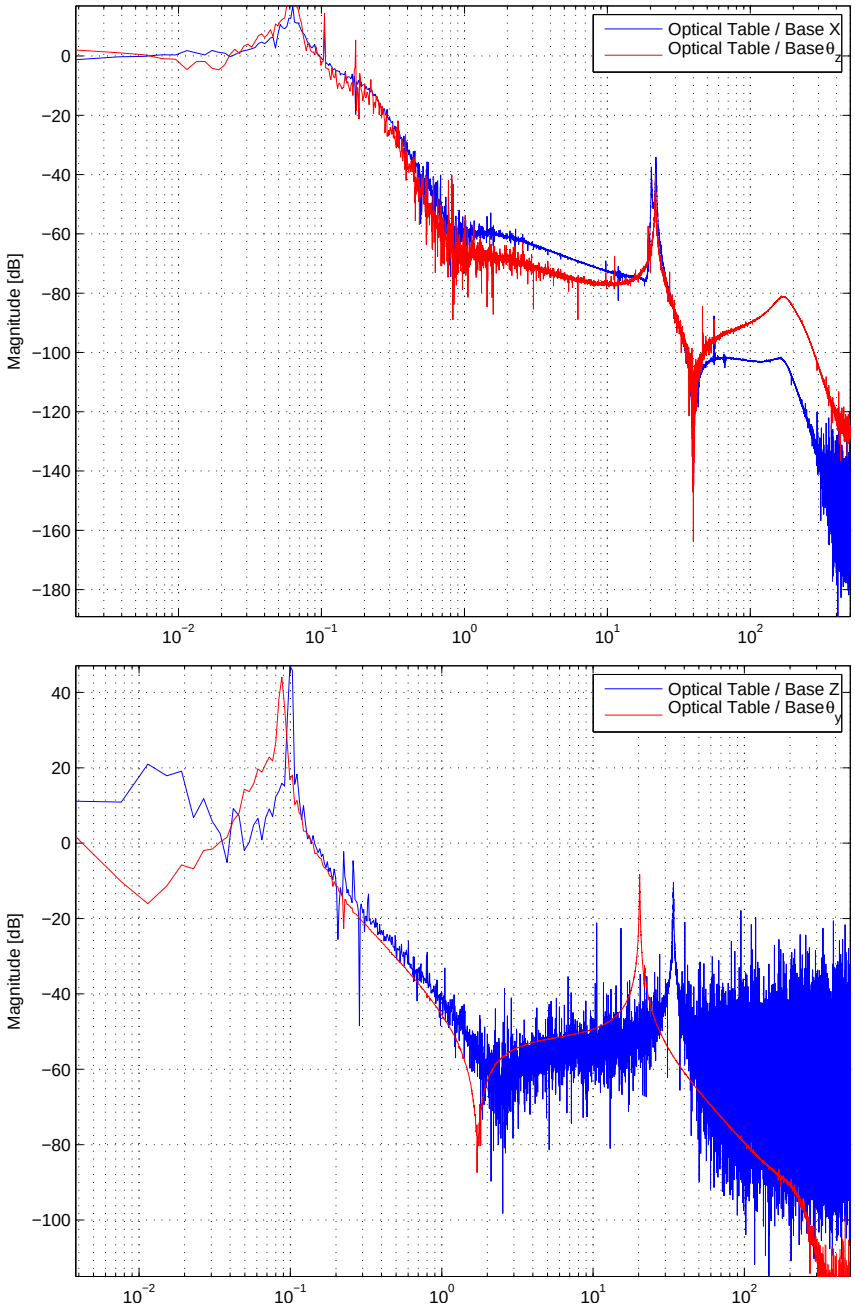

Figure 6.4: Transfer functions of MBDyn HAM-SAS model along the horizontal DOFs (x, θ_z) and the vertical DOFs z, θ_y obtained from 1000 s of simulation data.

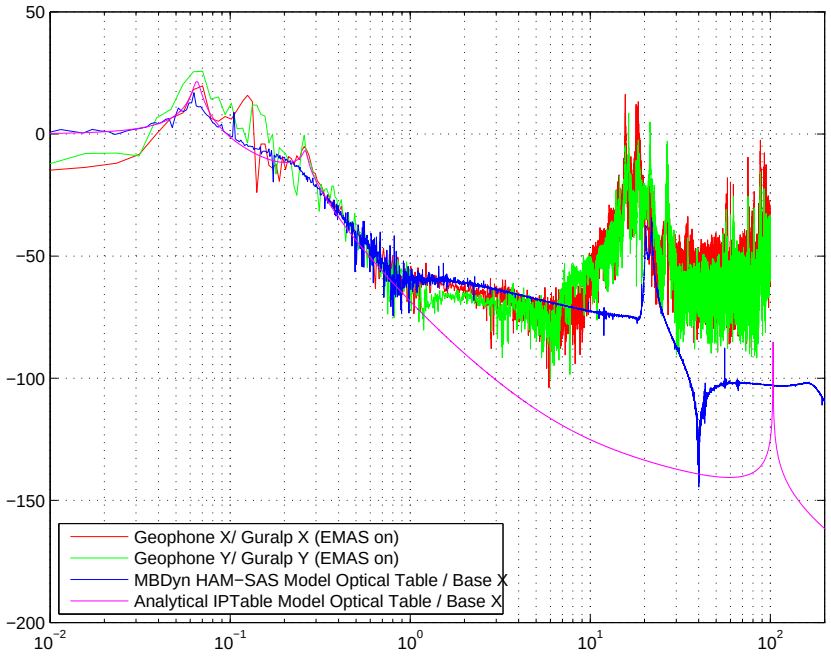

Figure 6.5: Comparison between the experimental transmissibilities, along the translational directions x, y and corresponding transmissibilities obtained from the HAM-SAS MBDyn model and from the IP Table analytical model using the same parameters.

This shows that using only a wand for each MGAS we can introduce the desired saturation in the transmissibilities along both the vertical and horizontal DOFs. Therefore our equivalent model has essentially the same dynamics of a real MGAS.

Parameter	Description	Value
(Dx_{IP}, Dy_{IP})	Relative distance of the IP legs along x and y (see fig.)	$(0.505, 0.450)$ m
(Dx_{MGAS}, Dy_{MGAS})	Relative distance of the MGAS springs along x and y (see fig.)	$(0.5525, 0.500)$ m
M_{Base}	Mass of the shaker base	10^6 kg
M_{SB}	Mass of the spring box	281 kg
M_{OT}	Mass of the optical table	906 kg
M_{IP}	Mass of each IP leg	2.608 kg
M_{LP}	Mass of each little pendulum	$2.87 \cdot 10^{-2}$ kg
M_{VCW}	Mass of each wand counterweight of the MGAS springs	0.1 kg
Izz_{VCW}	Wand counterweight moment of inertia	10^{-6} kgm^2
$(Ixx_{Base}, Iyy_{Base}, Izz_{Base})$	Diagonal components of base inertia tensor	$(10^6, 10^6, 10^6)$ kgm^2
$(Ixx_{IP}, Iyy_{IP}, Izz_{IP})$	Diagonal components of IP leg inertia tensor	$(59.9, 59.9, 5.15)\cdot 10^{-3}$ kgm^2
$(Ixx_{SB}, Iyy_{SB}, Izz_{SB})$	Diagonal components of SB inertia tensor	$(100, 100, 100)$ kgm^2
$(Ixx_{OT}, Iyy_{OT}, Izz_{OT})$	Diagonal components of OT inertia tensor	$(306, 306, 306)$ kgm^2
$(kx_{IP}, ky_{IP}, kz_{IP})$	Diagonal components of flex joint linear stiffness. The values of are calculated using eq. 5.41.	$(5277, 5277, 10^7)$ N/m
$(\Gamma x_{IP}, \Gamma y_{IP}, \Gamma z_{IP})$	Damping factors of the flex joints	$(8, 8, 8)$
$(kx_{MGAS}, ky_{MGAS}, kz_{MGAS})$	Diagonal components of MGAS stiffness.	$(50, 50, 8)$ N/m
$(\Gamma x_{MGAS}, \Gamma y_{MGAS}, \Gamma z_{MGAS})$	Damping factors of the MGAS filters	$(1, 1, 1)$
$(kx_{VCW}, ky_{VCW}, kz_{VCW})$	Diagonal components of wand joint linear stiffness	$(5, 10^7, 10^7)$ N/m
$(k_{sph}, k_{sph}, k_{sph})$	Diagonal components of the spherical joints stiffness matrix.	10^7 N/m
$(\Gamma_{sph}, \Gamma_{sph}, \Gamma_{sph})$	Damping factors of the spherical joints	10^2
$(\Gamma_{VCW}, \Gamma_{VCW}, \Gamma_{VCW})$	Damping factors of the wand joints	10^2
H_{OT}	Height of the optical table center of mass respect to the base.	0.650 m
H_{SB}	Height of the spring box center of mass respect to the base.	0.384 m
H_{IP}	Height of each IP leg center of mass respect to the base.	$3.3 \cdot 10^{-2}$m
L_{IP}	Inverted Pendulum leg length	0.5 m
L_{LP}	Little Pendulum length	$2.5 \cdot 10^{-2}$ m
L^i_{VCW}	Arm lever of the wands	0.1 m
l^i_{VCW}	Arm lever of wands. The value is calculated using eq. 5.10.	0.0706 m

Table 6.2: Parameters used in MBDyn HAM-SAS model

Chapter 7

HAM-SAS Numerical Model Linearization

7.1 MBDyn Analytical Linearization Technique

The problem of extracting a linearized model from a numerical time domain simulation is a non trivial task. Two possible approaches can be used: one is to adopt system identification techniques, as we will do with Virgo suspensions experimental data in the next chapter, the other is to put the system in the small oscillation condition and to extract analytically the eigenvalues and eigenvectors at a specific time of the simulation.

In order to obtain reduced order models from MBDyn simulations we have used an analytical technique originally developed by P. Masarati. The HAM-SAS models have been one of its first applications and represented a testbed for the code. Some of the results that we discuss in this chapter have been presented in [58] at the ECCOMAS Multibody Dynamics 2007 conference.

As we have seen in subsection 5.2.1, using generalized coordinates we can describe an n-degree of freedom mechanical system subject to holonomic constraints with a set of ordinary differential equations. However, since in numerical simulation software the variables choice and their relations are generated automatically, generalized coordinates are rarely used in computer programs. Adopting an arbitrary set of coordinates $(\mathbf{y}, \dot{\mathbf{y}})$, our mechanical problem with viscous damping have to be written as

$$\frac{d}{dt}\frac{\partial \mathfrak{L}}{\partial \dot{\mathbf{y}}} - \frac{\partial \mathfrak{L}}{\partial \mathbf{y}} + \frac{\partial \mathfrak{F}}{\partial \dot{\mathbf{y}}} - \mu \left(\frac{\partial \phi}{\partial \mathbf{y}}\right)^T = \mathbf{Q} \tag{7.1}$$

$$\phi(\mathbf{y}) = 0 \tag{7.2}$$

where the second equation describes the constraints and μ are the Lagrange multipliers. The system constituted by the last two expressions is just an example of a broad class of differential equations called Differential-Algebraic-Equations (DAEs). The most general form of a DAE is

$$\boldsymbol{F}(\mathbf{y}, \dot{\mathbf{y}}, t) = \mathbf{0}, \quad \mathbf{y}(t) = \mathbf{y}_0 \tag{7.3}$$

where $\mathbf{F} = (F_1, \cdots, F_n) : \mathbb{R}^{2n+1} \rightarrow \mathbb{R}^n$, $\mathbf{y} = (y_1(t), \cdots, y_n(t))$ and $\dot{\mathbf{y}}(t) = (\dot{y_1}(t), \cdots, \dot{y_n}(t))$ are vector valued functions and t is the independent variable.

The n-tuple $\mathbf{y}$ includes both the differential and algebraic variables. The derivative of the latter does not explicitly appear in the problem.

In MBDyn DAEs are integrated numerically, using a family of implicit multistep integration algorithms in predictor-corrector form. The predictor determines an estimate of the solution at time step k, based on the solution at earlier time steps. It is typically written in the form

$$\mathbf{y}_k = \sum_{i=1,n} a_i \mathbf{y}_{k-i} + h \sum_{j=0,n} b_j \dot{\mathbf{y}}_{k-j}, \tag{7.4}$$

where h is the time step [59]. The perturbed form of expression 7.3 can be written as

$$\mathbf{F} + \mathbf{F}_{/\dot{\mathbf{y}}} \delta\dot{\mathbf{y}} + \mathbf{F}_{/\mathbf{y}} \delta\mathbf{y} = \mathbf{0} \tag{7.5}$$

where $\mathbf{A}_{/\mathbf{x}} = \frac{\partial \mathbf{A}}{\partial \mathbf{x}}$ indicates the Jacobian matrix of $\mathbf{A}$ respect to $\mathbf{x}$. The correction phase uses the perturbed form of equation 7.4,

$$\delta\mathbf{y}_k = h b_0 \delta\dot{\mathbf{y}}_k, \tag{7.6}$$

to turn 7.5 into the purely algebraic problem

$$(\mathbf{F}_{/\dot{\mathbf{y}}} + h b_0 \mathbf{F}_{/\mathbf{y}}) \delta\dot{\mathbf{y}} = -\mathbf{F} \tag{7.7}$$

in $\delta\dot{\mathbf{y}}$ only. Since the problem is differential-algebraic, both of the matrices $\mathbf{F}_{/\mathbf{y}}$ and $\mathbf{F}_{/\dot{\mathbf{y}}}$ may be structurally singular. This problem is solved iteratively to convergence for each time step.

The eigenanalysis consists in finding the eigenvalues λ and the eigenvectors $\mathbf{Y}$ that satisfy

$$(\lambda \mathbf{F}_{/\dot{\mathbf{y}}} + \mathbf{F}_{/\mathbf{y}}) \mathbf{Y} = \mathbf{0} \tag{7.8}$$

Since the matrices $\mathbf{F}_{/\mathbf{y}}$ and $\mathbf{F}_{/\dot{\mathbf{y}}}$ are in general non-symmetric, the eigenanalysis have to be done

$$(\lambda \mathbf{F}^T_{/\dot{\mathbf{y}}} + \mathbf{F}^T_{/\mathbf{y}}) \mathbf{Y}^T_{adj} = \mathbf{0} \tag{7.9}$$

Every time step MBDyn computes the Jacobian of equation 7.7, using the function $J(c)$, in the form

$$\mathbf{J}(c) = \mathbf{F}_{/\dot{\mathbf{y}}} + c \mathbf{F}_{/\mathbf{y}} \tag{7.10}$$

In order to save computational time we choose $c = h b_0$. Simply calling the function twice with equal but opposite sign arguments, we have

$$\mathbf{F}_{/\dot{\mathbf{y}}} = \frac{\mathbf{J}(c) + \mathbf{J}(-c)}{2} \tag{7.11}$$

$$\mathbf{F}_{/\mathbf{y}} = \frac{\mathbf{J}(c) - \mathbf{J}(-c)}{2c} \tag{7.12}$$

Using the last relations we can rewrite the eigenvalue problem as

$$(\Lambda \mathbf{J}(c) + \mathbf{J}(c)) \mathbf{Y} = 0 \tag{7.13}$$

where

$$\Lambda = \frac{\lambda c + 1}{\lambda c - 1} \tag{7.14}$$

The form of last expression recalls the bilinear transform $z = \frac{1+(T/2)s}{1-(T/2)s}$, an operator used in digital signal processing to transform a continuous time filter that

depends by the Laplace variable s into a discrete one sampled at frequency $1/T$. This analogy suggests that the accuracy of the extracted eigenvalues depends by the parameter c. In fact in order to be accurately calculated, λ has to be in the interval $0 \leq |\lambda| \leq 1/c$ and therefore $1/c$ represents a sort of Nyquist frequency. Inverting 7.13 and 7.14 we obtain

$$\Lambda \mathbf{Y} = -(\mathbf{J}^{-1}(c)\mathbf{J}(-c))\mathbf{Y} \tag{7.15}$$

$$\lambda = \frac{1}{c}\frac{\Lambda+1}{\Lambda-1} \tag{7.16}$$

Projecting the matrices $\mathbf{F}_{/\mathbf{y}}$ and $\mathbf{F}_{/\dot{\mathbf{y}}}$ onto the span of the eigenvectors $\mathbf{Y}$ and $\mathbf{Y}_{adj}$, we can calculate a state-space representation of the system. Typically only a subset $\bar{\mathbf{Y}}$, $\bar{\mathbf{Y}}_{adj}$ of the eigenvectors is selected. Input and output selection is done defining the two matrices $\bar{\mathbf{B}}$ and $\bar{\mathbf{C}}$ that map the inputs $\mathbf{u}$, that in our case are the excitations applied to the shaker, into the force perturbation $-\Delta\mathbf{F}$ and the space of the variables :

$$-\Delta\mathbf{F} = \bar{\mathbf{B}}\mathbf{u} \tag{7.17}$$

$$\mathbf{z} = \bar{\mathbf{C}}\Delta\mathbf{y} \tag{7.18}$$

. Using the previous expressions and mapping eq. 7.7 on the eigenvectors space, we obtain

$$\bar{\mathbf{Y}}_{adj}\mathbf{F}_{/\dot{\mathbf{y}}}\bar{\mathbf{Y}}\dot{\mathbf{x}} + \bar{\mathbf{Y}}_{adj}\mathbf{F}_{/\dot{\mathbf{y}}}\bar{\mathbf{Y}}\mathbf{x} = \bar{\mathbf{Y}}_{adj}\bar{\mathbf{B}}\mathbf{u} \tag{7.19}$$

$$\mathbf{z} = \bar{\mathbf{C}}\bar{\mathbf{Y}}\mathbf{x} \tag{7.20}$$

We have therefore obtained a descriptor state-space representation of the system:

$$\mathbf{E}\dot{\mathbf{x}} = \mathbf{A}\mathbf{x} + \mathbf{B}\mathbf{u} \tag{7.21}$$

$$z = \mathbf{C}\mathbf{x} \tag{7.22}$$

defining

$$\mathbf{E} = \bar{\mathbf{Y}}_{adj}\mathbf{F}_{/\dot{\mathbf{y}}}\bar{\mathbf{Y}} \tag{7.23}$$

$$\mathbf{A} = -\bar{\mathbf{Y}}_{adj}\mathbf{F}_{/\mathbf{y}}\bar{\mathbf{Y}} \tag{7.24}$$

$$\mathbf{B} = \bar{\mathbf{Y}}_{adj}\bar{\mathbf{B}} \tag{7.25}$$

$$\mathbf{C} = \bar{\mathbf{C}}\bar{\mathbf{Y}} \tag{7.26}$$

The equations 7.21 and 7.22 are a generalization of the standard state-space form and they are used when the matrix $\mathbf{E}$ is poorly conditioned with respect to inversion. The expressions 7.23 and 7.24 can be rewritten using $J(c)$ function generated by MBDyn as

$$\mathbf{E} = \frac{\mathbf{J}(c)+\mathbf{J}(-c)}{2}\bar{\mathbf{Y}} \tag{7.27}$$

$$\mathbf{A} = -\bar{\mathbf{Y}}_{adj}\frac{\mathbf{J}(c)-\mathbf{J}(-c)}{2c}\bar{\mathbf{Y}} \tag{7.28}$$

The passage between the descriptor form and the standard form of the state-space representation can be done applying singular value decomposition to $\mathbf{E}$. This procedure consists in finding a factorization of the form

$$\mathbf{E} = \mathbf{U}\mathbf{\Sigma}\mathbf{V}^T \tag{7.29}$$

where $\mathbf{U}$ and $\mathbf{V}$ are orthogonal real matrices and $\mathbf{\Sigma}$ is a diagonal matrix with nonnegative real elements. This result allows to rewrite the equations 7.21 and 7.22 as

$$\begin{aligned} \mathbf{\Sigma}\dot{\xi} &= \mathbf{U}^T\mathbf{A}\mathbf{V}\xi + \mathbf{U}^T\mathbf{B}\mathbf{u} && (7.30)\\ \mathbf{z} &= \mathbf{C}\mathbf{V}\xi && (7.31) \end{aligned}$$

where ξ is the new state vector. If one or more elements of $\mathbf{\Sigma}$ are zero, the system cannot be inverted yet. However we can break the state vector in two parts, $\xi = \xi_s + \xi_d$, corresponding to the zero (ξ_s) and non zero (ξ_d) elements of $\mathbf{\Sigma}$. In this way expressions 7.30 and 7.31 can be written as

$$\begin{aligned} \mathbf{\Sigma}_d\dot{\xi}_d &= \mathbf{U}_d^T\mathbf{A}\mathbf{V}_s\xi_s + \mathbf{U}_d^T\mathbf{A}\mathbf{V}_d\xi_d + \mathbf{U}_d^T\mathbf{B}\mathbf{u} && (7.32)\\ \mathbf{0} &= \mathbf{U}_s^T\mathbf{A}\mathbf{V}_s\xi_s + \mathbf{U}_s^T\mathbf{A}\mathbf{V}_d\xi_d + \mathbf{U}_s^T\mathbf{B}\mathbf{u} && (7.33)\\ \mathbf{z} &= \mathbf{C}\mathbf{V}_s\xi_s + \mathbf{C}\mathbf{V}_d\xi_s && (7.34) \end{aligned}$$

Calculating ξ_s from equation 7.33 and substituting it in 7.32 and 7.34, the problem finally assumes the desired form

$$\begin{aligned} \dot{\xi}_d &= \mathfrak{A}\xi_d + \mathfrak{B}\mathbf{u} && (7.35)\\ \mathbf{z} &= \mathfrak{C}\xi_d + \mathfrak{D}\mathbf{u} && (7.36) \end{aligned}$$

with

$$\begin{aligned} \mathfrak{A} &= \mathbf{\Sigma}_d^{-1}\mathbf{U}_d^T\left(\mathbf{I} - \mathbf{A}\mathbf{V}_s\left(\mathbf{U}_s^T\mathbf{A}\mathbf{V}_s\right)^{-1}\mathbf{U}_s^T\right)\mathbf{A}\mathbf{V}_d && (7.37)\\ \mathfrak{B} &= \mathbf{\Sigma}_d^{-1}\mathbf{U}_d^T\left(\mathbf{I} - \mathbf{A}\mathbf{V}_s\left(\mathbf{U}_s^T\mathbf{A}\mathbf{V}_s\right)^{-1}\mathbf{U}_s^T\right)\mathbf{B} && (7.38)\\ \mathfrak{C} &= \mathbf{C}\left(\mathbf{I} - \mathbf{V}_s\left(\mathbf{U}_s^T\mathbf{A}\mathbf{V}_s\right)^{-1}\mathbf{U}_s^T\mathbf{A}\right)\mathbf{V}_d && (7.39)\\ \mathfrak{D} &= -\mathbf{C}\mathbf{V}_s\left(\mathbf{U}_s^T\mathbf{A}\mathbf{V}_s\right)^{-1}\mathbf{U}_s^T\mathbf{B} && (7.40) \end{aligned}$$

7.2 Models Linearization Results

In order to put the systems in the small oscillation condition, a linear spring and an angular spring with diagonal stiffness matrices $K_x = (10^{12}, 10^{12}, 10^{12})$ N/m and $K_\theta = (10^{12}, 10^{12}, 10^{12})$ Nm/rad are connected between the base used to excite the system and ground. The springs are then removed from the resulting linearized models subtracting from the inputs $\mathbf{u}$ the term $\mathbf{K}\mathbf{C_e}\mathbf{x}$, where $\mathbf{K}$ is the stiffness $\mathbf{K} = \begin{pmatrix} K_x & \mathbf{0}_{3\times3} \\ \mathbf{0}_{3\times3} & K_\theta \end{pmatrix}$ and $\mathbf{C}_e$ is a matrix that selects the coordinates of the excited body in the simulation (in our case the base). In this way, we can write the descriptor state-space representation of the system as

$$\begin{aligned} \mathbf{E}\dot{\mathbf{x}} &= (\mathbf{A} - \mathbf{B}\mathbf{K}\mathbf{C}_e)\mathbf{x} + \mathbf{B}\mathbf{u} && (7.41)\\ \mathbf{y} &= \mathbf{C}\mathbf{x} && (7.42) \end{aligned}$$

All the linearized models have been calculated at time $t = 0.1$ s in the simulation. The tables 7.1, and 7.2 show the resonance frequencies extracted from the linearized models using the Matlab command `damp` and their relative physical meanings.

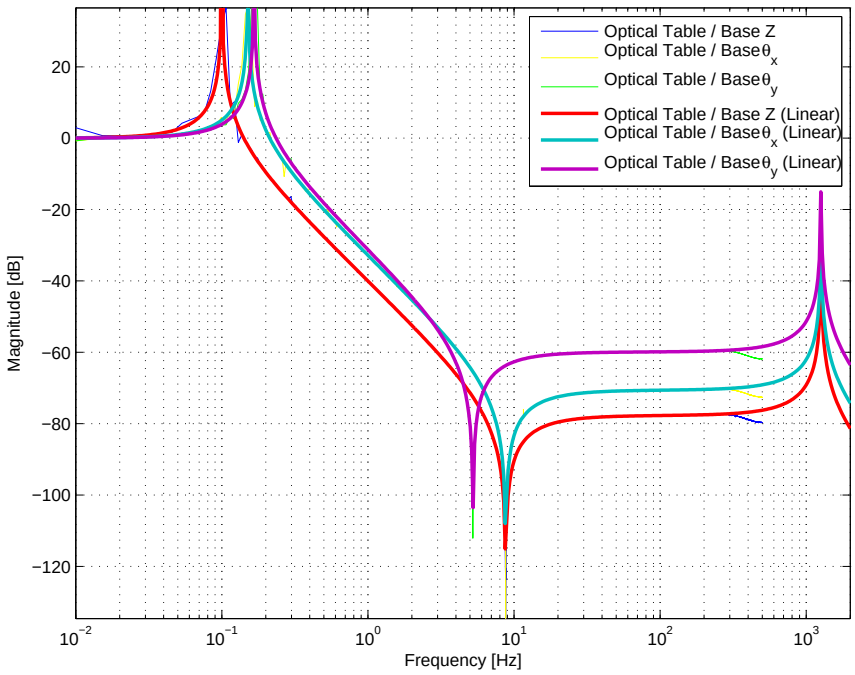

Figure 7.1: Comparison between the frequency responses of the linearized MBDyn MGAS Table models and the transfer functions of their relative time domain simulation (T =500 s, $t_{step} = 10^{-3}$ s) along the horizontal DOFs.

Fig. 7.1 shows a comparison between the transfer function calculated from MGAS Table MBDyn time domain simulation data and the frequency response of the corresponding linearized models along the vertical DOFs. As we can see there is a good agreement between the two models, confirming that our representation of the MGAS table does not contain any relevant non-linearities and that the system remained in the small oscillation condition during all the simulation.

The linearized version of the complete HAM-SAS model, along x, θ_z and z, θ_y DOFs, are shown in fig. 7.2. In the plots relative to the horizontal directions, between 20 and 100 Hz, we notice some discrepancies between the linear models and the time domain simulation. This is probably caused by numerical errors introduced by the linearization algorithm. Except for the spurious resonance at about 700 Hz introduced by the spherical joints, not visible in the time domain data because $t_{step} = 10^{-3}$ s, the frequency domain behavior along the vertical directions is essentially the same we obtained from the MGAS Table analytical models of chapter 6.

Frequency (Hz)	Description
0.1	MGAS z mode
0.1514	MGAS θ_x mode
0.166	MGAS θ_y mode
1259	Spherical joint mode

Table 7.1: Resonance frequencies extracted from the linearized MBDyn MGAS Table model

Frequency (Hz)	Description
0.0537	IP flex joint θ_z mode
0.0589	IP flex joint x mode
0.204	MGAS x mode
0.219	MGAS θ_z mode
0.089	MGAS θ_y mode
0.1	MGAS z mode
21.88	LP pendulum θ_z mode
22.39	LP pendulum x mode
64.57	LP pendulum θ_y mode
109.6	LP pendulum z mode
741.3	Spherical joint x mode
741.3	Spherical joint θ_z mode
1202	Spherical joint z mode
1202	Spherical joint θ_y mode

Table 7.2: Resonance frequencies extracted from the linearized HAM-SAS MBDyn models

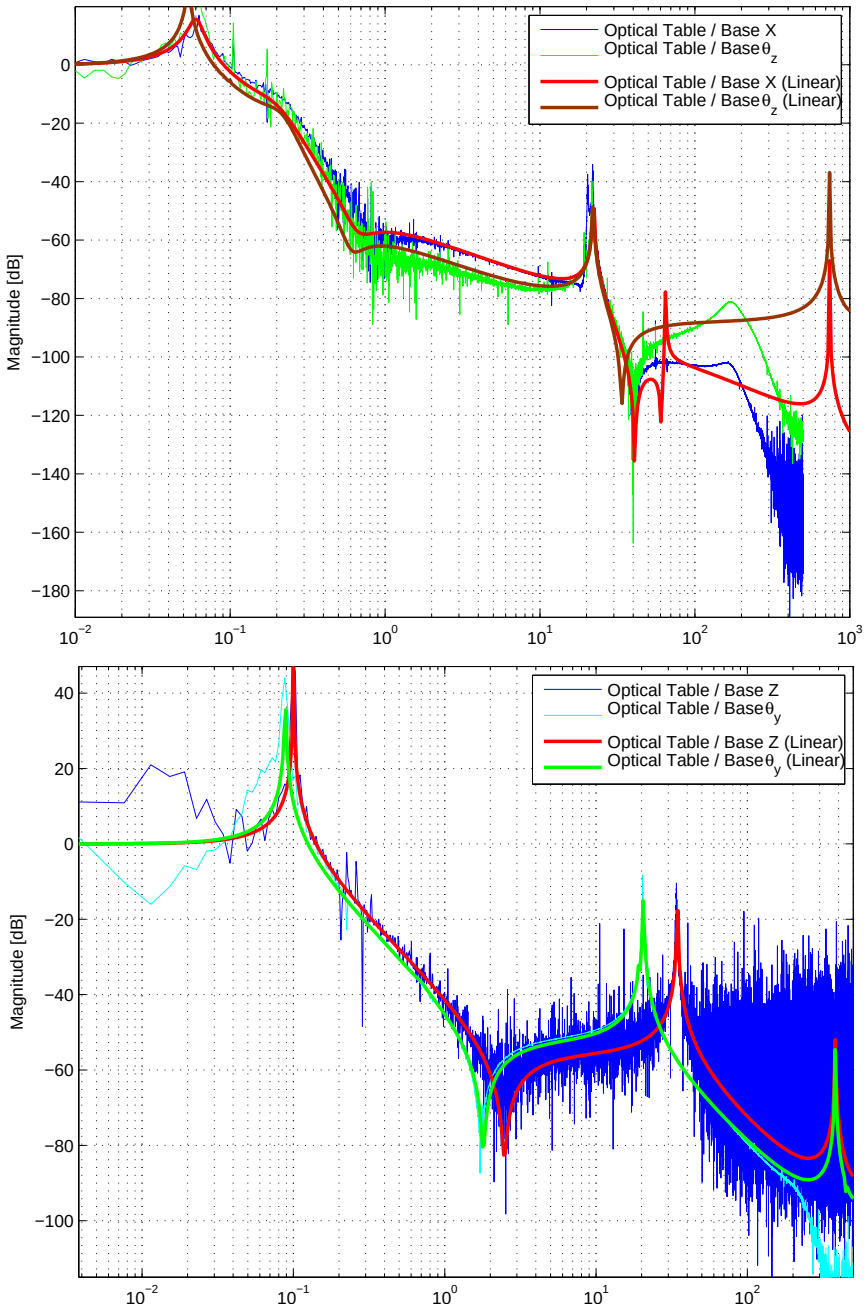

Figure 7.2: Comparison between the frequency responses of the linearized MB-Dyn HAM-SAS models and the transfer functions of their relative time domain simulation (T =1000 s, $t_{step} = 10^{-3}$ s) along the horizontal (top) and vertical (bottom) DOFs .

Part III

Virgo Suspensions Modeling

Chapter 8

A Kalman state observer for Virgo suspensions

8.1 System identification of Virgo suspensions

8.1.1 Control model of Virgo IP

As we have seen in section 3.3.1.3 six sensors, LVDTs and accelerometers, and three electromagnetic actuators, placed on the Virgo Superattenuator top table, are used for active damping. We are going to write a simple control model of the IP [60]. Since the frequencies of vertical, pitch and roll IP modes are well above the unity gain bandwidth of the control loop, we consider only the Cartesian coordinates x, y and θ_z. Using generalized coordinates, we can therefore define the state vector of the IP control system as

$$\xi = (x, y, \theta_z, \dot{x}, \dot{y}, \dot{\theta}_z) \tag{8.1}$$

Considering the coil currents as the system input vector $\mathbf{u}_A$ and the accelerometers signals as the output $\mathbf{y}_A$, we can write the IP equations of motion in the form

$$\dot{\xi} = \mathbf{A}_A \xi + \mathbf{B}_A \mathbf{u}_A \tag{8.2}$$

$$\mathbf{y}_A = \mathbf{S}_A \dot{\xi} + \mathbf{S}_T \xi \tag{8.3}$$

where $\mathbf{S}_A \dot{\xi}$ represents the IP center of mass acceleration projected along the accelerometers sensibility axis and $\mathbf{S}_T \xi$ is the top table tilt respect to the horizontal direction. Since we are in the normal mode reference frame, the matrix $\mathbf{A}_A$ has the form

$$\mathbf{A}_A = \begin{pmatrix} \mathbf{0} & \mathbf{I} \\ -\omega_j^2 \delta_{jk} & -(\omega_j / Q_j)\, \delta_{jk} \end{pmatrix} \tag{8.4}$$

where ω_j are the normal modes resonance frequencies and Q_j their relative damping factors.

In a similar way, using the IP position measurements, provided by the LVDTs, as the system output $\mathbf{y}_L$, we have

$$\dot{\xi} = \mathbf{A}_L \xi + \mathbf{B}_L \mathbf{u}_L \tag{8.5}$$

$$\mathbf{y}_L = \mathbf{S}_L \dot{\xi} \tag{8.6}$$

Substituting equation 8.2 into 8.3 and expression 8.5 into 8.6, we can rewrite both models in the standard form

$$\dot{\xi} = \mathfrak{A}\xi + \mathfrak{B}\mathbf{u} \tag{8.7}$$
$$\mathbf{y} = \mathfrak{C}\xi + \mathfrak{D}\mathbf{u} \tag{8.8}$$

with $\mathfrak{A} = \mathbf{A}_A$, $\mathfrak{B} = \mathbf{B}_A$, $\mathfrak{C} = \mathbf{S}_A\mathbf{A}_A + \mathbf{S}_T$, $\mathfrak{D} = \mathbf{S}_A\mathbf{B}_A$ and $\mathbf{u} = \mathbf{u}_A$, $\mathbf{y} = \mathbf{y}_A$ for the accelerometers model and $\mathfrak{A} = \mathbf{A}_L$, $\mathfrak{B} = \mathbf{B}_L$, $\mathfrak{C} = \mathbf{S}_L\mathbf{A}_L$, $\mathfrak{D} = \mathbf{S}_L\mathbf{B}_L$ and $\mathbf{u} = \mathbf{u}_L$, $\mathbf{y} = \mathbf{y}_L$ for the LVDTs model. Laplace transforming 8.7 and inserting in 8.8, we can write the two 3x3 transfer function matrices as

$$\mathbf{G}_A(s) = (\mathbf{S}_A\mathbf{A}_A + \mathbf{S}_T)(s\mathbf{I} - \mathbf{A}_A)^{-1}\mathbf{B} + \mathbf{S}_A\mathbf{B}_A \tag{8.9}$$
$$\mathbf{G}_L(s) = \mathbf{S}_L\mathbf{A}_L(s\mathbf{I} - \mathbf{A}_L)^{-1} + \mathbf{S}_L\mathbf{B}_L \tag{8.10}$$

Once the matrices of equations 8.7 and 8.8 have been estimated for each of the two systems, we can design a state observer (see next sections) and other parameters, such as the sensing and driving matrices that diagonalize the control loop, can be analytically calculated [61].

8.1.2 System identification Algorithms

Using system identification techniques, we are going to extract, from experimental time-domain data, the $\mathfrak{A}$, $\mathfrak{B}$, $\mathfrak{C}$, $\mathfrak{D}$ matrices for each of the models.

The goal of a system identification procedure is to generate a model of a dynamical system, based on its observed data, that behaves in the same way as the process under consideration [62]. We can distinguish four essential steps

- Measurement: we have to design an experiment that generates data informative enough respect to a generic model set. This means that, from the data, it should be possible to distinguish between different models contained in the set.
- Choice of model structure: depending on whether the parameters that constitute the model structure are based on the *a priori* physical knowledge of the system or simply viewed as a way to fit the data, we can distinguish gray and black box models. As we have seen, in our case the chosen model structure is the state-space representation.
- Identification: using numerical techniques, we want to determine the best model of the chosen set, guided by the data.
- Validation: in the final phase we want to determine how the model relates to experimental data and to prior physical modeling of the system we may have.

8.1.3 Prediction-Error Minimization Method

Considering a SISO system described by a model $\mathfrak{M}(\theta)$, function of the parameter vector θ, we introduce the quantity called prediction error defined as the difference [62]

$$\epsilon(t, \theta) = y(t) - \hat{y}(t \mid \theta) \tag{8.11}$$

between the measured ($y(t)$) and the predicted ($\hat{y}(t \mid \theta)$) outputs. The general idea behind the Prediction-Error Minimization (PEM) method is to select at time $t = t_N$ the parameters θ_N so that the errors $\epsilon(t_i, \theta_N)$ are as small as possible for $i = 1, \ldots, N$. In order to formalize this procedure, we have to define a norm, often called cost function, that can be written as

$$V_N(\theta, \mathbf{Z}) = \frac{1}{N} \Sigma_{i=1}^{N} L\left(\epsilon(t_i, \theta)\right) \tag{8.12}$$

where $\mathbf{Z} = y(t_1), \ldots y(t_N)$. The typical choice of L is the quadratic criterion

$$L = \frac{1}{2}\epsilon^2 \tag{8.13}$$

The estimate is obtained minimizing V_N

$$\theta_N = \arg\min V_N(\theta, \mathbf{Z}) \tag{8.14}$$

where $\arg\min(f)$ indicated the minimizing argument of the function f.

For a MIMO system ϵ becomes a $p \times p$ matrix, with p the number of model outputs, and

$$L = \frac{1}{2}\epsilon^T \Lambda \epsilon \tag{8.15}$$

where Λ is a symmetric $p \times p$ matrix that determines the weights of the components of ϵ.

8.1.4 The subspace method

Given a linear system in the state-space form

$$\begin{aligned} x(t+1) &= Ax(t) + Bu(t) + w(t) && (8.16)\\ y(t) &= Cx(t) + Du(t) + v(t) && (8.17) \end{aligned}$$

where $w(t)$ and $v(t)$ are Gaussian distributed, zero mean, white noise vector sequences, we want to determine the A, B, C, D matrices that gives the best description of the input-output data $u(t)$, $y(t)$. We consider our system as a black box, in the sense that we have no insight into the structure of the matrices. Consequently the matrices are not unique up to a similarity transformation.

We can see that, if we assume that not only $u(t)$ and $y(t)$ but also the state vector $x(t)$ are known, the problem can be rewritten as a linear regression: introducing

$$\begin{aligned} Y(t) &= \begin{bmatrix} x(t+1) \\ y(t) \end{bmatrix} \\ \Theta &= \begin{bmatrix} A & B \\ C & D \end{bmatrix} \\ \Phi(t) &= \begin{bmatrix} x(t) \\ u(t) \end{bmatrix} \\ E(t) &= \begin{bmatrix} w(t) \\ u(t) \end{bmatrix} \end{aligned}$$

the our state-space system becomes simply

$$Y(t) = \Theta\Phi(t) + E(t) \tag{8.18}$$

An estimate $\hat{\Theta}$ of all the elements of the matrix Θ, can now be calculated using simply the least-squared method:

$$\hat{\Theta} = \arg\min \frac{1}{N}\sum_{t=1}^{N} \|Y(t) - \Theta\Phi(t)\|^2 = \frac{1}{N}\sum_{t=1}^{N} \Phi(t)Y^T(t) \left[\frac{1}{N}\sum_{t=1}^{N} \Phi(t)\Phi^T(t)\right]^{-1}$$

where the third member of the expression can be easily obtained analytically. The accuracy of the estimate grows with the number of input-output data samples N.

In order to determine $x(t)$, traditional state estimator techniques, such as the Kalman filter (see next section), cannot be used because they require the knowledge of A, B, C, D matrices. The key point is that the state vector sequence can be obtained directly from the input-output data. The approach used by Van Overschee and De Moore [63] basically consist of two steps. As a first step, the algorithm computes a certain characteristic subspace from the given input-output data, which coincides with the subspace generated by the columns of the extended observability matrix of the system. This latter quantity is defined as

$$\Gamma_i = \begin{pmatrix} C \\ CA \\ \vdots \\ CA^{i-1} \end{pmatrix} \tag{8.19}$$

and differs from the standard observability matrix because we have $i > n$. In the second step Γ_i is used to determine two state vector sequence estimates. This is possible defining the input and output Hankel matrices

$$U_{0|i-1} = \begin{pmatrix} u_0 & u_1 & \cdots & u_{j-1} \\ u_1 & u_2 & \cdots & u_j \\ \vdots & \vdots & \cdots & \vdots \\ u_{i-1} & u_i & \cdots & u_{i+j-2} \end{pmatrix} \tag{8.20}$$

$$Y_{0|i-1} = \begin{pmatrix} y_0 & y_1 & \cdots & y_{j-1} \\ y_1 & y_2 & \cdots & y_j \\ \vdots & \vdots & \cdots & \vdots \\ y_{i-1} & y_i & \cdots & y_{i+j-2} \end{pmatrix} \tag{8.21}$$

and the triangular Toepliz matrix

$$H_i = \begin{pmatrix} D & 0 & 0 & \cdots & 0 \\ CB & D & 0 & \cdots & 0 \\ CAB & CB & D & \cdots & 0 \\ \vdots & \vdots & \vdots & \cdots & \vdots \\ CA^{i-2}B & CA^{i-3}B & CA^{i-4}B & \cdots & D \end{pmatrix} \tag{8.22}$$

We then introduce the projection Z_i of the future outputs $Y_{i|2i-1}$ onto the past and future inputs $U_{0|2i-1}$ and the past outputs $U_{0|i-1}$

$$Z_i = Y_{i|2i-1} / \begin{pmatrix} U_{0|2i-1} \\ U_{0|i-1} \end{pmatrix} \tag{8.23}$$

where $A/B = AB^T \left(BB^T\right)^{-1} B$. The estimated state vector sequences can be written as

$$\hat{X}_i = \Gamma_i^+ (Z_i - H_i U_{i|2i-1}) \tag{8.24}$$

$$\hat{X}_{i+1} = \Gamma_{i-1}^+ (Z_{i+1} - H_{i-1} U_{i+1|2i-1}) \tag{8.25}$$

where Γ_i^+ is the pseudoinverse of the extended observability matrix. Using a similar approach for the stochastic part of the model the properties of the noises $w(t)$ and $v(t)$ can be obtained.

The Van Overschee and De Moore subspace identification method has been numerically implemented by L. Ljung [62] in the MATLAB System Identification toolbox command `n4sid`.

8.1.5 Experimental Results

The measurements have been done in collaboration with P. Ruggi, during a maintenance period in preparation of the science run VSR2, and consisted in three experiments for each selected tower. We excited the IPs of the West End (WE) and West Input (WI) suspensions using the three electromagnetic actuators placed on filter 0 in succession and we measured the LVDTs and accelerometers signals. Since in the convention used in Virgo the z axis is aligned with the beam, our generalized coordinates reference frame (x, y, θ_z) becomes (z, x, θ_y). For this reason the coil currents and the LVDT signals data channels are named xCorr, zCorr, tyCorr and xLvdt, zLvdt, tyLvdt respectively. The SA filter 0 has been excited with white noise filtered by the band pass filter shown in the top bode plot of fig. 8.3. This have been done in order to avoid the excitation of high and low frequencies modes that can move the IP from its ideal position. In each experiment, we excited for 1800 s and acquired the LVDTs and accelerometers signals with 500 Hz sampling frequency.

The identification phase have implemented in two steps:

1. Since we are interested in the modes closer to the control bandwidth and in order to reduce the computation time, the data are decimated to 50 Hz. We used the `n4sid` command to calculate three state-space representations of the LVDT model (equations 8.5 and 8.6) one for each excitation, with order $n = 30$. Therefore we obtained the estimates $\hat{A}_L^i$, $\hat{B}_L^i$, $\hat{C}_L^i$, $\hat{D}_L^i$ with $i = 1, 2, 3$, where each $\hat{A}_L^i$ is 30×30, $\hat{B}_L^i$ is 30×1, $\hat{C}_L^i$ is 3×30 and $\hat{D}_L^i$ is 3×1. The results are shown in fig. 8.1, where the blue curves represents the transfer function matrix for the West End (top) and the West Input (bottom) and the red curves are the frequency response of the estimated state space models. Even though the quality factors of some modes are overestimated, a good level of agreement is reached. The resonance frequencies of the identified main modes (x_1, x_2, x_3) are respectively 43.8 mHz, 47.1 mHz and 301.4 mHz for the West End and 48.7 mHz, 57.2 mHz and 306.3 mHz for the West Input. The geometrical orientation of (x_1, x_2, x_3) is in general not aligned with (z, x, θ_y) but depends by random factors such as the asymmetric stiffness of the IP flex joints.

2. We calculated the second derivative of the models $\hat{A}_L^i$, $\hat{B}_L^i$, $\hat{C}_L^i$, $\hat{D}_L^i$ using the filter shown in the bottom plot of fig. 8.3. Then using the model

parameters obtained in the first step, we calculate $\hat{A}^i_A$, $\hat{B}^i_A$, $\hat{C}^i_A$, $\hat{D}^i_A$ with $i = 1, 2, 3$ with the predictor-error minimization method. The results are shown in fig. 8.2.

8.2 The State observer

In a generic linear time-invariant system, the number of states that can be estimated using its inputs and outputs is determined by the rank of the observability matrix $\mathcal{O}$ [64]. This quantity, that we have already written in its extended form in 8.19, is defined as

$$\mathcal{O} = \Gamma_n = \begin{pmatrix} C \\ CA \\ \vdots \\ CA^{n-1} \end{pmatrix} \tag{8.26}$$

If the rank of $\mathcal{O}$ is equal to the dimension of the state vector, the system is said to be completely observable. Calculating the observability for the three sets of estimated matrices $\hat{A}^i_L$, $\hat{B}^i_L$, $\hat{C}^i_L$, $\hat{D}^i_L$ we have $rank\left(\mathcal{O}^i_L\right) = 30$ for $i = 1, 2, 3$. Therefore our linear models are completely observable and a state observer capable of providing outputs proportional to each mode of the system can be implemented. The most common state estimator used in control theory is the Kalman filter.

8.2.1 The Discrete Kalman filter

The Kalman state observer is essentially a recursive linear filter based on a predictor-corrector type estimator that is optimal in the sense that it minimizes the estimated error covariance, when some presumed conditions are met [65]. Another aspect of this optimality is that the Kalman filter incorporates all the information that can be provided to it. It combines all available measurement data, plus prior knowledge about the system and measuring devices, to produce an estimate of the desired variables in such a manner that the error is minimized statistically.

In order to study the Kalman filter, we have to introduce two operators that acts on random vector variables: the expected value $\mathbf{E}$ <> and the covariance $\mathbf{cov}()$

$$\mathbf{E} < \mathbf{x}(t) >= \int_{-\infty}^{+\infty} \mathbf{x}(t) p(\mathbf{x}(t)) dx(t) \tag{8.27}$$

$$\mathbf{cov}(\mathbf{x}(t)) = \mathbf{E} < [x(t_1) - \mathbf{E} < x(t_1) >][x(t_2) - \mathbf{E} < x(t_2) >]^T > \tag{8.28}$$

where $p(\mathbf{x}(t))$ is the probability density function of the random vector variable $\mathbf{x}(t)$. The covariance is essentially a generalization of the variance for vector valued random variables.

First we assume that, for a discrete time system, the state vector and its related measurement data can be written in the recursive form

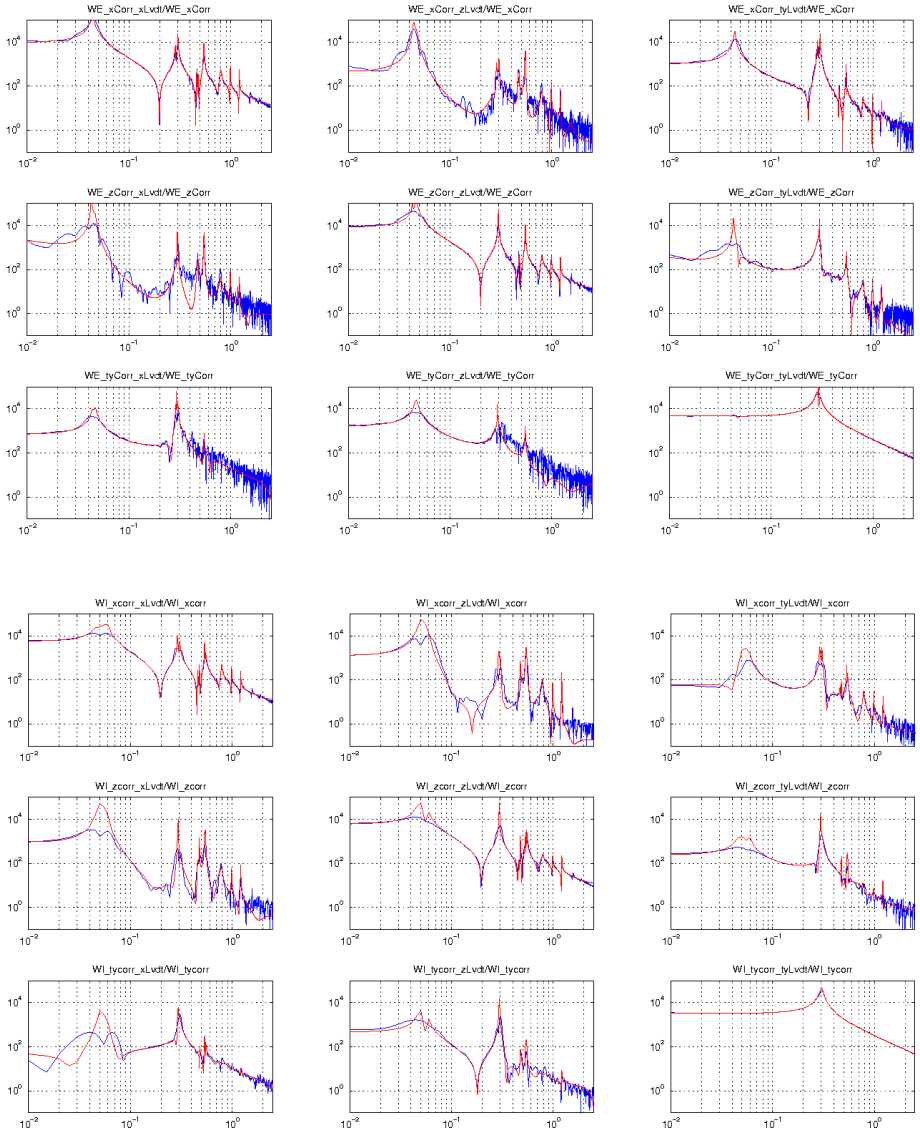

Figure 8.1: Comparison between the transfer function matrix obtained from the LVDTs measurements and the frequency response of the linear models calculated using n4sid. The top 3x3 matrix shows the results relative to the West End IP, while the bottom matrix shows the West Input IP results.

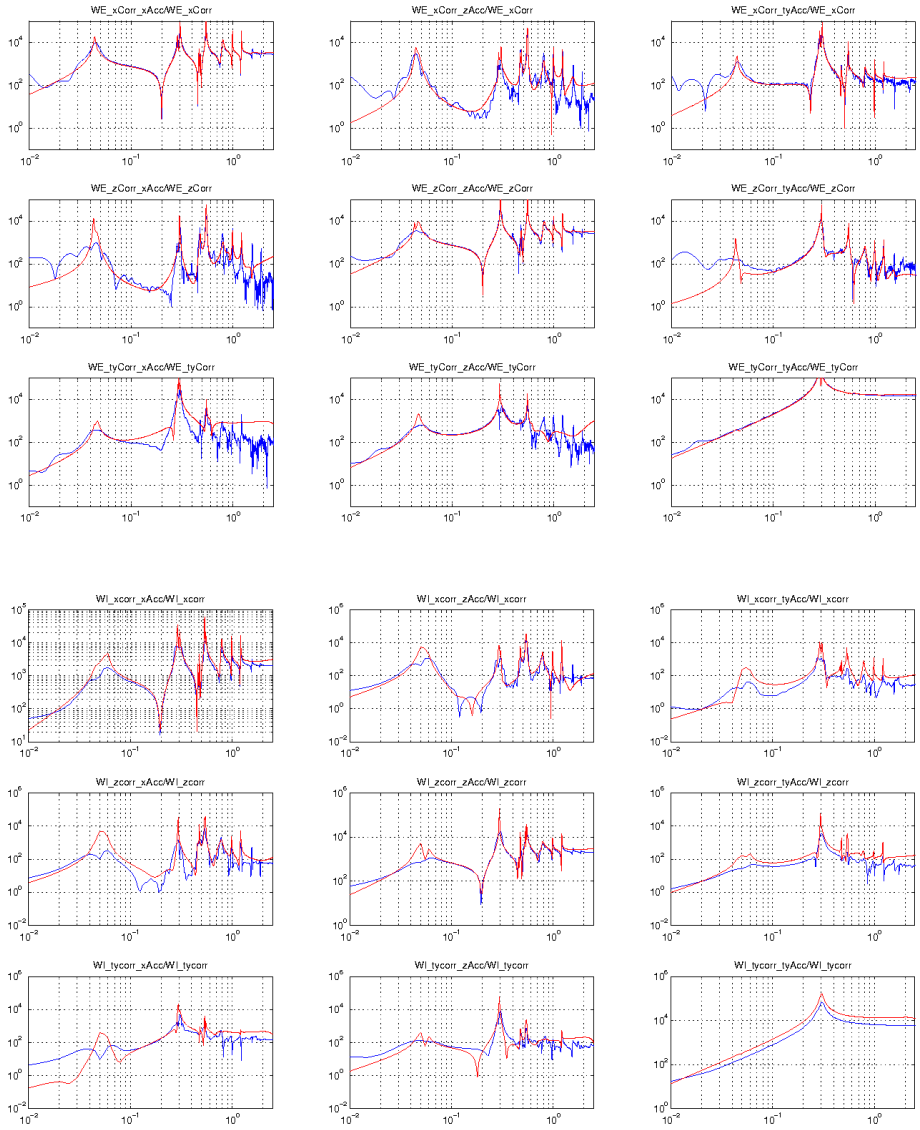

Figure 8.2: Comparison between the transfer function matrix obtained from the accelerometers measurements and the frequency response of the linear models calculated filtering the LVDT n4sid models and optimizing the estimates using PEM. The top 3x3 matrix shows the results relative to the West End IP, while the bottom matrix shows the West Input IP results.

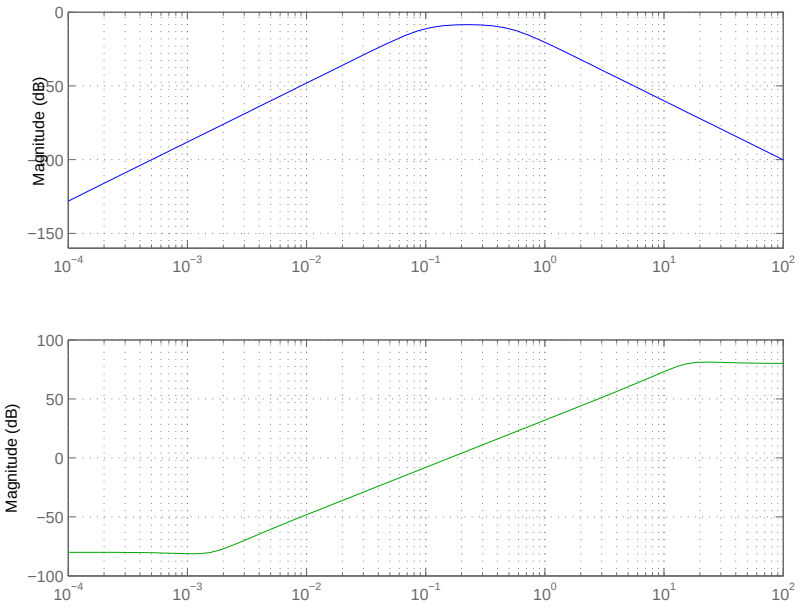

Figure 8.3: Frequency response of the filters used in the transfer function measurements. Top: Band pass filter used to excite Virgo IPs. Bottom: double derivative filter used to obtain the accelerometer model from the LVDT model

$$\mathbf{x}_{k+1} = \Phi_{k+1,k}\mathbf{x}_k + \mathbf{w}_k \quad (8.29)$$
$$\mathbf{z}_k = \mathbf{H}_k\mathbf{x}_k + \mathbf{v}_k \quad (8.30)$$

where $\mathbf{x}_k$ is the state vector of the system at time t_k, $\Phi_{k+1,k} \equiv \Phi(t_k, t_{k+1})$ is the state transition matrix between times t_k and t_{k+1}, $\mathbf{H}_k$ is the measurement sensitivity matrix, $\mathbf{w}_k$ is the process noise and $\mathbf{v}_k$ is the measurement noise. The initial conditions of the system are

$$\mathbf{E} < \mathbf{x}_0 > = \mathbf{x}_0 \quad (8.31)$$
$$\mathbf{cov}(\mathbf{x}_0) = \mathbf{P}_0 \quad (8.32)$$

where are respectively the estimate and the estimation error of $\mathbf{x}_0$. The noise sequences $\mathbf{w}_k$ and $\mathbf{v}_k$ are considered white and Gaussian distributed with zero mean. In other words, the two sequences are uncorrelated and orthogonal:

$$\mathbf{E} < \mathbf{w}_k, \mathbf{w}_j^T > = \mathbf{R}_k\delta_{kj} \quad (8.33)$$
$$\mathbf{E} < \mathbf{v}_k, \mathbf{v}_j^T > = \mathbf{Q}_k\delta_{kj} \quad (8.34)$$
$$\mathbf{E} < \mathbf{v}_k, \mathbf{w}_j^T > = \mathbf{0} \quad (8.35)$$

where $\mathbf{R}_k$ and $\mathbf{Q}_k$ are the covariance matrices of the noise sequences at time t_k.

The Kalman filter estimates a process by using a form of feedback control: the filter estimates the process state at some time and then obtains feedback in the form of noisy measurements. As such, the equations for the Kalman filter fall into two groups: time update equations and measurement update equations. The time update equations are responsible for projecting forward the current state and error covariance estimates in order to obtain *a priori* estimates for the next time step:

$$\hat{\mathbf{x}}_{k|k-1} = \Phi_{k,k-1}\hat{\mathbf{x}}_{k-1|k-1} \quad (8.36)$$
$$\mathbf{P}_{k|k-1} = \Phi_{k,k-1}\mathbf{P}_{k-1|k-1}\Phi_{k,k-1}^T + \mathbf{Q}_{k-1} \quad (8.37)$$

where the writing $\hat{\mathbf{x}}_{k|k-1}$, in this case, indicates the predicted $\mathbf{x}$ at time t_k computed using $\mathbf{z}_0, \mathbf{z}_1, \ldots \mathbf{z}_{k-1}$ measurement samples. The measurement update incorporates a new measurement into the *a priori* estimates in order to obtain *a posteriori* estimates:

$$\mathbf{K}_k = \mathbf{P}_{k|k-1}\mathbf{H}_k^T\left(\mathbf{H}_k\mathbf{P}_{k|k-1}\mathbf{H}_k^T + \mathbf{R}_k\right)^{-1} \quad (8.38)$$
$$\hat{\mathbf{x}}_{k|k} = \Phi_{k,k-1}\hat{\mathbf{x}}_{k-1|k-1} + \mathbf{K}_k\left(\mathbf{z}_k -\right) \quad (8.39)$$
$$\mathbf{P}_{k|k} = \mathbf{P}_{k|k-1} - \mathbf{K}_k\mathbf{H}_k\mathbf{P}_{k|k-1} \quad (8.40)$$

A block diagram of the estimating process is shown in fig. 8.4, where the notation used is $\Phi_{k-1} \equiv \Phi_{k,k-1}$, $\hat{\mathbf{x}}_k(+) \equiv \hat{\mathbf{x}}_{k|k}$ and $\hat{\mathbf{x}}_k(-) \equiv \hat{\mathbf{x}}_{k|k-1}$. The recursive nature of the Kalman filter is one of its most appealing features since it makes numerical implementations much more feasible than, for example, a Wiener filter [67] which is designed to operate on all of the data directly for each estimate.

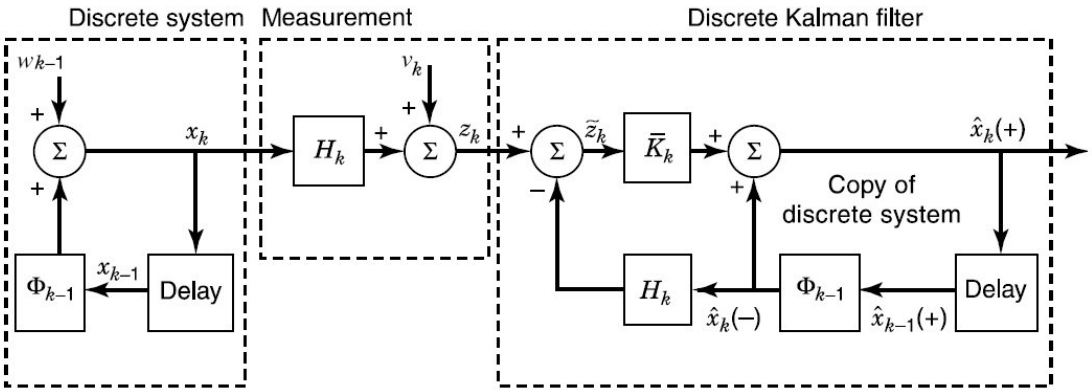

Figure 8.4: Block diagram of a discrete linear system, its measurement model and its associated discrete Kalman filter [66].

8.2.2 Implementation of the state observer

In order to obtain a numerically accurate eigenanalysis, the state-space models estimated with the subspace method are scaled. This can be done multiplying each state by some scaling factor to reduce the numerical range and sensitivity of the model. The next step consists in writing the scaled system in modal representation, a canonic form in which the real eigenvalues of the $\mathbf{A}$ matrix appear on its diagonal and the complete conjugate eigenvalues appear in 2×2 blocks on its diagonal. For a system with k real eigenvalues $\lambda_1, \ldots \lambda_k$ and s complex eigenvalues $\sigma_1 \pm \omega_1, \ldots \sigma_s \pm \omega_s$, with $k + s = n$, we have

$$\mathbf{A}_m = \begin{pmatrix} \lambda_1 & & & & & \\ & \sigma_1 & \omega_1 & & \mathbf{0} & \\ & -\omega_1 & \sigma_1 & & & \\ & & & \ddots & & \\ & & & & \lambda_k & \\ & \mathbf{0} & & & \sigma_s & \omega_s \\ & & & & -\omega_s & \sigma_s \end{pmatrix} \tag{8.41}$$

This can be done using the matrix $\mathbf{P}$ constituted by the eigenvectors of matrix $\mathbf{A}$. The state-space becomes

$$\dot{\mathbf{x}}_m = \mathbf{P}^{-1}\mathbf{A}\mathbf{P}\mathbf{x}_\mathbf{m} + \mathbf{P}^{-1}\mathbf{B}\mathbf{u} \tag{8.42}$$

$$\mathbf{y}_m = \mathbf{C}\mathbf{P}\mathbf{x}_m + \mathbf{D}\mathbf{u} \tag{8.43}$$

and we can define the new matrices $\mathbf{A}_m = \mathbf{P}^{-1}\mathbf{A}\mathbf{P}$, $\mathbf{B}_m = \mathbf{P}^{-1}\mathbf{B}$, $\mathbf{C}_m = \mathbf{C}\mathbf{P}$, $\mathbf{D}_m = \mathbf{D}$. In our case, the outputs $\mathbf{y}_m$ provide the positions/accelerations along the generalized coordinates of the suspension. It can be shown that the forms 8.4 and 8.41 are equivalent.

As we have already mentioned, using the subspace method is possible to extract some characteristics of the process and measurement noises $w(t)$ and $v(t)$. In particular, the command `n4sid` calculates the matrix $\mathbf{K}$ that transforms the measurements noise into the process noise, $w(t) = \mathbf{K}v(t)$, and the covariance

matrix **Q**. Combining **K** and **Q** with the equations 8.42 and 8.43, we can rewrite our modal state-space representation in the form

$$\dot{\mathbf{x}}_m = \mathbf{A}_m\mathbf{x}_m + \mathbf{B}_m\mathbf{u}+\mathbf{KQe}(t) \quad (8.44)$$

$$\mathbf{y}_m = \mathbf{C}_m\mathbf{x}_m + \mathbf{D}_m\mathbf{u} + \mathbf{e}(t) \quad (8.45)$$

where $\mathbf{e}(t)$ is a normalized noise source. In this way a Kalman state estimator for the previous system can be obtained simply using identity covariance matrices.

8.2.3 Experimental Results

After applying the procedure described in last subsection to the estimated state-space models, we calculated three discrete Kalman filters, one for each DOF excited. Every estimator has 4 inputs, constituted by the excitations and the measurements and 33 outputs, formed by the 30 estimated states and the 3 estimated outputs.

In fig. 8.5 we show the transfer functions between the state outputs of one observer, relative to the main resonance modes $(x_1, x_2, x_3, \dot{x_1}, \dot{x_2}, \dot{x_3})$, and its actuator signal input. The choice of the filter is arbitrary since the coils are not diagonalized and therefore each of them excites all the modes of the system. Looking at fig. 8.5 we can notice that, as expected, the position transfer functions (blue, red and green curves) have an approximately $1/\omega^2$ high frequency trend while the velocity transfer functions (magenta, black and brown curves) tends to zero for low frequencies and goes as $1/\omega$ for high frequencies. However we can see that the transfer functions x_1/xCorr (blue curve of top plot) and x_2/zCorr (red curve of bottom plot) deviates from $1/\omega^2$ for $f > 1$ Hz. This suggests that the position and velocity modes are not completely decoupled and therefore our reduction of the estimated linear models to their modal form can still be improved.

8.3 Perspectives

A first possible application of the Kalman filters we have developed, it's the implementation of a monitoring tool that provides the real-time position and velocity of Virgo inverted pendulum along its normal modes. In this way any drift in the mechanical characteristics of the IP, due for example environmental noise, can be identified and studied.

Kalman filters are commonly used for the development of MIMO optimal dynamic regulators through the Linear Quadratic Gaussian (LQG) design. As shown in fig. 8.6, an LQG regulator [68] is constituted by a Kalman filter (*kest* in the diagram) connected to the state feedback gain **K** defined for a discrete time system as

$$\mathbf{u}_k = -\mathbf{K}\mathbf{x}_k \quad (8.46)$$

. The matrix **K** is calculated minimizing the quadratic cost function **J** that can be written as

$$\mathbf{J} = \sum_{k=0}^{\infty} \left(\mathbf{x}_k^t\mathbf{Q}\mathbf{x}_k + \mathbf{u}_k^t\mathbf{R}\mathbf{u}_k\right) \quad (8.47)$$

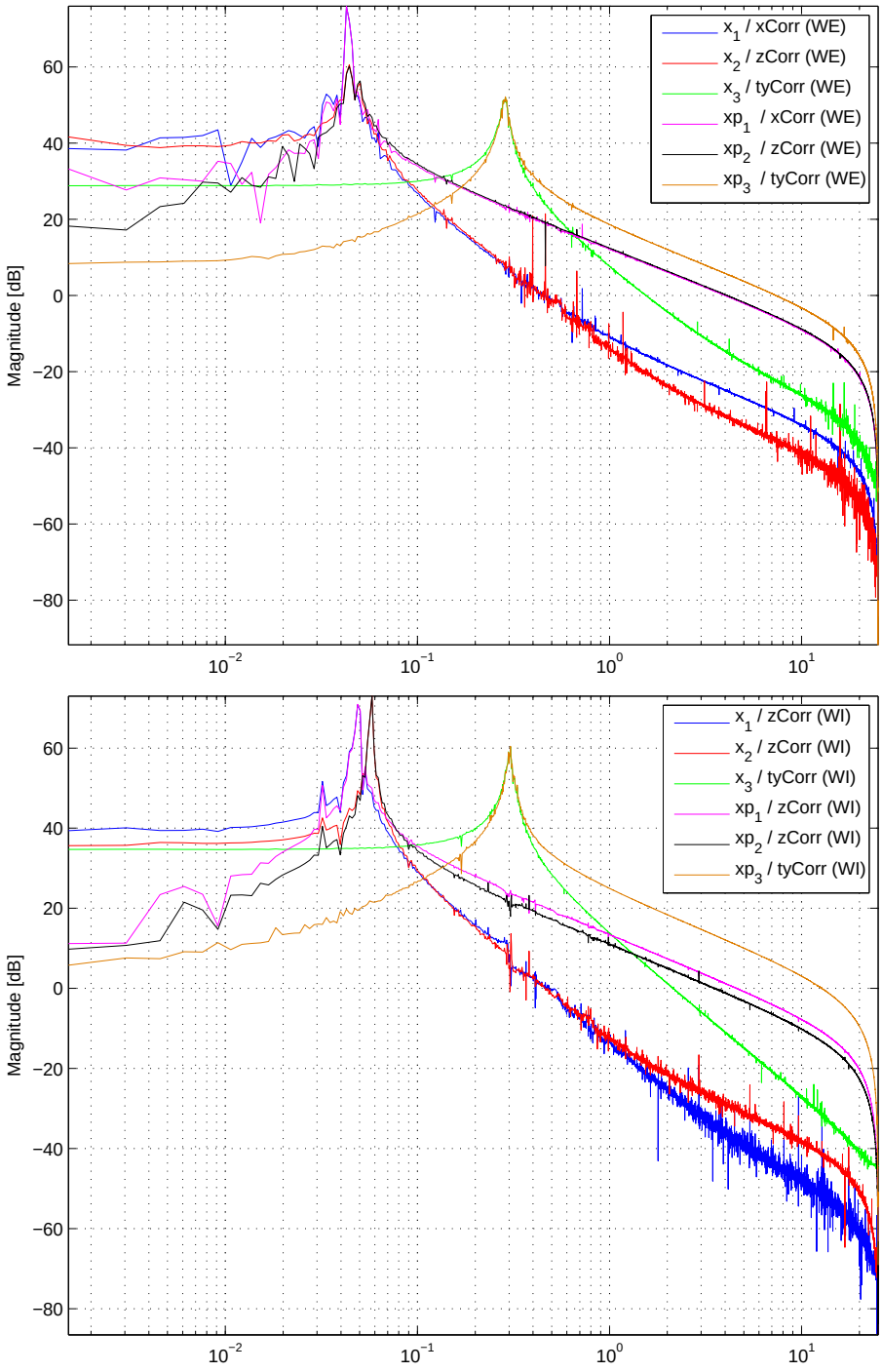

Figure 8.5: Transfer functions between the state outputs of the Kalman filters and the relative coil actuators signals for the WE (top) and WI (bottom) towers. Only the state vector of the main modes $(x_1, x_2, x_3, \dot{x_1}, \dot{x_2}, \dot{x_3})$ is shown.

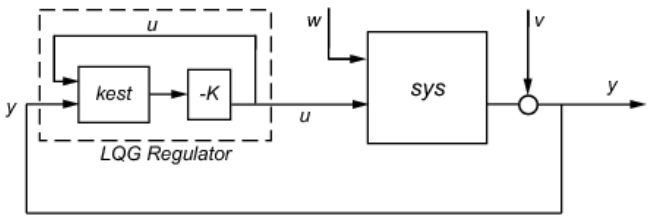

Figure 8.6: Block diagram of a plant *sys* controlled with an LQG regulator

Therefore since a plant state observer is available, we could substitute the classical SISO design approach, currently used in Virgo IP control, with a multivariable feedback technique such as the LQG. In this way the control diagonalization would no more be required, and consequently it would be possible to optimize the loop parameters also for the mixed term modes of the sensor/actuator transfer function matrix.

Conclusions

In this work we analyzed, using different approaches, the mechanical and control simulation of seismic attenuation system for both Advanced LIGO and Virgo GW interferometers. A major part of our study is concentrated on HAM-SAS, a passive seismic isolator dedicated to the Advanced LIGO HAM vacuum chambers. The results are here summarized:

- We developed a set of three-dimensional linear analytical models of HAM-SAS and we made a preliminary evaluation of its performance and controllability.
- We developed a complete three dimensional non-linear numerical model of HAM-SAS in order to improve the accuracy of the simulations. Good agreements with the experimental transmissibilities have been obtained.
- We linearized our HAM-SAS numerical models using a recently developed procedure, obtaining a set of state-space representations to be used for control simulations.
- We used system identification techniques in order to estimate a linear model of Virgo suspensions inverted pendulum. Using the obtained state space representations, we developed a Kalman filter that estimates from open loop time domain data, the state variables of the system. This allows to observe every resonance of the IP mechanical structure independently.

Acknowledgments

In such a long period there are so many people I would like to thank that it's almost impossible to make a comprehensive list. First of all I would like to thank Riccardo DeSalvo for the opportunity he gave me. Working and living in a country so different from our own is an invaluable culturally enriching experience. Virginio Sannibale has contributed to many parts of this work and represented a constant reference. His frequent advices and remarks made me certainly grow as a scientist. My deepest gratitude to Alberto Gennai and Diego Passuello that helped and supported me during many phases of this long run. Many thanks to Pierangelo Masarati for his help and availability and for the great time spent in Milan.

My life abroad would have been poorer without all the people I met in Pasadena. I would like to thank in particular Stefano and Dado, two of the best friends I've ever had, with whom I've shared many experiences that I'll never forget. My thoughts go also to Manuel, Erika, Daniele, Ciro, Simona, Cinzia, Misha, Silva and all the other members of the Caltech Italian mob. Moreover I want to express my gratitude to Giulio, Carlo Nicola and the rest of many friends I have in Pisa.

Last but not least I would like to thank my parents that, even being physically so far, they were always at my side to support me every day.

Bibliography

[1] S. Weinberg, *Gravitation and cosmology*, Wiley, New York (1993)

[2] P. R. Saulson, *Fundamentals of interferometric gravitational wave detectors*, World Scientific (1994)

[3] R. A. Hulse, J. H. Taylor, *Discovery of a pulsar in a binary system*, ApJ 195 (1975), 51-53

[4] A. Wolszczan, *A nearby 37.9-ms radio pulsar in a relativistic binary system*, Nature, 350 (1991), 688-690

[5] M. Burgay et al., *An increased estimate of the merger rate of double neutron stars from observations of a highly relativistic system*, Nature, 426 (2003), 531-533

[6] J. M. Weisberg, J. H. Taylor, *Relativistic Binary Pulsar B1913+16: Thirty Years of Observations and Analysis*, ASP Conference Series, Vol. 328 (2005), 25

[7] B. Abbott et al., *Searches for periodic gravitational waves from unknown isolated sources and Scorpius X-1: Results from the second LIGO science run*, Phys. Rev. D, 76 (2007), 082001

[8] R. Prix, *Gravitational Waves from Spinning Neutron Stars*, Neutron Stars and Pulsars, ed. W. Becker, Springer-Verlag (2009), p. 651

[9] http://numrel.aei.mpg.de/Visualisations/Archive/Oscillations/barmode.html

[10] J. L. Friedman and B. F. Schutz, *Secular Instability of Rotating Newtonian Stars*, ApJ 222 (1978), 281-296

[11] T. Zwerger, E. Muller, *Dynamics and gravitational wave signature of axisymmetric rotational core collapse*, Astron. Astrophys., 320 (1997), 209-227

[12] LIGO and Virgo Scientific Collaborations, *Search for gravitational-wave bursts associated with gamma-ray bursts using data from LIGO Science Run 5 and Virgo Science Run 1*, arXiv:0908.3824

[13] LIGO and Virgo Scientific Collaborations, *An upper limit on the stochastic gravitational-wave background of cosmological origin*, Nature, 460 (2009), 990-994

[14] R. H. Dicke, *The Theoretical Significance of Experimental Relativity*, Gordon and Breach, New York (1964)

[15] J. Weber, *Detection and Generation of Gravitational Waves*, Phys. Rev. 117 (1960), 306–313

[16] J. Peterson, *Observations and Modeling of Seismic Background Noise*, USGS Report 93-322 (1993)

[17] S. Kedar and F. H. Webb, *The Ocean's Seismic Hum*, Science, 307 (2005), n. 5710, 682-683

[18] P. R. Saulson, *Terrestrial gravitational noise on a gravitational wave antenna*, Phys. Rev. D 30 (1984), 732-736

[19] S. A. Hughes, K. Thorne, *Seismic gravity-gradient noise in interferometric gravitational-wave detectors*, Phys. Rev. D, 58 (1998), 122002

[20] G. Cella, *Underground reduction of Gravity Gradient Noise*, GWADW 2006, La Biodola (LI)

[21] J. Harms, S. Dorsher, V. Mandic, R. DeSalvo, *Gravity-Gradient Subtraction in 3rd Generation Underground Gravitational-Wave Detectors in Homogeneous Media*, arXiv:0910.2774

[22] H. B. Callen, T. A. Welton, *Irreversibility and Generalized Noise*, Phys. Rev. 83 (1951), 34–40

[23] G. Cagnoli et al., *Very High Q Measurements on a Fused Silica Monolithic Pendulum for Use in Enhanced Gravity Wave Detectors*, Phys. Rev. Letters, 85 (2000), 2442–2445

[24] Y. Levin, *Internal thermal noise in the LIGO test masses: A direct approach*, Phys. Rev. D, 57 (1998), 659–663

[25] M. Varvella, *Time-domain model for Advanced LIGO interferometer*, IEEE Nuclear Science Symposium Conference Record, 7 (2004), 4629 - 4635

[26] LIGO Scientific Collaboration, *LIGO: The Laser Interferometer Gravitational-Wave Observatory*, Rep. Prog. Phys., 72 (2009), 076901

[27] LIGO Scientific Collaboration, *Advanced LIGO Reference Design*, LIGO-M060056-v1 (2009)

[28] G. Giaime et al., *A passive vibration isolation stack for LIGO: Design, modeling, and testing*, Rev. Sci. Instrum., 67 (1), 208-214 (1996)

[29] M. V. Plissi et al., *GEO 600 triple pendulum suspension system: Seismic isolation and control*, Rev. Sci. Instrum., 71 (2000), 2539

[30] N. A. Robertson et al., *Quadruple suspension design for Advanced LIGO*, Class. Quantum Grav., 19 (2002), 4043-4058

[31] G. Ballardin et al., Measurement of the VIRGO superattenuator performance for seismic noise suppression, Review of Scientific Instruments, 72 (2001), 9, 3643-3652

[32] C. Casciano, Seismic Isolation for the Test Masses of the VIRGO Gravitational Wave Antenna, PhD Thesis (2002)

[33] G. Losurdo, *Ultra low frequency inverted pendulum for the Virgo test mass suspension*, PhD Thesis (1998)

[34] S. Braccini et al., *Low noise wideband accelerometer using an inductive displacement sensor*, Rev. Sci. Instrum., 66 (1995), 2672

[35] R. Abbott et al., *Seismic isolation enhancements for initial and Advanced LIGO*, Class. Quantum Grav., 21 (2004), 915–921

[36] S. J. Richman et al., *Multistage active vibration isolation system*, Rev. Sci. Instrum., 69 (6), (1998)

[37] A. Stochino et al., *The Seismic Attenuation System (SAS) for the Advanced LIGO gravitational wave interferometric detectors*, Nucl. Instrum. Meth. A 598 (2009), 3, 737-753

[38] V. Sannibale et al., *Recent Results of a Seismically Isolated Optical Table Prototyped designed for Advanced LIGO*, J. Phys.: Conf. Ser. 122 012010 (2009)

[39] A. Bertolini et al., *Design and prototype tests of a seismic attenuation system for the advanced-LIGO output mode cleaner*, Class. Quantum Grav. 23:S111–118 (2006)

[40] R. DeSalvo, *Passive, Nonlinear, Mechanical Structures for Seismic Attenuation*, J. Comput. Nonlinear Dynam., 2 (2007), 4, 290-298

[41] G. Cella et al., *Monolithic geometric anti-spring blades*, Nucl.Instrum.Meth. A, 540 (2005), 502-519

[42] A. Stochino et al., *Improvement of the seismic noise attenuation performance of the Monolithic Geometric Anti-Spring filters for gravitational wave interferometric detectors*, Nucl. Instrum. Meth. A 580 (2007), 1559-1564

[43] H. Tariq et al., *The linear variable differential transformer (LVDT) position sensor for gravitational wave interferometer low-frequency controls*, Nucl.Instrum.Meth. A 489 (2002), 570-576

[44] Analog Devices, AD698 Datasheet (1995)

[45] V. Boschi, V. Sannibale, *HAM-SAS LVDTs and LVDT Board Prototypes Characterization*, T060136-00-R (2006)

[46] C. Wang et al., *Constant force actuator for gravitational wave detector's seismic attenuation systems (SAS)*, Nucl. Instrum. Meth. A, 489 (2002), 563-569

[47] L. Meirovitch, *Fundamentals of Vibrations*, McGraw-Hill (2001)

[48] I. Taurasi, *Inverted Pendulum Studies for Seismic Attenuation*, LIGO-T060048 (2006)

[49] Y. Huang at al., *HAM-SAS Spring Box Simulations*, LIGO-T060066-00-E (2006)

[50] LIGO-D51101-D51245 (2006)

[51] A. Takamori, *Low Frequency Seismic Isolation for Gravitational Wave Detectors*, PhD Thesis, LIGO-P030049-00-R (2003)

[52] P. Fritschel et al., *Seismic Isolation Subsystem Design Requirements Document*, LIGO-E990303-03-D (2001)

[53] P. Fritschel, *HAM Seismic Isolation Requirements*, LIGO-T060075-00-D (2006)

[54] J. J. Mcphee, *A unified graph—theoretic approach to formulating multibody dynamics equations in absolute or joint coordinates*, Journal of the Franklin Institute, 334 (1997), 3, 431-445

[55] G. L. Ghiringhelli, P. Masarati, P. Mantegazza, and M. W. Nixon, *Multi-body analysis of a tiltrotor configuration*, Nonlinear Dynamics, 19(4):333–357, August 1999

[56] http://www.aero.polimi.it/~mbdyn/

[57] http://www.ligo.caltech.edu/~citsas/Exp/Home.shtml

[58] V. Boschi et al., *Seismic attenuation system synthesis by reduced order models from multibody analysis,* Proceedings of ECCOMAS Multibody Dynamics 2007 Conference

[59] K. E. Brenan, S. L. Campbell, L. R. Petzold, *Numerical Solution of Initial Value Problems in Differential Algebraic Equations*, SIAM (1996)

[60] A. Gennai et al., *A Control Model for the inverted pendulum*, VIR-NOT-PIS-4900-102 (1997)

[61] V. Boschi, *Sviluppo nel dominio del tempo del sistema di controllo per il damping inerziale di Virgo*, B.S. thesis (in Italian)

[62] L. Ljung, *System Identification: Theory for the User*, Prentice-Hall (1999)

[63] P. Van Overschee, B. De Moor, *N4SID: Subspace algorithms for the identification of combined deterministic-stochastic systems*, Automatica, Special Issue on Statistical Signal Processing and Control, vol. 30, no. 1, Jan. 1994, pp. 75-93.

[64] T. Kailath, *Linear Systems*, Prentice-Hall (1980)

[65] H. W. Sorenson, *Least-squares estimation: from Gauss to Kalman*, IEEE Spectrum, vol. 7, 63-68 (1970)

[66] M. S. Grewal, A. P. Andrews, Kalman Filtering: Theory and Practice Using MATLAB, John Wiley & Sons (2001)

[67] R. G. Brown and P. Y. C. Hwang, *Introduction to Random Signals and Applied Kalman Filtering*, John Wiley & Sons (1992)

[68] J. M. Maciejowski, *Multivariable Feedback Design*, Addison-Wesley (1989)